EXPERIMENTAL AND NUMERICAL STUDY ON SHEAR FAILURE MECHANISM OF RC DEEP BEAMS

Yasar Hanifi GEDIK

EXPERIMENTAL AND NUMERICAL STUDY ON SHEAR FAILURE MECHANISM OF RC DEEP BEAMS

By

Yasar Hanifi GEDIK

A Dissertation Submitted to Nagoya University

In partial Fulfillment of the Requirements for

The degree of Doctor of Engineering

Department of Civil Engineering

Graduate School of Engineering, Nagoya University

Nagoya, JAPAN

July, 2011

ACKNOWLEDGEMENTS

ABSTRACT

The shear failure mechanisms of RC deep beams differs from ordinary beams and so far several studies focused on to investigate the shear failure mechanism and shear strength of deep beams. Considerable amount of the load is carried by compression struts and the strain distribution in the member is considered as non-linear in deep beams. Moreover, there is limited effect of stirrup for smaller shear span to depth ratios (a/d). On the other hand, the size effect in short deep beam without shear reinforcement is significant. Therefore, the evaluation of shear strength of deep beams is more complicated and a deep comprehension of load carrying mechanism is required.

Regarding design method of shear failure of RC deep beams, several design equations are applied in the world. In ACI 318-0.5 Code, the limit shear span to height ratio (a_v/h) is equal to 2.0 for deep beams, where the entire member is considered as a single the D-region and Strut and tie models (STM) can be used for the design of the D regions. On the other hand, a method to calculate the shear strength of deep beams is given in The Standard Specifications for Concrete Structures (2002). In this method, stirrup contribution is calculated based on truss analogy and then the calculated value is reduced depending on a/d ratio. That is, the stirrup effect decreases for smaller a/d ratio. However, in the JSCE's 2007 Standard Specifications for Concrete Structures, the previous method was revised based on the experimental results. In this method, the effect of stirrup is considered by the increase of concrete contribution. The effect of stirrup increases by increase of the parameters of stirrup ratio and shear span to depth ratio. That is, there are several different approaches to evaluate the shear strength of deep beams with stirrup since the shear failure behavior of deep beams has not been fully clarified yet. Therefore, one of the main purposes of this study is to clarify the shear failure mechanism of deep beams.

Numerical methods are useful to evaluate the shear failure mechanism of RC deep beams. However, the shear failure behavior of RC deep beams is a complex matter that is affected by the compression failure of concrete, shear crack propagation, bond and anchorage of reinforcing bars and a number of other factors. Therefore, modeling shear failure is one of the difficult problems in the numerical simulation of concrete structures. Moreover, since the failure of deep beams localizes near the support and loading points with a complex high

stress state, it is important to consider the behavior of strain softening. Therefore, advanced method to accurate simulation of these behaviors is required.

The general purpose of this dissertation is to evaluate and clarify the shear failure mechanism of RC deep beams in detail. The shear failure behavior of deep beams is investigated both experimentally and numerically by 3-D RBSM as an advanced method. Firstly, the applicability of the numerical tool on deep beams is demonstrated and confirmed. Then, the load carrying capacity of deep beams with stirrup was numerically investigated, and the shear failure mechanism based on the B and the D-region concept was clarified. Three types of stirrup effect on the load carrying capacity are observed in deep beams. In a/d=0.5 case, 3-D effects is dominant and the peak load increases due to confinement effect of stirrup. That is, there is no significant effect of stirrup along the vertical direction. In a/d=1.0 case, the stirrup contribute the strut action that leads to increase in load. In the case of a/d ≤ 1.0, the D-region is dominant. On the other hand, the peak load increases significantly with the increase of stirrup in the case of a/d≥1.5, in which the truss analogy is dominant rather than the strut action.

Then, 3D behavior as well as the shape and size effect is investigated in order to clarify 3-D effects in short deep beams. To achieve that, deep beams with a/d=0.5 and having different sizes are tested, and failure mechanism was discussed to determine the shape and size effect on behavior. The effect of beam width on load carrying capacity, failure mode, crack pattern and 3-D behavior was investigated, and the shape and size effect was clarified. In addition, the beams were analyzed by the 3-D RBSM and three-dimensional deformation, strut widths and cross sectional stress distribution were investigated numerically and compared with the experimental results to determine 3-D behavior in detail. Therefore, 3-D effects in short deep beams were clarified.

Since there is no significant effect of stirrup along vertical direction and 3-D effects are important in short deep beams, a new reinforcement method named "horizontal stirrup arrangement" is proposed for short deep beams by considering three-dimensional effects. In this method, stirrups are placed within the shear span horizontally along the beam height. The proposed stirrup arrangement provides the increase of load carrying capacity of a short deep beam as well as the ductility by confinement effect of horizontal stirrups. The effectiveness of the horizontal stirrup arrangement was confirmed by both experimentally and numerically.

Table of Contents

List of Tables

List of Figures

1. Introduction

1.1 General Background and Purpose

The shear failure mechanism of RC deep beams is different from ordinary beams and so far several studies focused on to investigate the shear failure mechanism and shear strength of deep beams (Zararis 2003; Yang et al. 2003; Ashour 2000; Tan et al. 1999; Sanad et al. 2001; Salamy et al. 2005; Tang et al. 2004; Mau et al. 1989; Ashour et al. 2003; Rogowsky et al. 1986; Smith et al. 1982; Wang et al. 1993; Averbuch et al. 1999 and Niwa 1983). In deep beams, considerable amount of the load is carried by compression struts and the strain distribution in the member is considered as non-linear (Mac Gregor 1997). Moreover, the effect of stirrup is limited for smaller shear span to depth ratios (a/d) (Kosa et al. 2005; Tanimura et al. 2004). On the other hand, the shear failure mechanism of deep beams is affected by the size of a specimen. In the literature, size effect in concrete deep beams has been investigated and presented by several researchers (Walraven and Lehwalter 1994; Zhang and Tan 2007; Tan and Cheng 2006; Bazant and Kazemi 1991; Kotsovos and Pavlovic 2004). Walraven and Lehwalter (1994) stated that the size effect in short members without shear reinforcement, in which behavior is dominated by strut and tie action, is significant. Therefore, the evaluation of shear

strength of deep beams is more complicated and it requires a deep comprehension of load carrying mechanism.

Regarding design method of shear failure of RC deep beams, several design equations are applied in the world. Design equations for the shear strength of deep beams are given in Appendix A in detail. ACI 318-0.5 Code (ACI 2005) describes the deep and slender beams based on the shear span to height ratio (a_v/h). The limit shear span to height ratio (a_v/h) for deep beams is equal to 2.0. The entire member is considered as a single the D-region for deep beams. Strut and tie models (STM) can be used for the design of the D regions. On the other hand, a method to calculate the shear strength of deep beams is given in The Standard Specifications for Concrete Structures (JSCE 2002). In this method, stirrup contribution is calculated based on truss analogy and then the calculated value is reduced depending on a/d ratio. That is, the stirrup effect decreases for smaller a/d ratio. However, in the JSCE's 2007 Standard Specifications for Concrete Structures (JSCE 2007), the previous method was revised based on the experimental results. In this method, the effect of stirrup is considered by the increase of concrete contribution. The effect of stirrup increases by increase of the parameters of stirrup ratio and shear span to depth ratio. The discussion above shows that, there are several different approaches to evaluate the shear strength of deep beams with stirrup since the shear failure behavior of deep beams has not been fully clarified yet. Therefore, one of the main purposes of this study is to clarify the shear failure mechanism of deep beams.

Numerical methods are useful to evaluate the shear failure mechanism of RC deep beams. They give us not only global behavior such as load displacement relationship but also cracking, local strain, local stress and so on. The information is useful to understand the shear

failure mechanism of deep beams profoundly. However, modeling shear failure is one of the difficult problems in the numerical simulation of concrete structures because the shear failure behavior of RC deep beams is a complex matter that is affected by the compression failure of concrete, shear crack propagation, bond and anchorage of reinforcing bars and a number of other factors. The prediction of damage and failure of concrete, which is a quasi-brittle heterogeneous material, requires a physically realistic and mathematically sound description of softening behavior (Bazant 1986; Mazars and Pijauder-Cabot 1986; Bazant and Pijauder-Cabot 1988). Since the failure of deep beams localizes near the support and loading points, where there exist complex states of high stress, accurate representation of softening behavior is both essential and complicated. Attempts to describe the failure by local continuum theory have been inadequate since the localization phenomena caused by material softening cannot be obtained objectively (Bazant 1986; Bazant and Pijauder-Cabot 1988). Such models tend to exhibit mesh dependency of deformation, local strain, as well as the localization area (Bazant 1976). Therefore, an advanced method to simulate these behaviors accurately is required.

Beside the continuum theory, numerical methods based on discrete mechanics have been proposed and applied to concrete structures (Meguro and Hakuno 1989; Shi and Goodman 1989; Schlangen 1993; Schlangen and van Mier 1992; Bolander et al. 1996 and van Mier 1997). The discrete methods do not rely on the continuum assumption and this facilitates some aspects of fracture modeling. The rigid-body-spring model (RBSM) is one such method, which was first proposed by Kawai in 1978 (Kawai 1978; Bolander et al. 2000; Bolander and Hong 2002 and Saito 1999). RBSM can show realistic behavior from cracking to failure, and it can also be used to investigate stress transfer mechanisms at the meso-level (Yamamoto et al. 2008 and Yamamoto 2010). Furthermore, 3-D RBSM is applicable to the simulation of 3-

D behavior as well as the effects of confinement of concrete. Therefore, one of the main purposes of this study is to clarify the applicability of 3D RBSM and is to evaluate the shear failure mechanism of deep beams numerically.

The general purpose of this dissertation is to evaluate and clarify the shear failure mechanism of RC deep beams in detail. The shear failure behavior of deep beams is investigated both experimentally and numerically by 3D RBSM as an advanced method. The applicability of the numerical tool on deep beams is demonstrated and confirmed. The load carrying capacity and shear failure mechanism of deep beams with stirrup, and three-dimensional effects as well as the size and shape effects in short deep beams, which represent the beams with shear span to depth ratio (a/d) less than 1.0 in this study, are explored in detail and clarified based on the numerical results. Moreover, a new reinforcement arrangement for short deep beams is proposed considering clarified shear failure mechanism.

1.2 Objectives and Content of the Study

A general content of the study is summarized in Fig. 1.1. In order to achieve the purpose for investigation of shear failure mechanism of RC deep beams, the effect of several factors such as stirrup, shape and size are investigated experimentally and numerically. Moreover, a new horizontal stirrup arrangement for short deep beams is proposed.
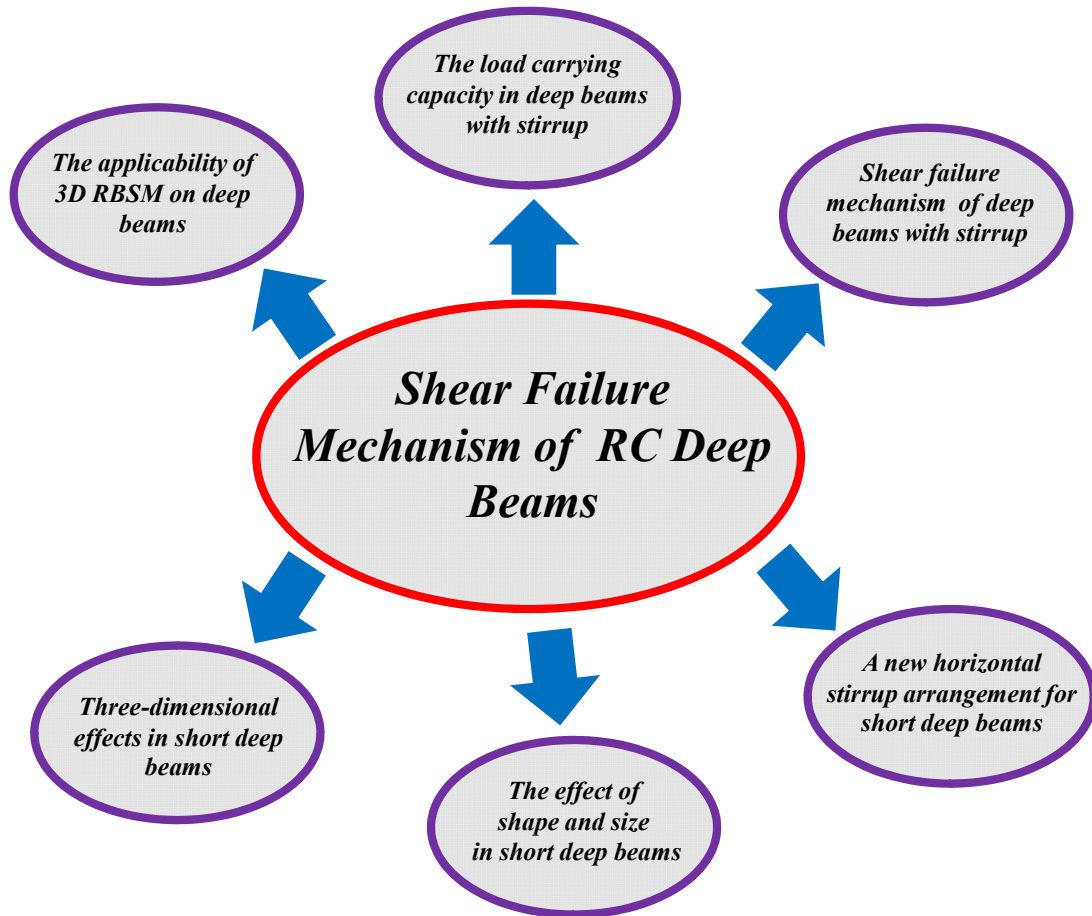
Fig. 1.1 Framework of the Dissertation

Chapter 1 is the introduction part. A general background of the study is presented. The content and objectives of the dissertation is included.

In chapter 2, the numerical model 3-D RBSM is explained. Constitutive models for compression, tension and shear is presented. Reinforcement model used in 3-D RBSM is given. Moreover, the applicability of the numerical model is confirmed by comparison of experimental and numerical results for compression cylinder specimens.

In chapter 3, the applicability of the 3-D RBSM on deep beams is verified. In order to achieve that, a series of deep beam with and without stirrup and having shear span to depth ratio a/d=0.5 to 2.0 is tested. Experimental results are presented and discussed. Then, the

tested specimens are also analyzed by 3-D RBSM. The experimental and the numerical results obtained from 3-D RBSM are compared in terms of displacement curves, crack pattern, failure mode as well as the strain of stirrups. Therefore, the simulation capability of the numerical tool in deep beams is confirmed.

In chapter 4, a series of deep beam with and without stirrup and having shear span to depth ratio a/d=0.5 to 2.0 as well as slender beams with a/d=3.0 are analyzed by 3-D RBSM, in order to investigate the load carrying capacity of deep beams with stirrup and to clarify the shear failure mechanism based on the B and the D-region concept. The load carrying capacity and the shear failure mechanism are investigated in detail by evaluation of load-displacement curves, crack pattern, 3-D deformed shapes, strut behavior and stress distribution and crack widths as well as the strain of stirrups. Finally, the load carrying capacity and shear failure mechanism of deep beams with stirrup is clarified.

In chapter 5, the shape effect and size effect in short deep beams is investigated in detail as well as 3-D behavior using 3-D RBSM. In order to achieve that, two series of deep beams with a/d=0.5 and having different widths and heights are tested. Therefore, size effect as well as the shape effect on the shear failure behavior is investigated. The tested beams are simulated by 3D RBSM and the results, such as the load-displacement curve, deformation, and failure depths on the strut, are compared. Moreover, the analyses are expanded to include various width cases to clarify the effect of beam width in detail.

Chapter 6 includes a new reinforcement method for short deep beams. The results obtained from the investigation of shear failure mechanism in deep beams and the investigation on three dimensional effects in short deep beams show that, the compressive shear failure with spalling of concrete along the compression struts occurs in deep beams

6

having shear span to depth ratio (a/d) less than 1.0. That is, three-dimensional behavior is important in short deep beams and it is dominant on behavior. Moreover, it was clarified that there is no significant effect of stirrup along the vertical direction in deep beams with a/d less than 1.0. This means that, no effective reinforcement method in order to enhance the structural performance of short deep beams has been proposed yet. Therefore, a new reinforcement method named "horizontal stirrup arrangement" is proposed for short deep beams by considering three-dimensional effects. In this method, stirrups are placed within the shear span horizontally along the beam height. The proposed stirrup arrangement provides the increase of load carrying capacity of a short deep beam as well as the ductility by confinement effect of horizontal stirrups. The effectiveness of the horizontal stirrup arrangement is confirmed by both experimentally and numerically.

Chapter 7 presents summary and conclusions of the study.

2. Numerical Model

2.1 Introduction

In this chapter, three-dimensional Rigid-Body-Spring-Model (3-D RBSM), which is the numerical tool used in this study, is introduced. Firstly, a general explanation of RBSM is given. Secondly, the tensile, compression and shear constitutive models of concrete are expressed. Then, the reinforcement model of the numerical tool is explained. At last, applicability of 3-D RBSM by uniaxial compression and triaxial cylinder analyses is demonstrated.

2.2 3-D RBSM

In a 3-D RBSM, concrete is modeled as an assemblage of rigid particles interconnected by springs along their boundary surfaces (Fig. 2.1.(a)). The crack pattern is strongly affected by the mesh design as the cracks initiate and propagate through the interface boundaries of particles. Therefore, a random geometry of rigid particles is generated by a Voronoi diagram (Fig. 2.1.(b)), which reduces mesh bias on the initiation and propagation of potential cracks (Bolander et al. 2000).

The response of the spring model provides an insight into the interaction among the particles, which is different from models based on continuum mechanics. In this model, each rigid particle has three translational and three rotational degrees of freedom defined at the nucleus that represents the center of particles (Fig. 2.1.(a)). The boundary surface of two particles is divided into several triangles with a center of gravity and vertices of the surface as seen in the figure. One normal and two tangential springs are set at the center of each triangle. As rotation can be calculated by evaluating the change of the coordinates of two spring location, this model can automatically evaluate the effect of bending and torsional moment without the need to set any rotational springs (Yamamoto et al. 2008 and Yamamoto 2010).

(a) Rigid-Body-Spring-Model   (b) Voronoi Diagram
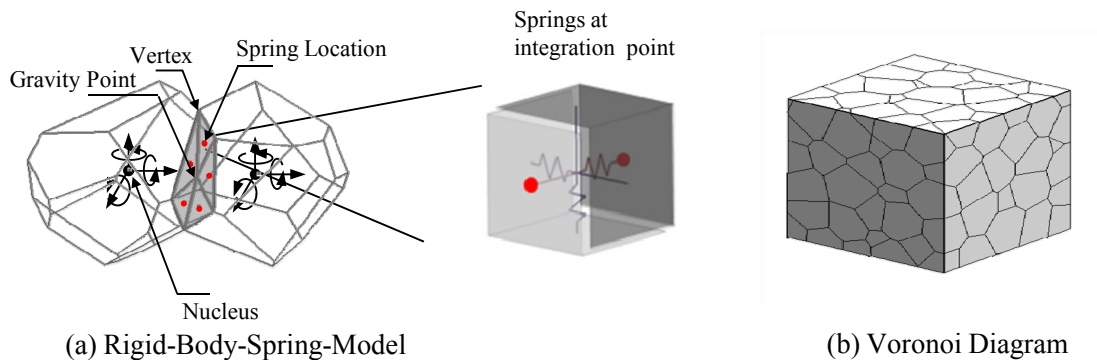
Fig. 2.1 Numerical Model 3-D RBSM

2.3 Concrete Material Model

The constitutive models for tension, compression and shear that are used in 3-D RBSM are shown in Fig. 2.2 (Yamamoto et al. 2008). The tensile model for normal springs is shown in Fig. 2.2.(a). Up to tensile strength, the tensile behavior of concrete is modeled as linear elastic and, after cracking, a bilinear softening branch according to a 1/4 model is assumed. In the model, σ_t, g_f and h represent tensile strength, tensile fracture energy, and distance

between nuclei, respectively. The model takes into consideration tensile fracture energy.

$\sigma_{tl}=0.25\sigma_t$
$\varepsilon_{tl}=0.75g_f/\sigma_t h$
$\varepsilon_{tu}=5.0\,g_f/\sigma_t h$

(a) Tensile Model of
Normal Spring

(b) Compression Model of
Normal Spring

(c) Shear Spring Model

(d) Softening Coefficient for
Shear Spring

(e) Mohr-Coulomb Criteria
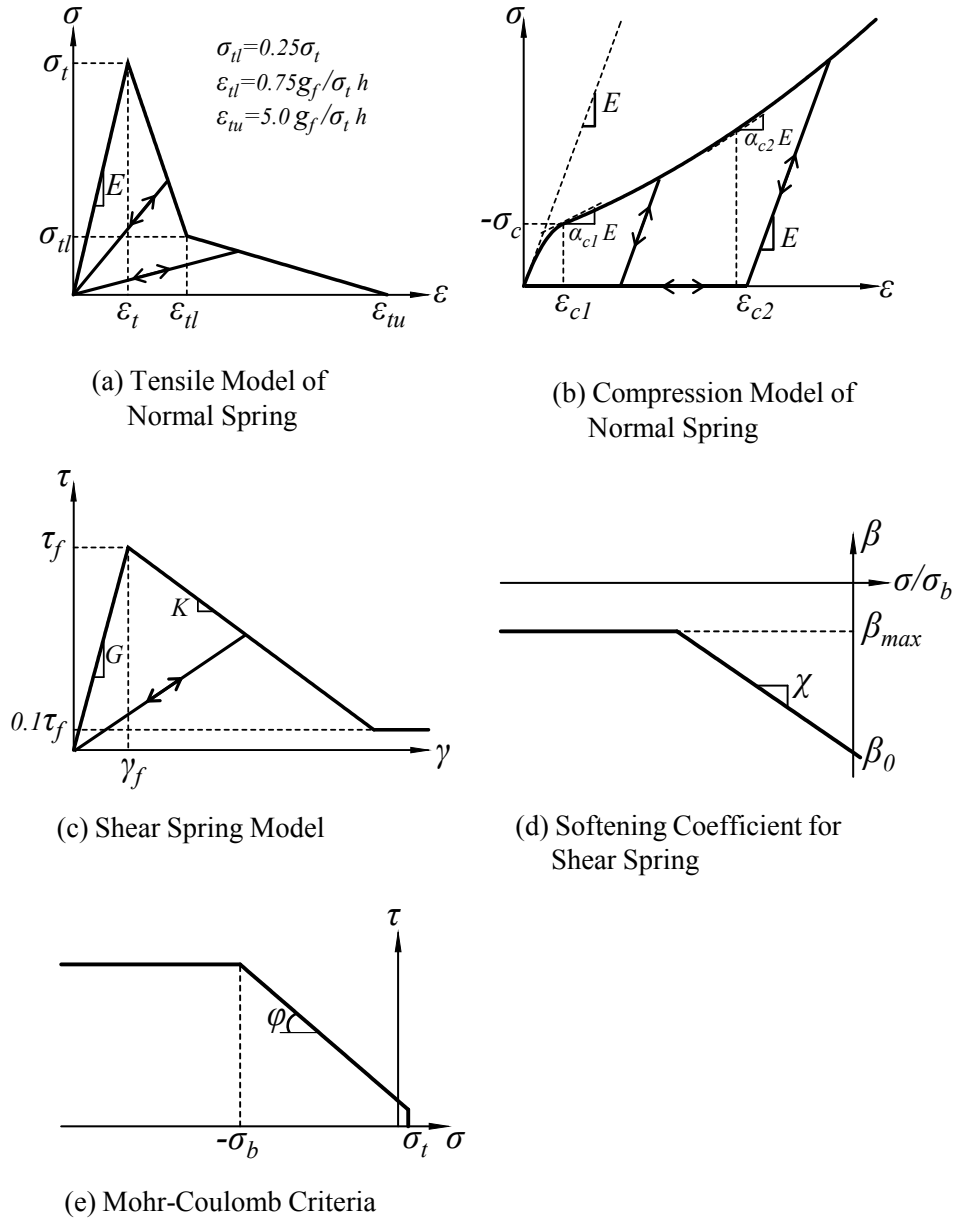
Fig. 2.2 Constitutive Models for Concrete (Yamamoto et al. 2008)

Figure 2.2.(b) shows the stress-strain relation for compression of normal springs that was modeled as an S-shape curve combining two quadratic functions given in Eq. [2.1]. The parameters of ε_{c1}, a_0, b_0, a_1, b_1 and c_1 are calculated by Eq. [2.2], based on Table 2.1, in which

each parameter has been decided by conducting parametric analyses comparing with the test results of uniaxial tension, uniaxial compression, hydrostatic compression and triaxial compression. The parametric analyses include a variety of specimen size, shape, mesh size and concrete strengths. These parameters are recommended for normal strength concrete. Moreover, the average size of the voronoi particles (mesh size) to use the parameters was recommended from 10 mm to 30 mm (Yamamoto 2010). The applicability of the parameters and concrete model will be discussed in Section 2.5.

Softening behavior is not considered in the compression model. Compressive failure of normal springs in material level does not occur in this model. However, compressive failure behavior of specimens in structural level can be simulated with a confinement effect by combination of a normal spring and a shear spring.

$$\sigma = \begin{cases} a_0\varepsilon^2 + b_0\varepsilon & (\varepsilon > \varepsilon_{c1}) \\ a_1\varepsilon^2 + b_1\varepsilon + c_1 & (\varepsilon \le \varepsilon_{c1}) \end{cases} \qquad [2.1]$$

$$\varepsilon_{c1} = -\frac{2\sigma_c}{E(1+\alpha_{c1})} \qquad [2.2.a]$$

$$a_0 = -\frac{E(1-\alpha_{c1})}{2\varepsilon_{c1}} \qquad [2.2.b]$$

$$b_0 = E \qquad [2.2.c]$$

$$a_1 = \frac{E(\alpha_{c2}-\alpha_{c1})}{2(\varepsilon_{c2}-\varepsilon_{c1})} \qquad [2.2.d]$$

$$b_1 = \frac{E(\alpha_{c1}\varepsilon_{c2}-\alpha_{c2}\varepsilon_{c1})}{\varepsilon_{c2}-\varepsilon_{c1}} \qquad [2.2.e]$$

$$c_1 = -a_1\varepsilon_{c1}^2 - b_1\varepsilon_{c1} - \sigma_c \qquad [2.2.f]$$

11

where;

E   : Young Modulus

α_{c1}, α_{c2} : Reduction factor for E at ε_{c1} and ε_{c2} respectively.

ε_{c1}, ε_{c2} : Compressive strains, and

σ_c : Stress corresponding to ε_{c1}

Table 2.1 Model Parameters (Yamamoto 2010)

Normal Spring							Shear Spring						
Young Modulus	Tensile Region		Compressive Region				Young Modulus	Fracture Criterion			Softening Behavior		
E N/mm²	*σ_t* N/mm²	*g_f* N/mm²	*σ_c* N/mm²	*ε_{c2}*	*α_{c1}*	*α_{c2}*	*η=G/E*	*c* N/mm²	*φ* degree	*σ_b* N/mm²	*β_0*	*β_{max}*	*χ*	*κ*
1.4*E**	0.80*f_t**	0.5*G_f**	*1.5f_c'**	-0.015	0.15	0.25	0.35	*0.14f_c'**	37	*f_c'**	-0.05	-0.025	-0.01	-0.3

*" *" indicates test values. E*:Young Modulus, f_t*: Tensile Strength, G_f*: Fracture Energy, f_c'*:Compressive Strength*

The stress-strain relation of shear stress represents the combination of two tangential springs. The combined shear strain is defined by Eq. [2.3], in which γ_l and γ_m represent the strains of the springs in each direction (Nagai et al. 2005). Then, combined shear stress τ is calculated from the shear stress-strain relation, and the shear stresses for each direction (τ_l and τ_m) are distributed by Eq. [2.4].

$$\gamma = \sqrt{\gamma_l{}^2 + \gamma_m{}^2}$$ [2.3]

$$\tau_l = \tau \, (\gamma_l/\gamma), \quad \tau_m = \tau \, (\gamma_m/\gamma)$$ [2.4]

where;

τ : Combined shear stress

γ : Combined shear strain

γ_l , γ_m : Shear strains in each direction, and

τ_l ,τ_m : Shear stresses in each direction

Stress-strain relationship for shear is given in Fig. 2.2.(c) and Eq. [2.5]. In the model, τ_f and γ_f represent shear strength and strain corresponding to strength, respectively. The stress elastically increases up to the shear strength with the slope of shear modulus (G) and softening behavior is also assumed. K is the shear-softening coefficient that is defined by Eq. [2.6]. It is assumed that the shear-softening coefficient K depends upon the stress of the normal spring as represented in Eq. [2.6] and Fig. 2.2.(d); where, β_0, β_{max} and χ are the parameters of dependency on the normal spring for the shear-softening coefficient.

$$\tau = \begin{cases} G\gamma & (\gamma < \gamma_f) \\ \max\left(\tau_f + K(\gamma - \gamma_f), 0.1\tau_f\right) & (\gamma \geq \gamma_f) \end{cases}$$ [2.5]

$$K = \beta G$$ [2.6.a]

$$\beta = \min\left(\beta_0 + \chi(\sigma/\sigma_b), \beta_{max}\right)$$ [2.6.b]

where;

G   : Shear modulus

τ_f : Shear Strength

γ_f : Strain corresponding to τ_f

K   : Shear-softening coefficient

$\beta_0, \beta_{max}, \chi$: Dependency parameters, and

σ_b : Compression limit value

The Mohr-Coulomb criterion is assumed as the failure criteria for the shear spring (Fig. 2.2.(e) and Eq. [2.7]), where c and φ are cohesion and the angle of internal friction, respectively. Shear strength is assumed to be constant when normal stress is greater than σ_b, which is termed the compression limit value (Yamamoto 2010). The values of the parameters

are given in Table 2.1.

$$\tau_f = \begin{cases} c - \sigma \tan\varphi & (\sigma > -\sigma_b) \\ c + \sigma_b \tan\varphi & (\sigma \le -\sigma_b) \end{cases}$$

[2.7]

where;

c   : Cohesion

φ : The angle of internal friction

Moreover, it is assumed that shear stress decreases with an increase in crack width at the cracked surface, in which tensile softening occurs in a normal spring by taken into consideration the shear deterioration coefficient β_{cr} as represented in Eq. [2.8], which is similar to Saito's model (Saito 1999 and Saito et al. 1999). Where, ε_t and ε_{tu} are cracking strain and ultimate strain in a normal spring, respectively. The unloading and reloading paths in shear springs are modeled as origin-oriented.

$$\tau = \begin{cases} \beta_{cr} G\gamma & (\gamma < \gamma_{ft}) \\ \beta_{cr} \max\left(\tau_{ft} + K(\gamma_{max} - \gamma_{ft}), 0.1\tau_{ft}\right) & (\gamma \ge \gamma_{ft}) \end{cases}$$

[2.8.a]

$$\beta_{cr} = \frac{\varepsilon_t}{\varepsilon} \exp\left\{\frac{\kappa}{\varepsilon_{tu}}(\varepsilon - \varepsilon_t)\right\}$$

[2.8.b]

$$\tau_{ft} = c - \sigma_t \tan\varphi$$

[2.8.c]

where;

β_{cr} : Shear deterioration coefficient

τ_{ft} : Shear stress at the tensile strength

γ_{ft} : τ_{ft}/G

γ_{max} : A dependency parameter

ε_t : Cracking strain

14

ε_{tu} : Ultimate strain

κ : A parameter to control shear reduction property

σ_t : Tensile strength

2.4 Reinforcement Model

Reinforcement is modeled as a series of regular beam elements (Fig. 2.3) that can be freely located within the structure, regardless of the concrete mesh design (Bolander and Hong 2002).Two translational and one rotational degrees of freedom represented by the springs are defined at each beam node. The reinforcement is attached to the concrete particles by means of zero-size link elements that provide a load-transfer mechanism between the beam node and the concrete particles (Saito 1999).

The stress-strain relation of reinforcement is defined by a bi-linear model. Crack development is strongly affected by the bond interaction between concrete and reinforcement. The bond stress-slip relation is provided in the spring parallel to the reinforcement of linked element. Figure 2.4 shows the relation that is defined by Eq. [2.9] up to the strength (Suga 2001), and the function proposed by CEB-FIB is assumed after strength (CEB 1990),

$$\tau = 0.36 f'_c{}^{2/3} \left\{ 1 - \exp\left(-40(s/D)^{0.5}\right) \right\}$$ [2.9]

where, D is diameter of the reinforcement and s represents slippage.
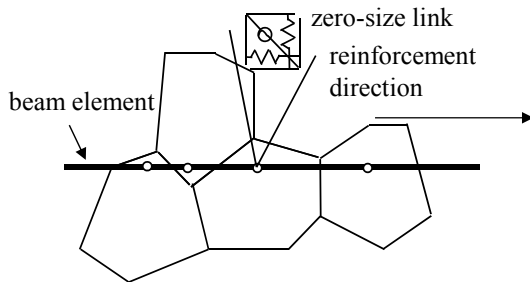
Fig. 2.3 Reinforcement Arrangement   **Fig. 2.4** Bond Stress-slip Relation
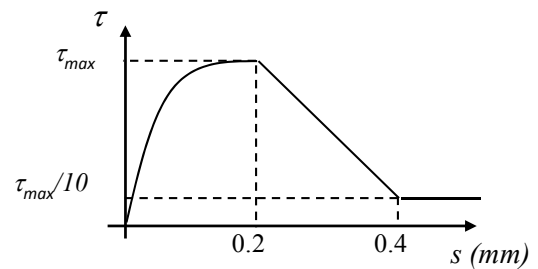
15

2.5 Applicability of the Model

2.5.1 Uniaxial Compression

The applicability of this model is shown by a 3-D RBSM simulation of uniaxial compressive cylinder. To achieve that, a cylinder with a diameter of 150 mm and a height of 600 mm was analyzed, and the results were compared with the test performed by Nakamura and Higai (2001). The average size of the voronoi particles in the analysis was 22 mm. The compressive strength of concrete was 18.85 MPa. In the experiment, strain distribution along the axial direction was measured using the deformed acrylic bar method and localized behavior was observed in the post-peak region. Figure 2.5 shows the comparison of load-displacement curves between the numerical and the experimental results. As seen in the figure, a reasonably good agreement is obtained. A comparison of axial strain distribution is given in Fig. 2.6. Axial strain distributions having a range from pre-peak to further post-peak region are given at displacements of 1.0, 1.5 and 2.0 mm. A similar localized behavior between the experiment and 3-D RBSM analysis is obtained. Figure 2.7 shows the 3-D deformed shapes obtained from 3-D RBSM. The deformation was magnified by a factor of 30 in order to observe the 3-D deformation clearly. As shown in the figure, a 3-D RBSM can simulate localized compressive failure reasonably well.
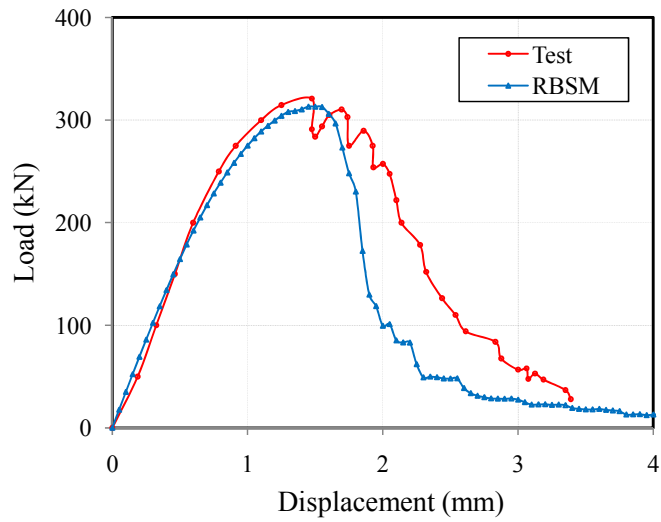
Fig. 2.5 Comparison of Experimental (Nakamura and Higai 2001) and Numerical Load-Displacement Curves of Cylinder in Compression
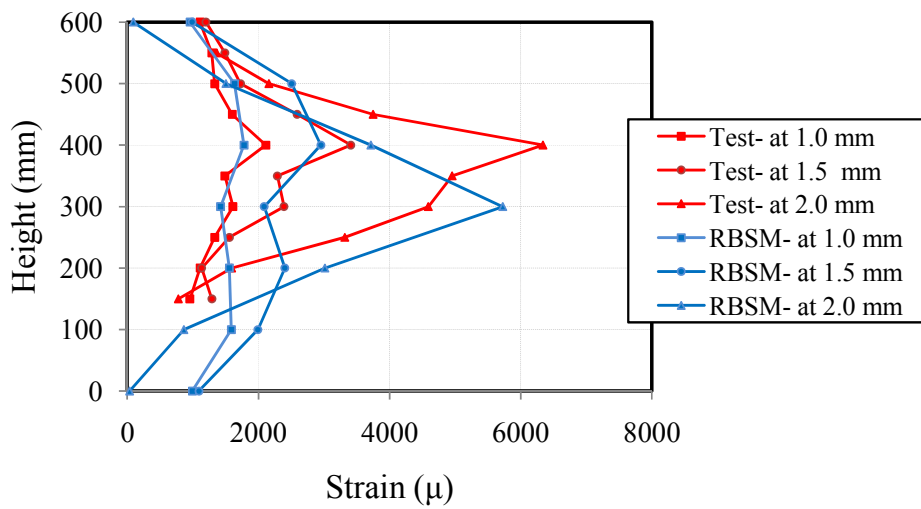
Fig. 2.6 Comparison of Experimental (Nakamura and Higai 2001) and Numerical Axial Strain Distribution Results

17

1 mm   1.50 mm   2 mm
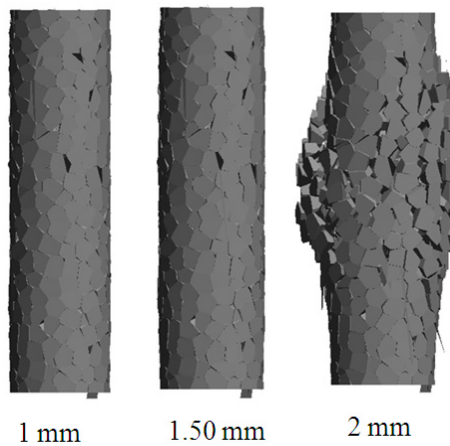
Fig. 2.7 3-D Deformed Shapes

2.5.2 Triaxial Compression

Yamamoto et al. (2008) confirmed the applicability of 3-D RBSM under a triaxial stress state by simulating the experiment of Kotsovos and Newman (1978). Figure 2.8 shows 3-D RBSM analysis of a cylinder having a diameter of 100 mm and a height of 250 mm. An numerical model of the cylinder is shown in Fig. 2.8.(a). Figure 2.8.(b) shows a comparison of the axial stress-axial strain and the axial stress-lateral strain relation under various lateral pressures. The experimental and numerical stress-strain curves and maximum stress values agreed significantly well as shown. Only for the high confinement of 70 MPa, the numerical stress-strain curves show strain hardening as opposed to the experiments. However, the maximum stress agreed with the experiment. The results show that the dilatancy and confinement effect can be simulated by the 3-D RBSM.

Therefore, the compressive failure simulation capability of the concrete material model of 3-D RBSM is confirmed.

18

(a) Numerical Model   b) Stress-Strain Relation
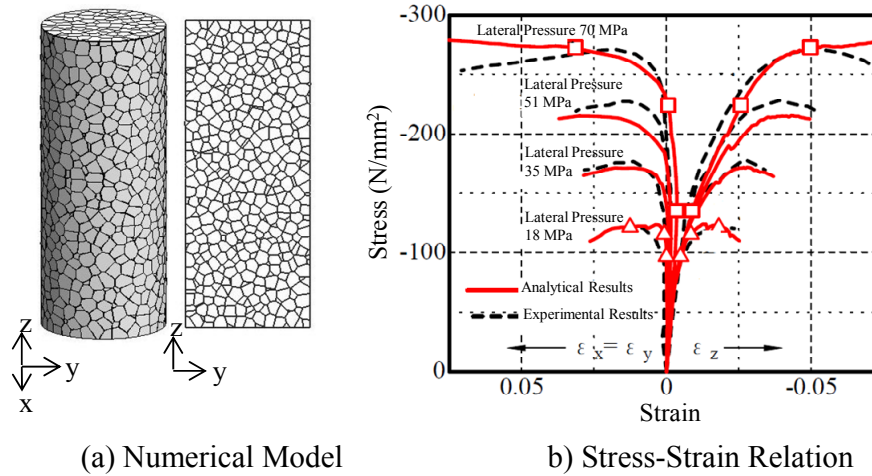
Fig. 2.8 Comparison of Experimental Results (fc' = 46.9 MPa ,(Kotsovos and Newman (1978)) and 3-D RBSM Results (Yamamoto et al. 2008)

2.6 Calibration of Model Parameters for Deep Beams

The parameters given in Table 2.1 should be calibrated while applying them to the structural level. This study mainly focuses on the simulation of deep beams. Therefore, the parameters of σ_b and E given in Table 2.1 are calibrated for deep beams. Figure 2.9 shows the parameter of σ_b due to $f_c'^*$ that is used in this study. Moreover, the parameter of E is used as $1.0E^*$ for the specimens having $f_c'^*$ more than 20 MPa. The applicability of these parameters is confirmed by compression cylinder analyses for specimens with different $f_c'^*$ values that are used in this study and given in Appendix B.
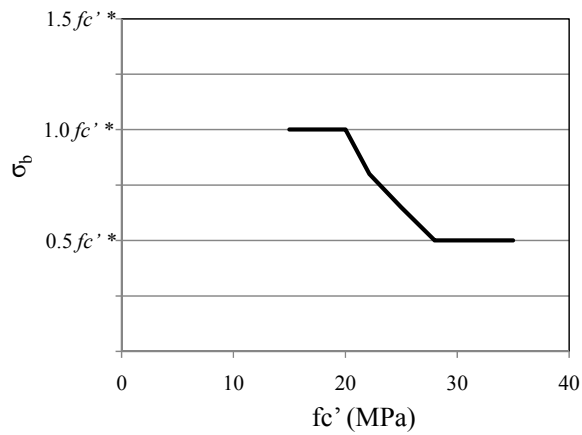
Fig. 2.9 Model Parameter of σ_b for Deep Beams

2.7 Summary and Conclusions

In this chapter, a general explanation of 3-D RBSM is introduced. The tensile, compression and shear constitutive models of concrete and the reinforcement model of the numerical tool are explained. The applicability of 3-D RBSM is verified by the uniaxial and triaxial compression cylinder analyses. A good agreement in terms of load-displacement curves, 3-D deformed shapes and axial strain values between the experimental and numerical results are introduced in uniaxial compression analyses. Moreover, the triaxial compression analysis shows that 3-D RBSM can simulate the dilatancy and confinement effect.

3. *Applicability of 3-D RBSM on Deep Beams*

3.1 Introduction

The purpose of this chapter is to verify the applicability of 3-D RBSM on deep beams. In order to achieve that, a series of deep beam with and without stirrup and having a/d=0.5 to 2.0 is tested and the experimental results are presented. Then, tested specimens are also analyzed by the numerical tool of 3-D RBSM. The experimental and the numerical results obtained from 3-D RBSM are compared in terms of load-displacement curves, crack patterns as well as the strain of stirrups. Therefore, the applicability of 3-D RBSM on deep beams are confirmed.

3.2 Experimental Program

Four groups of deep beams with a/d=0.5, 1.0, 1.5 and 2.0 as described in Table 3.1 are designed and tested. Each group has two beams with and without stirrup. The dimensions and details of the specimens are given in Fig. 3.1. The plate width is 100 mm in each specimen. The cross-sectional area, longitudinal reinforcement ratio (ρ_t) and plate widths are the same in all cases.

Mixture proportion of concrete is given in Table 3.2. The same mixture proportion was used for all specimens, however the casting dates and the durations between casting and tests were different. Specimens were cured with water after remolding.

Table 3.1 Specimens Details

Specimen	a/d	Effective Depth d (mm)	Shear Span a(mm)	Longitudinal Reinforcement			Stirrup				fc' MPa	Peak Loads (kN)	
				As mm^2	fy N/mm^2	ρ_t (%)	Type	fyw N/mm^2	Spacing (mm)	ρ_w (%)		Experimental	Numerical
B3-0.5	0.5	240	120				-	388.2	-	-	32.6	601	662
B3-0.5-VS	0.5	240	120				D6	388.2	70	0.9	32.6	658	598
B3-1.0	1.0	240	240				-	388.2	-	-	35.7	452	402
B3-1.0-VS	1.0	240	240	774.2 (2D22)	372.2	3.23	D6	388.2	70	0.9	35.7	465	470
B3-1.5	1.5	240	360				-	388.2	-	-	22.2	209	193
B3-1.5-VS	1.5	240	360				D6	388.2	70	0.9	22.2	274	294
B3-2.0	2.0	240	480				-	388.2	-	-	22.2	130	146
B3-2.0-VS	2.0	240	480				D6	388.2	70	0.9	22.2	221	256

(a) a/d=0.5

(c) a/d=1.5

G1 : Gauge 1
G2 : Gauge 2
[Unit: mm]

(b) a/d=1.0

(d) a/d=2.0

Fig. 3.1 Overview of Specimens

Table 3.2 Concrete Mixture Proportion

G_{max}	Water-Cement Ratio	Mass Per Unit Volume (kg/m^3)			
(mm)	W/C (%)	Water W	Cement C	Sand S	Gravel G
15	0.56	166	294	779	990

* An admixture was used having an amount of 0.4% of Cement

Figure 3.2 shows the experimental setup for four-point loading that was applied to the test specimens. The load was distributed to the bearing plates using a steel beam. Steel rollers were used between the loading plates and the steel beam. A mid-span and support deflections were measured and a relative mid-span deflection was taken into consideration by subtracting the support displacements. In the experiment, the strain gauges, of which locations are labeled as 'G1' and 'G2'in Fig. 3.1, were attached to the stirrups in order to measure the strain values.
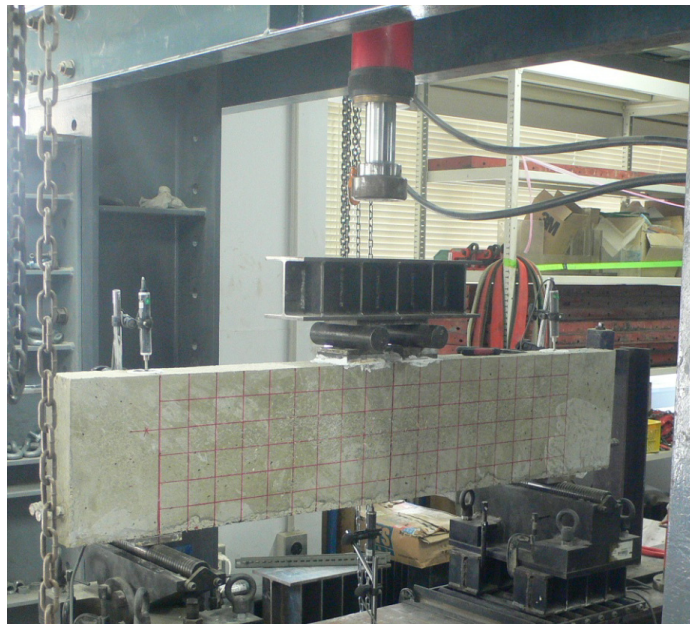
Fig. 3.2 Experimental Setup

3.3 Experimental Results

3.3.1 a/d=0.5 Case

The load-displacement curve of B3-0.5 specimen is shown by the dashed line in Fig. 3.3. The peak load is 662 kN. Figure 3.4.(a) shows the crack pattern of the beam from crack initiation to the failure. Crack pattern figures are given from pre-peak to post-peak loads in four steps labeled as 'a,b,c and d', which are also labeled in the load displacement curves (see Fig. 3.3). A mid-span bending crack occur at P=100 kN and then, first shear cracks were formed in the lower part of the struts at P=250 kN (a). Shear cracking was propagated at P=500 kN (b). At the peak load, a shear crack was formed from outer side of the bearing plate and the beam failed in shear compression with spalling of the concrete (c). In the post-peak region, the spalling of concrete-indicated by the shaded areas- and lateral deformation increased (d) and developed along the entire strut as shown in the figure. Failure pattern of the specimen is given in Fig. 3.5.

The load-displacement curve of the B3-0.5-VS specimen is shown by the solid line in Fig. 3.3. The peak load is 598 kN, which is smaller than B3-0.5 case. That is, the vertical stirrup is not effective.

Figure 3.4.(b) shows the crack pattern of B3-0.5-VS specimen. A mid-span bending crack occur at P=100 kN. The first shear crack was formed at P=200 kN and another shear cracks were developed at P=250 kN (A). Shear cracking was propagated at P=500 kN (B) and at the peak load; similarly with B3-0.5 case, a shear crack was formed from outer side of the bearing plate and the shear compression failure with spalling of the concrete was observed (C). In the post-peak region (D), concrete spalling was propagated along the entire strut, which is similar with B3-0.5 case. Failure pattern of the specimen is given in Fig 3.6.

24
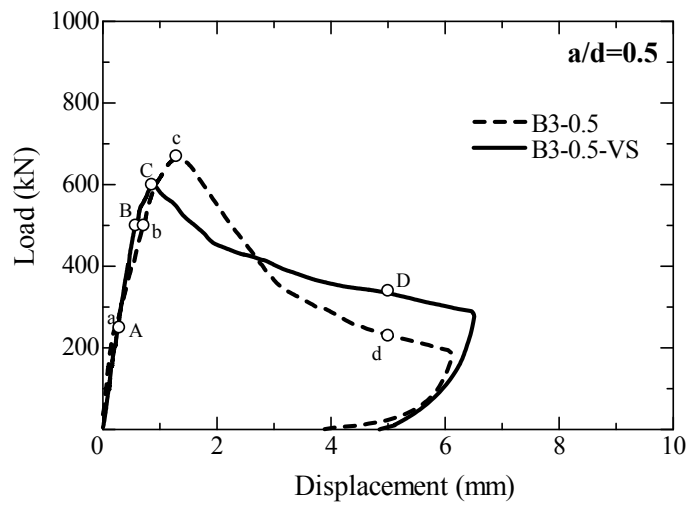
Fig. 3.3 Load-Displacement Curves (a/d=0.5)

(a) B3-0.5   (b) B3-0.5-VS
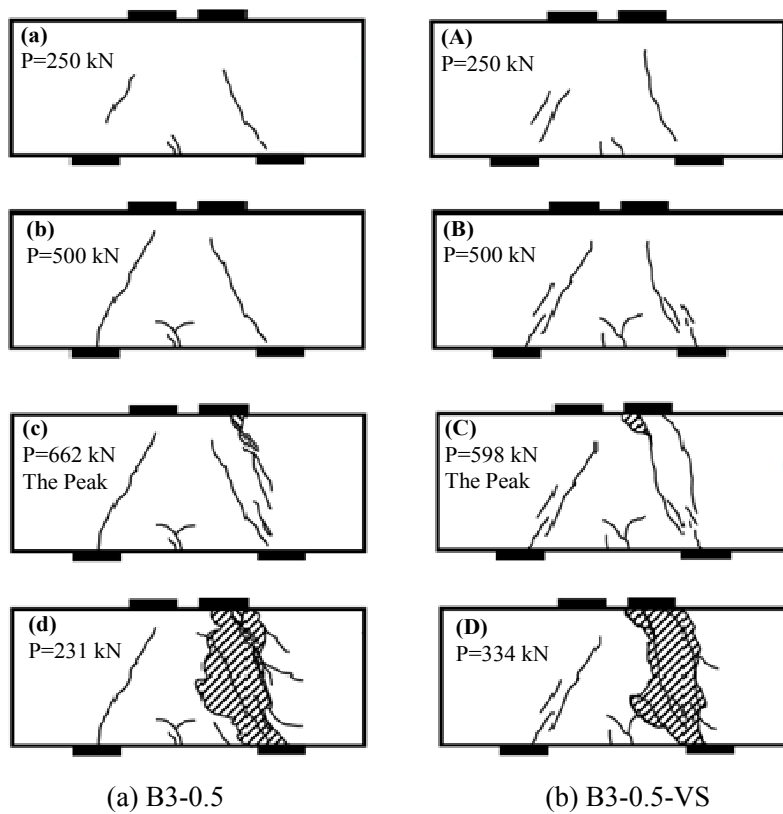
Fig. 3.4 Crack Pattern (a/d=0.5)
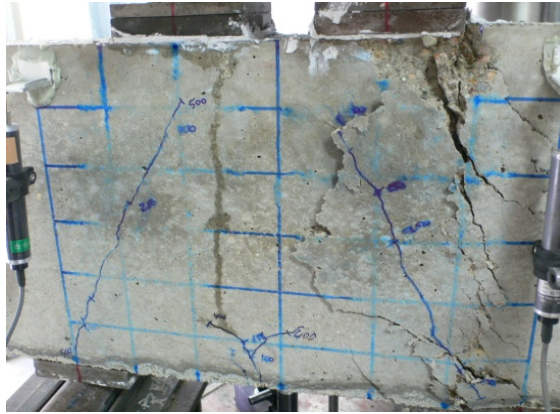
Fig. 3.5 Failure of B3-0.5

Fig. 3.6 Failure of B3-0.5-VS

Figure 3.7 gives strain of vertical stirrups. The strain measurement points are labeled in Fig. 3.1. As seen in the Fig. 3.7, the vertical stirrups did not yield before the peak load. On the other hand, the stirrup yielded in the post-peak region that is the reason of more ductile behavior in the load displacement curve of BS3-0.5-VS specimen in the post-peak region (see Fig. 3.3).
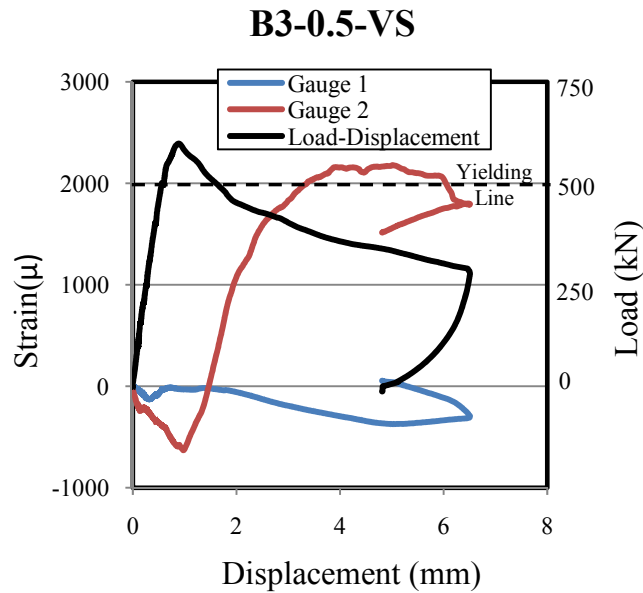
B3-0.5-VS

Fig. 3.7 Strain of Stirrups (B3-0.5-VS)

3.3.2 a/d=1.0 Case

Figure 3.8 shows the load-displacement curve of B3-1.0 specimen given by dashed line. The peak load is 452 kN. The crack pattern of the beam is given in Fig. 3.9.(a). Firstly, a mid-span bending crack occur and then, a shear crack was formed at P=150 kN (a). Shear cracking was propagated in the two struts at P=300 kN (b). At the peak load (c), a shear crack was developed from support to bearing plate and the beam suddenly failed in shear compression with spalling of the concrete (d). Failure pattern of the specimen is given in Fig 3.10.
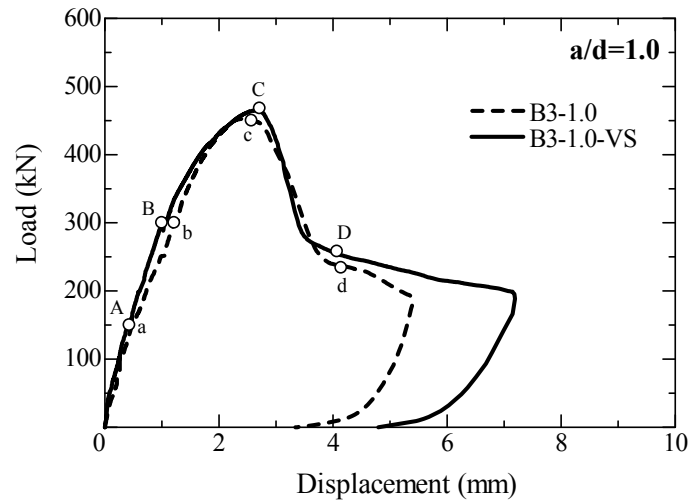
Fig. 3.8 Load-Displacement Curves (a/d=1.0)

The load-displacement curve of the B3-1.0-VS specimen is shown by the solid line in Fig. 3.8. The peak load is 465 where it is 452 kN in B3-1.0 case. That is, there is no significant effect of vertical stirrup.

Figure 3.9.(b) shows the crack pattern of B3-1.0-VS specimen. After mid-span bending cracks occur (A), the first shear cracks were formed on the lower part of the struts at P=200 kN. Then, shear cracks were propagated and new shear cracks were formed at P=300 kN (B). Finally, a shear crack connected to the outer side of the bearing plate developed at the peak load (C), that led to shear compression failure with spalling of the concrete (D). Failure pattern of the specimen is given in Fig 3.11.

(a) B3-1.0   (b) B3-1.0-VS
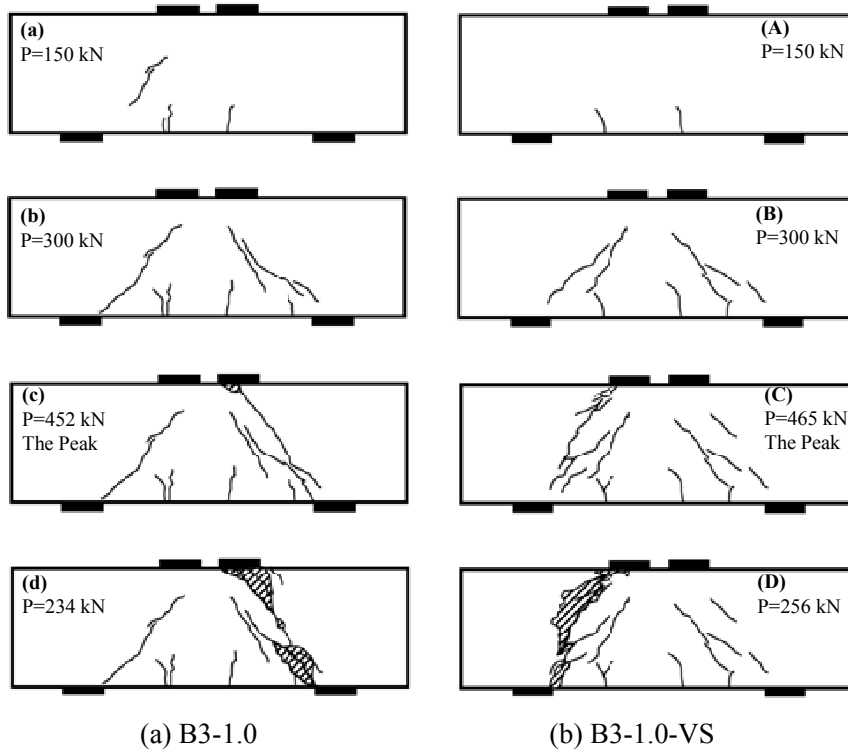
Fig. 3.9 Crack Pattern (a/d=1.0)

Fig. 3.10 Failure of B3-1.0
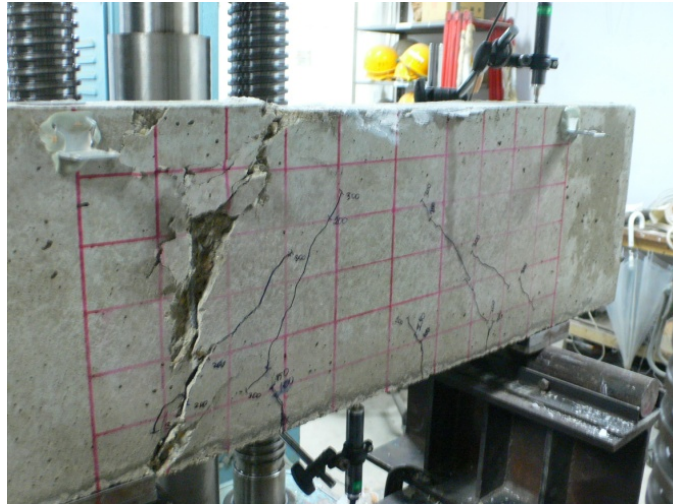
Fig. 3.11 Failure of B3-1.0-VS

The strain of vertical stirrups is given in Fig. 3.12. As seen in the figure, the vertical stirrups did not yield, that is not effective. However, it approaches to the yielding strain near the peak load.
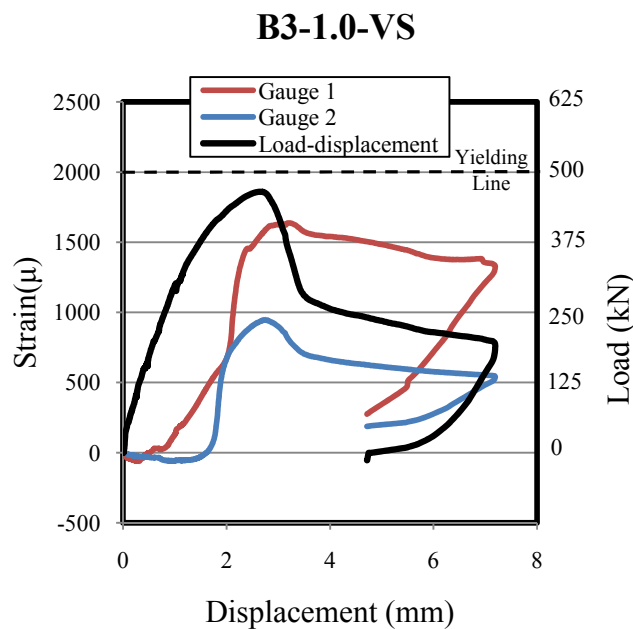
Fig. 3.12 Strain of Stirrups (B3-1.0-VS)

3.3.3 a/d=1.5 Case

The load-displacement curve of B3-1.5 specimen is shown by the dashed line in Fig. 3.13. The peak load is 209 kN. The crack pattern of the beam is given in Fig. 3.14.(a). A mid-span bending crack occur at P=70 kN and then, the first shear crack was formed at P=80 kN (a) with several bending cracks. At P=150 kN (b), a shear crack also developed in the other strut. At the peak load (c), the shear crack was propagated by connecting support and bearing plates that led to the sudden diagonal shear failure of the beam with spalling of concrete near the bearing plate. Failure pattern of the specimen is given in Fig 3.15.
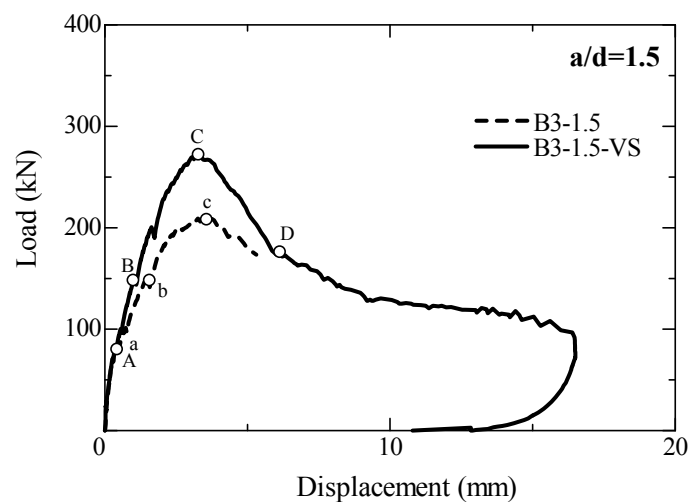
Fig. 3.13 Load-Displacement Curves (a/d=1.5)

The load-displacement curve of B3-1.5-VS specimen is shown by the solid line in Fig. 3.13. The peak load is 274 kN. That is, the vertical stirrup is effective in this case.

Figure 3.14.(b) shows the crack pattern of B3-1.5-VS specimen. A mid-span bending crack occur at P=70 kN and then, the first shear crack was formed at P=80 kN (A) with several bending cracks. A shear crack also developed in the other strut at P=150 kN (B). At

the peak load (C), several shear cracks were formed within the strut and the diagonal shear failure occurred with concrete spalling within the upper part of the strut (D). Failure pattern of the specimen is given in Fig 3.16.

| (a) B3-1.5 | (b) B3-1.5-VS |
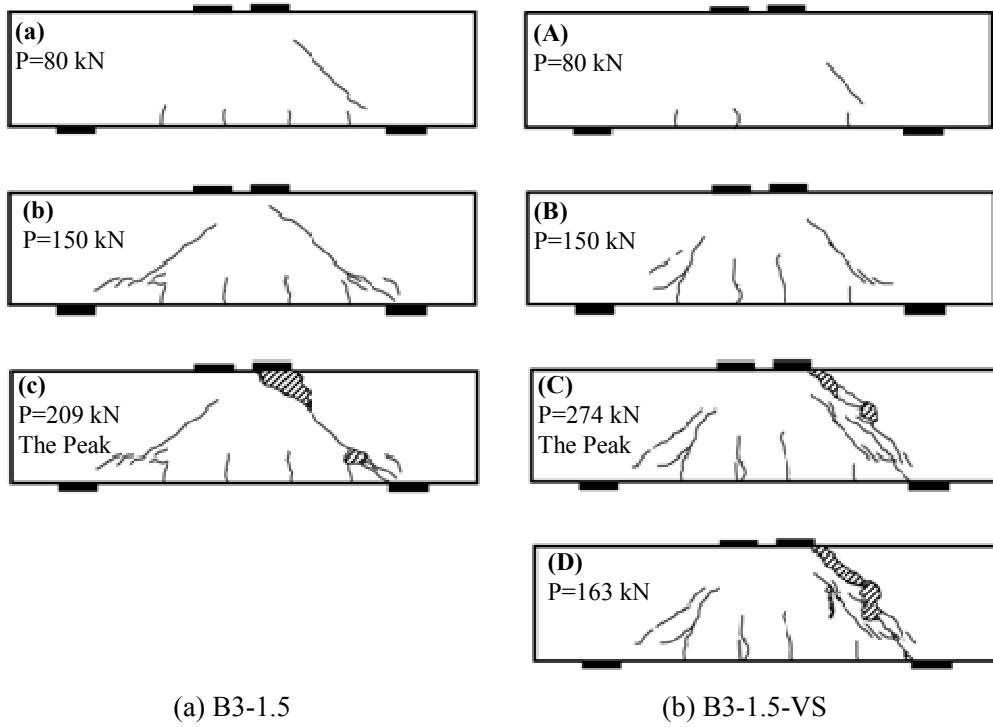
Fig. 3.14 Crack Pattern (a/d=1.5)
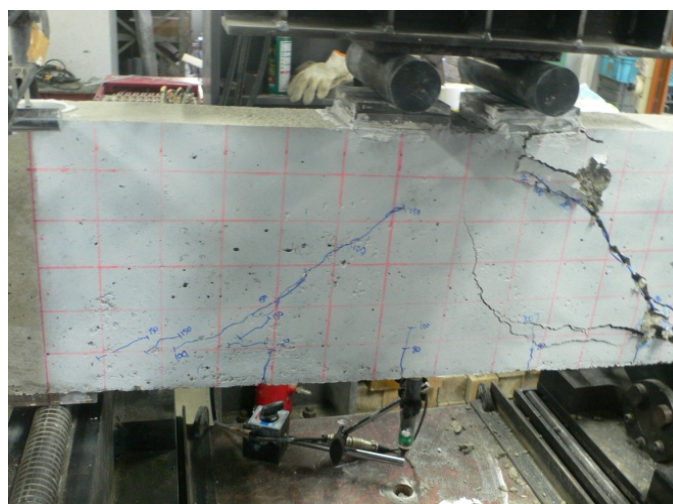
Fig. 3.15 Failure of B3-1.5
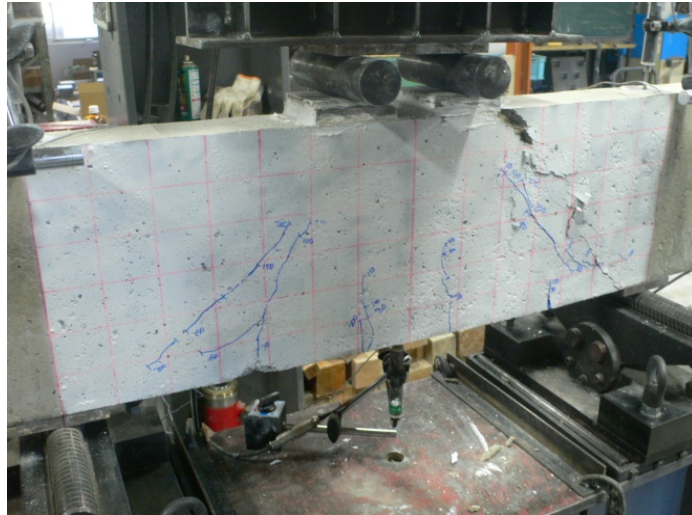
Fig. 3.16 Failure of B3-1.5-VS

Figure 3.17 gives strain of vertical stirrups. As seen in the figure, one of the vertical stirrups yielded before the peak load and then the strain rapidly reached to the value of 20840μ at the peak load.
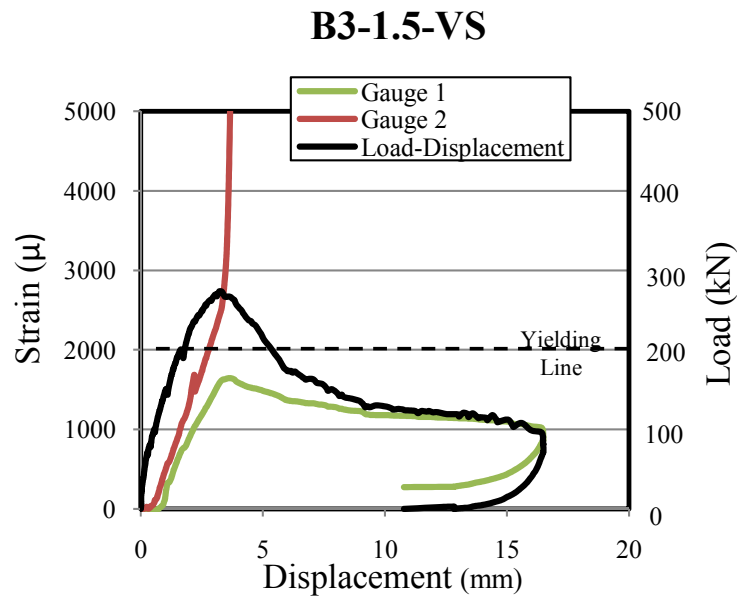
Fig. 3.17 Strain of Stirrups (B3-1.5-VS)

3.3.4. a/d=2.0 Case

The load-displacement curve of the B3-2.0 specimen is shown by the dashed line in Fig.3.18. The peak load is 130 kN. The crack pattern of the beam is given in Fig. 3.19.(a). A mid-span bending crack occur at P=50 kN and then, the first shear crack was formed at P=70 kN (a) with several bending cracks. At P=100 kN (b), shear cracks were propagated and at the peak load (c), one of the shear cracks was connected to the bearing plate that led to the sudden diagonal shear failure of the beam with small amount of concrete spalling near bearing plate. Failure pattern of the specimen is given in Fig. 3.20.

The load-displacement curve of B3-2.0-VS specimen is shown by the solid line in Fig. 3.18. The peak load is 221 kN. That is, the vertical stirrup provides significant increase in the load as seen in the figure.

Figure 3.19.(b) shows the crack pattern of B3-2.0-VS specimen. Firstly, mid-span bending cracks occur at P=50 kN and then, the first shear crack was formed at P=70 kN (A). At P=100 kN (B), a shear crack was also formed on the other strut. At the peak load (C), the shear cracks were propagated and connected to the bearing plate and the diagonal shear failure occurred (D) with concrete spalling near the bearing plate. Failure pattern of the specimen is given in Fig 3.21.
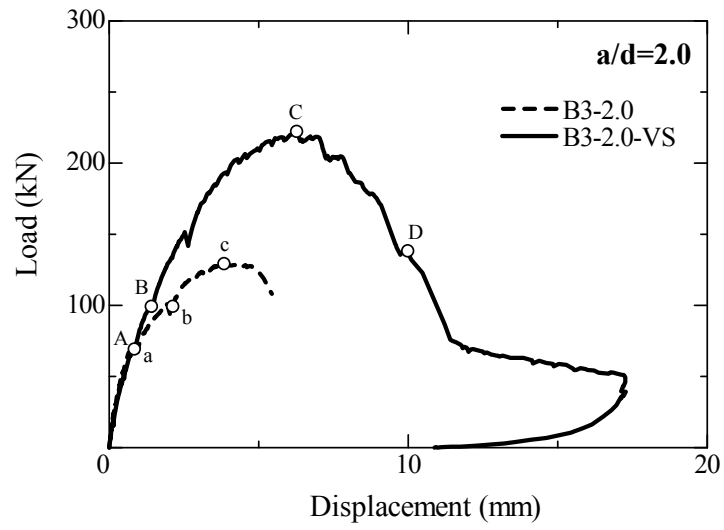
Fig. 3.18 Load-Displacement Curves (a/d=2.0)
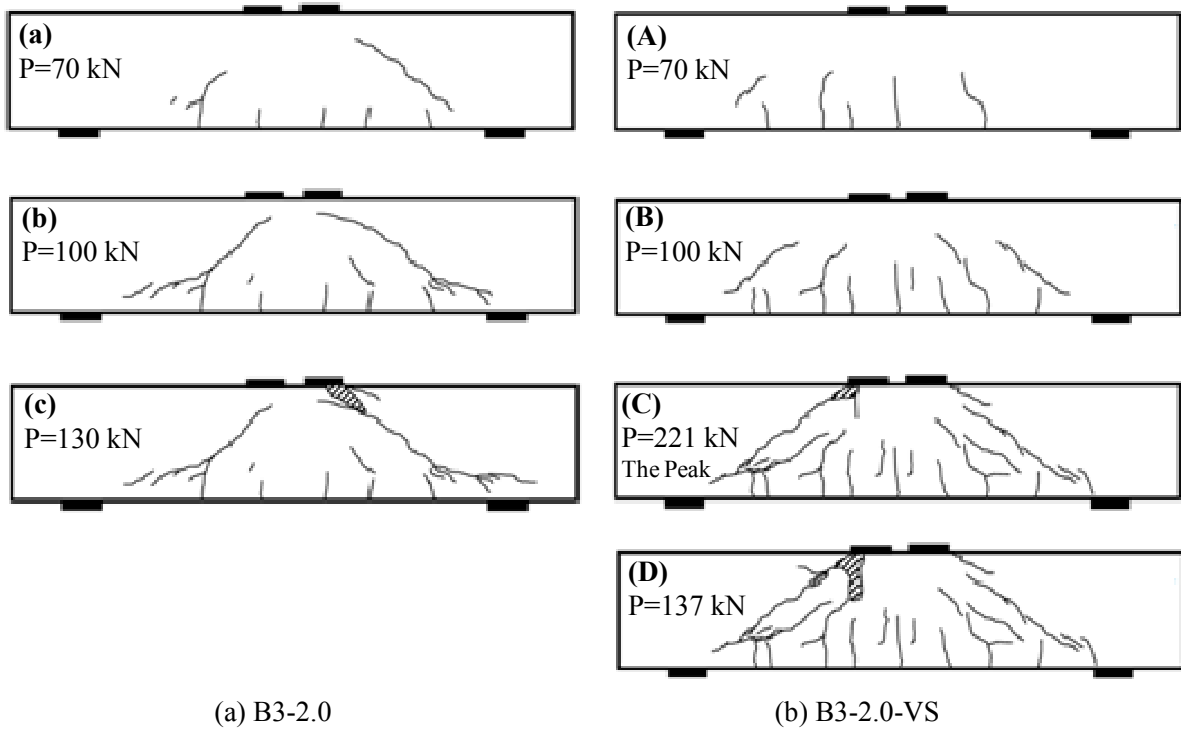
(a) B3-2.0   (b) B3-2.0-VS

Fig. 3.19 Crack Pattern (a/d=2.0)

Fig. 3.20 Failure of B3-2.0

Fig. 3.21 Failure of B3-2.0-VS

Figure 3.22 gives the strain of vertical stirrups. The both stirrups yielded before the peak load. As seen in the figure, the strain of the stirrup on the one side suddenly increased and reached to the value of 6743μ near the peak load. That is, the stirrups are significantly effective in a/d=2.0 case.
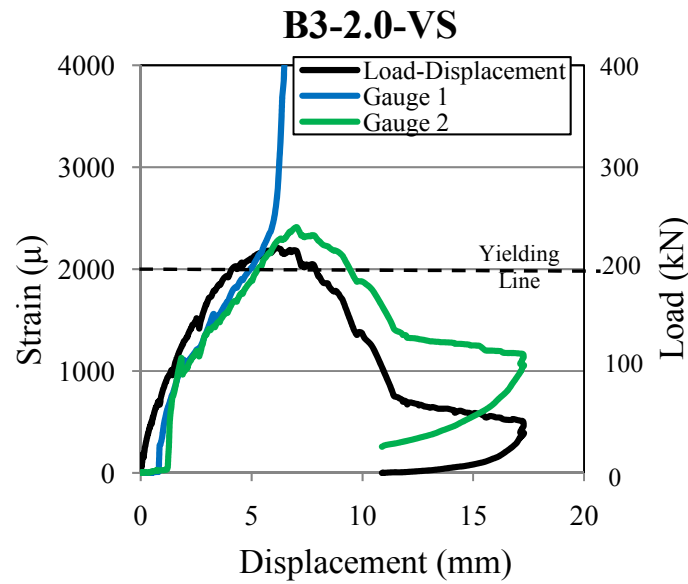
Fig. 3.22 Strain of Stirrups (B3-2.0-VS)

3.4 Comparison of Experimental and Numerical Results

The tested beams are also simulated by 3-D RBSM and the applicability of 3-D RBSM on deep beams is confirmed in this section by comparing the experimental and numerical results in terms of the load-displacement curves, crack patterns and strain of the stirrups. A representative numerical model of a deep beam is given in Fig. 3.23. In the model, bearing and support plates are modeled separately as seen in the figure. The boundary conditions are the same with a simple beam that is the translation at one support is fixed and at another support is free along x direction. The loading condition is the displacement control. The same numerical modeling is used for all numerical analyses in this study. In this chapter, the mesh size used was 20 mm in the numerical analyses.
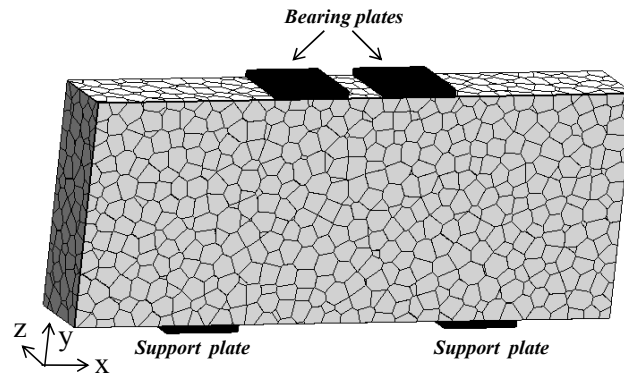
Fig. 3.23 Numerical Modeling by 3-D RBSM

3.4.1 a/d=0.5 Case

The experimental and the numerical load-displacement curves for B3-0.5 and B3-0.5-VS are given in Fig. 3.24. Total shear force calculated by Niwa's equation (1983) given in Eq. [3.1] for no stirrup case is also indicated in the figure in order to verify the numerical results. The peak load values are shown in Table 3.1. In the experiment, the peak load decreases in B3-0.5-VS case. The reason may be the reduction of the effective beam width caused by stirrup arrangement. That is a smaller effective beam width remained that led to decrease in load. On the other hand, this effect is not considered in the analysis and the numerical peak load increases in B3-0.5-VS compared to B3-0.5 case. The reason will be discussed in Chapter 4.
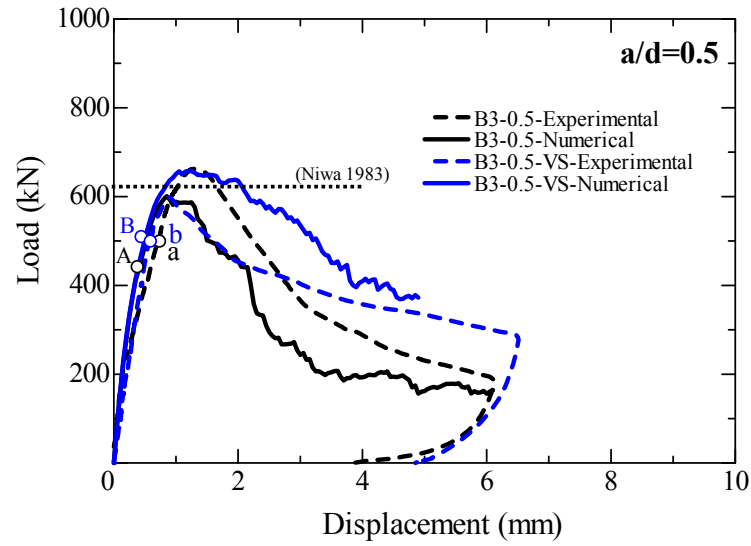
Fig. 3.24 Load Displacement Curves (a/d=0.5)

$$V_{cal1} = \frac{0.24 f_c'^{2/3} \cdot \left(1 + \sqrt{100 p_t}\right) \cdot (1 + 3.33\ r/d)}{1 + (a/d)^2} \, b_w \cdot d \qquad [3.1]$$

where;

V_{cal1} : Shear Capacity of Deep Beam (N)

b_w : Beam width (mm)

f_c' : Compressive strength of concrete (N/mm^2)

p_t : Longitudinal tension reinforcement ratio

d   : Effective depth (mm)

r   : Plate width (mm), and

a   : Shear Span (mm)

The comparison of the experimental and numerical crack pattern of B3-0.5 and B3-0.5-VS is shown in Fig. 3.25. The crack patterns are given in two steps: at a shear cracking propagation in pre-peak P=500 kN (labeled 'a' and 'A' for the experiment and the analysis

39

respectively) and at the peak load (b,B). In this section, the numerical crack pattern figures are magnified by a factor (M.F.) that is indicated in each figure. In the experiment, the crack pattern is similar in both B3-0.5 and B3-0.5-VS cases. That is, there is no significant effect of stirrups on the crack pattern. On the other hand, the numerical results agree significantly well with the experimental ones for B3-0.5 and B3-0.5-VS as seen in the figure.

Experimental   **Numerical**

P=500 kN (a)   P=435 kN (A)

The peak P=662 kN   The peak P=601 kN

(a) B3-0.5

Experimental   **Numerical**

P=500 kN (b)   P=505 kN (B)

The peak P=598 kN   The peak P=658 kN
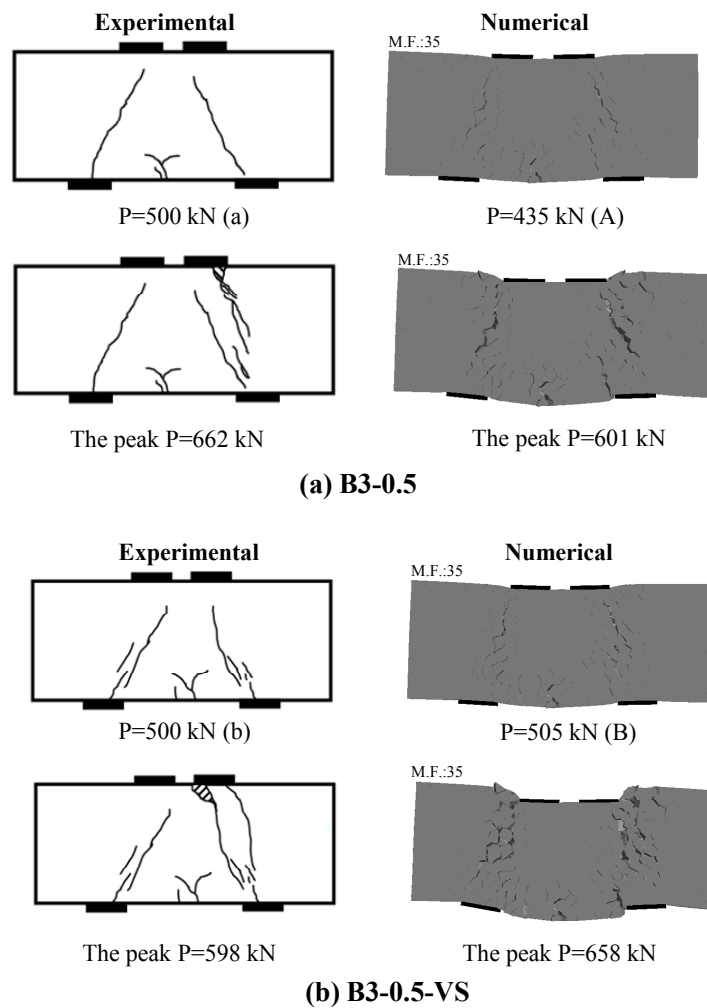
(b) B3-0.5-VS

Fig. 3.25 Crack Pattern (a/d=0.5)

Figure 3.26 shows the comparison of stirrup strains between the analysis and the experiment for B3-0.5-VS specimen. The measurement locations in the experiment are

labeled as 'G1' and 'G2'in Fig. 3.1. On the other hand, the numerical strain is given in the range of the one-third to two-third height of the stirrups at several points rather than only on the middle height of the stirrups, since the strain values are influenced by the crack location. The indices 'L' and 'R' represent the two sides of the beam that are also labeled in Fig. 3.1. The same procedure also used for numerical strain curves of B3-1.0-VS, B3-1.5-VS and B3-2.0-VS in this section. As seen in Fig. 3.26, a reasonable agreement between the experiment and the analysis is observed even in the post-peak region. Moreover, the difference between the strain values in the given range is small. This means that the localization of the damage on a crack with a large width does not occur and a strut behavior is dominant around the shear crack.
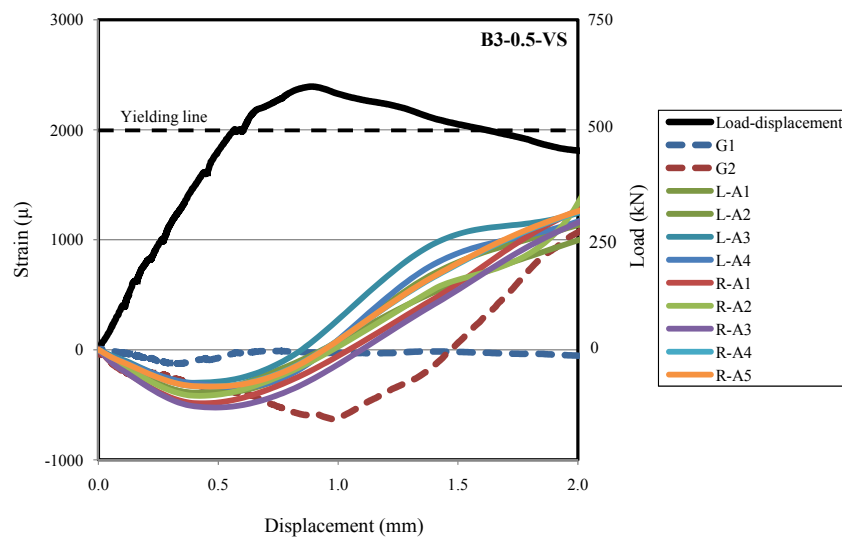
Fig. 3.26 Strain of Stirrups **(**B3-0.5-VS)

3.4.2 a/d=1.0 Case

The comparison of the numerical and experimental load-displacement curves for B3-1.0 and B3-1.0-VS are given in Fig. 3.27. In the experiment, B3-1.0 and B3-1.0-VS show similar behavior as seen in the figure. On the other hand, the numerical peak load increases in

B3-1.0-VS compared to B3-1.0 case. As seen in the figure, the numerical peak load of B3-1.0 is lower than the experimental one. However, it is similar with the shear strength equation of Niwa (1983) that is also labeled in the figure. Moreover, the initial stiffness and the stiffness after cracking are larger in the analysis; however, the initial stiffness agrees with the theoretical value calculated by the Timoshenko beam theory.
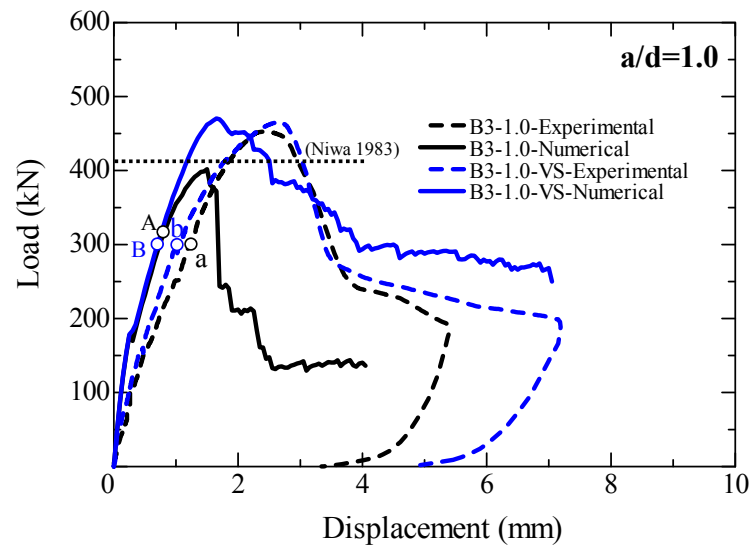
Fig. 3.27 Load Displacement Curves (a/d=1.0)

The comparison of the experimental and the numerical crack pattern for B3-1.0 and B3-1.0-VS cases is given in Fig. 3.28. In the experiment, the number of shear cracks slightly increase on both shear span in B3-1.0-VS due to the stirrup effect. The B3-1.0 specimen suddenly failed in the shear compression and also the shear compression failure occurred in B3-1.0-VS case. In the analysis, several shear cracks occurred on the one shear span of the beam where only one main crack occurred on the other shear span of B3-1.0 specimen that is similar with the experiment. On the other hand, several shear cracks are observed on both shear spans due to the stirrup effect in B3-1.0-VS. That is a good agreement between the numerical and experimental crack pattern and failure modes is obtained.
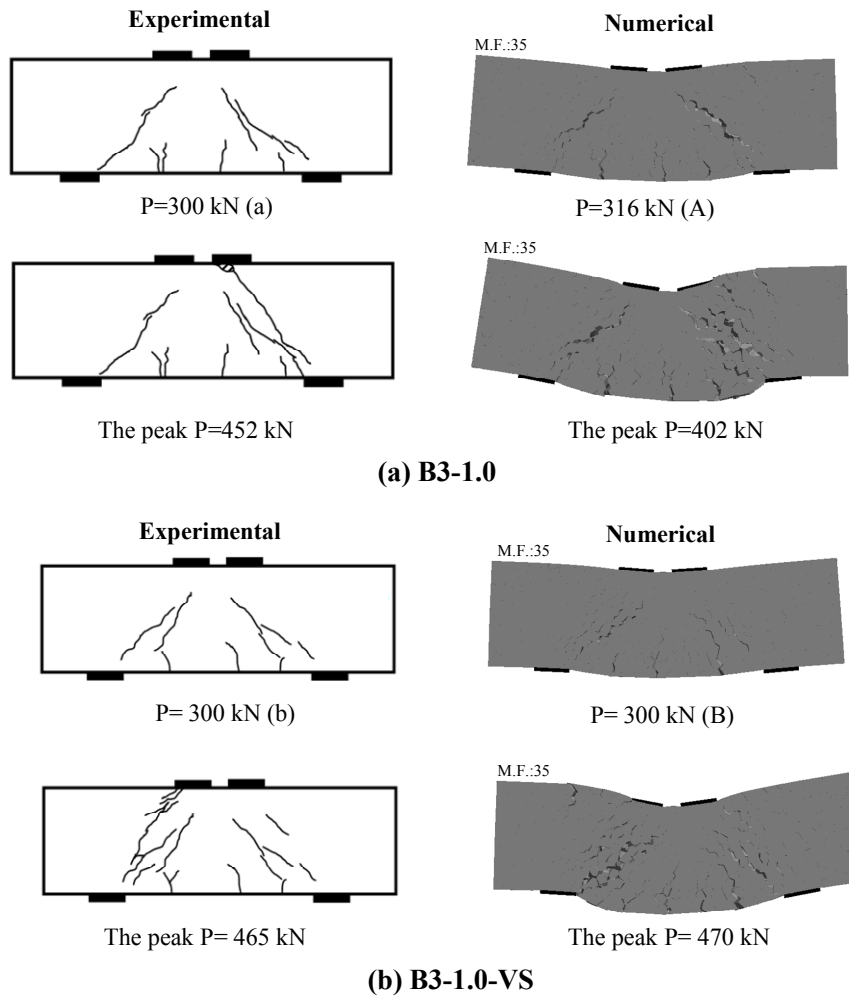
Fig. 3.28 Crack Pattern (a/d=1.0)

The comparison of stirrup strain between the analysis and the experiment for B3-1.0-VS specimen is given in Fig. 3.29. Similarly with the experimental results, stirrups do not yield before the peak in the analysis. Moreover, the numerical results agree significantly well with the experimental results. Comparing the strain range in the side "R", the range of strain values in the side "L" is expanded since the failure occured on this side. However, the range is still relatively small, that is the strut behavior is also dominant around the shear crack for a/d=1.0 case similar with the a/d=0.5 case.
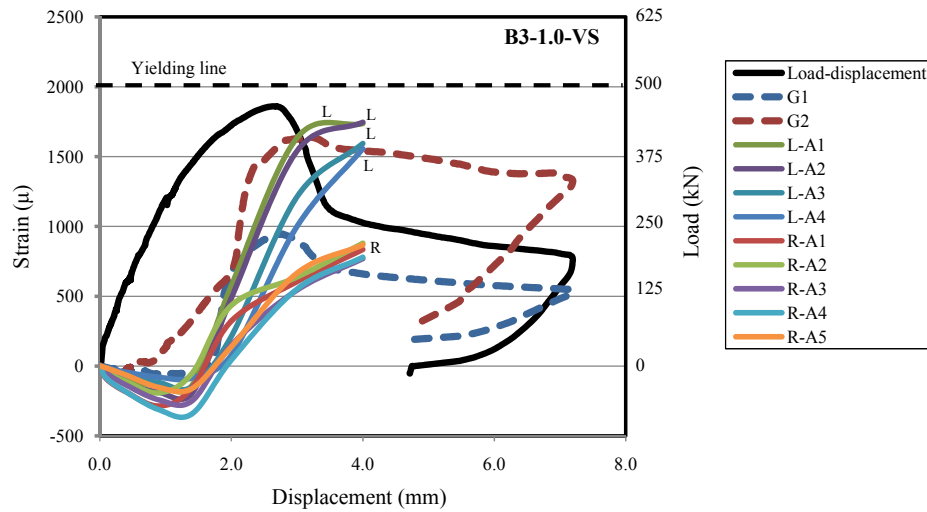
Fig. 3.29 Strain of Stirrups (B3-1.0-VS)

3.4.3 a/d=1.5 Case

The experimental and the numerical load-displacement curves for B3-1.5 and B3-1.5-VS are given in Fig. 3.30. In the experiment, the peak load and the ductility increase significantly in B3-1.5-VS case due to the effect of stirrup. In the analysis, more brittle behavior and the smaller peak load are observed in B3-1.5 case compared to the experimental one. However, the numerical peak load agrees with the shear strength equation of Niwa (1983) as demonstrated. Similarly with the experimental results, the load and ductility also increase in the analysis of B3-1.5-VS. The numerical and the experimental curves for B3-1.5 and B3-1.5-VS agree reasonably well in both pre-peak and post-peak region as seen in the figure.

44
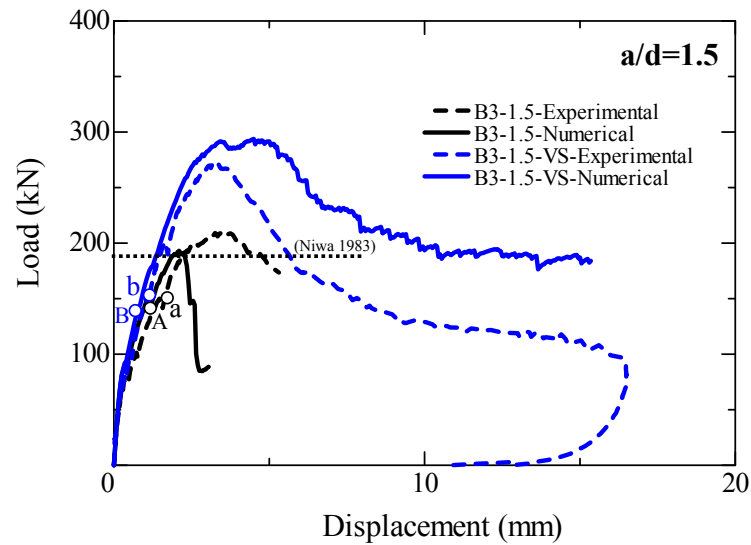
Fig. 3.30 Load Displacement Curves (a/d=1.5)

The comparison of the numerical and experimental crack pattern for B3-1.5 and B3-1.5-VS is given in Fig. 3.31. In the experiment, the damage localized on one main diagonal shear crack and a sudden diagonal shear failure occurred in B3-1.5 case. On the other hand, several shear cracks occurred at the peak and more ductile behavior is observed due to stirrups in B3-1.5-VS case. That is, the stirrup leads to several finer shear cracks rather than one main large crack and therefore more energy was absorbed and the load and ductility increased in the B3-1.5-VS case. In the analysis, only one shear crack occurred on the one shear span of the beam where more than one shear cracks occurred on the other shear span in B3-1.5. On the other hand, several shear cracks in both shear spans are formed in B3-1.5-VS specimen. Similarly with the experimental results, the beam suddenly failed in diagonal shear in the B3-1.5 case and the diagonal shear failure with softening behavior was observed in B3-1.5-VS specimen in the analysis.

45

	Experimental	Numerical

P= 150 kN (a)   P= 144 kN (A)

The peak P= 209 kN   The peak P= 193 kN

(a) B3-1.5

P= 150 kN (b)   P= 142 kN (B)

The peak P= 274 kN   The peak P= 294 kN
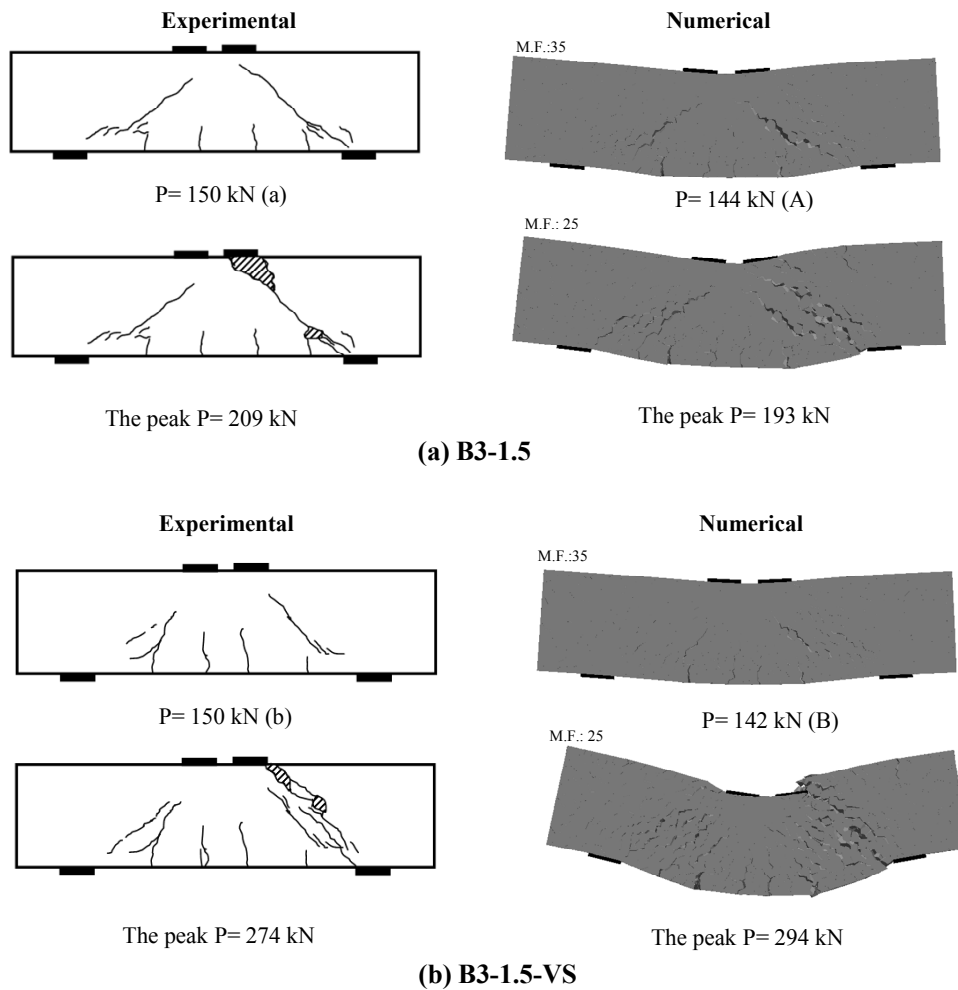
(b) B3-1.5-VS

Fig. 3.31 Crack Pattern (a/d=1.5)

Figure 3.32 shows the comparison of stirrup strains between the analysis and the experiment for B3-1.5-VS specimen. The yielding of stirrups before the peak load is observed in both the experiment and the analysis. The numerical results reasonably agree with the experimental results as seen in the figure. In the analysis, the range of strain values both on the side "L" and "R" is wide as seen in the figure. The reason is that, since the damage localize mainly on a one diagonal crack direction, larger strain values is observed near the main diagonal crack. Therefore, the effect of diagonal crack is dominant rather than the strut action.
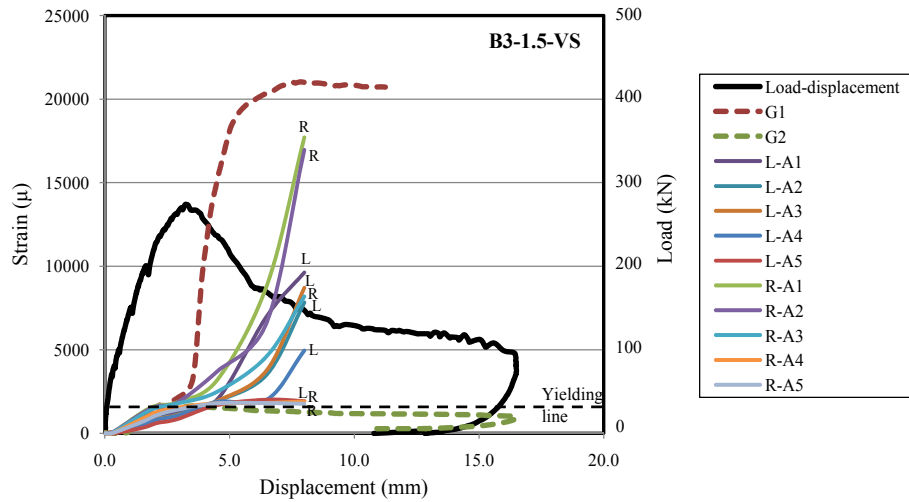
Fig. 3.32 Strain of Stirrups **(**B3-1.5-VS)

3.4.4 a/d=2.0 Case

Figure 3.33 shows the experimental and the numerical load-displacement curves for B3-2.0 and B3-2.0-VS. In the experiment, the peak load and the ductility increase significantly in B3-2.0-VS case. The numerical and the experimental results agree well in both cases.
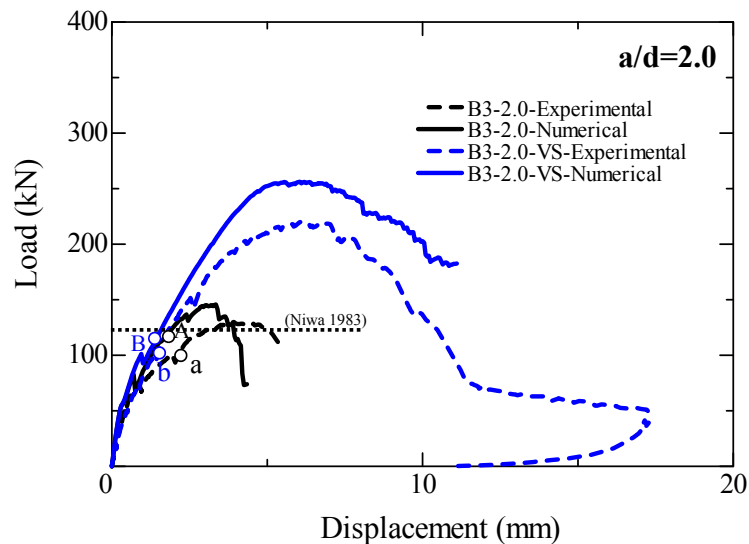
Fig. 3.33 Load Displacement Curves (a/d=2.0)

Figure 3.34 shows the comparison of the numerical and experimental crack pattern for B3-2.0 and B3-2.0-VS. In both experiment and the analysis, the damage localizes on one main diagonal shear crack that leads to a sudden diagonal shear failure in B3-2.0 case. On the other hand, several finer shear cracks occurred at the peak and more ductile behavior is observed in B3-2.0-VS case. As seen in the figure, the crack patterns between the experiment and the analysis agreed significantly well in both B3-2.0 and B3-2.0-VS cases. Moreover, failure modes of B3-2.0 and B3-2.0-VS in the analysis are the same with the experimental ones.

(a) B3-2.0
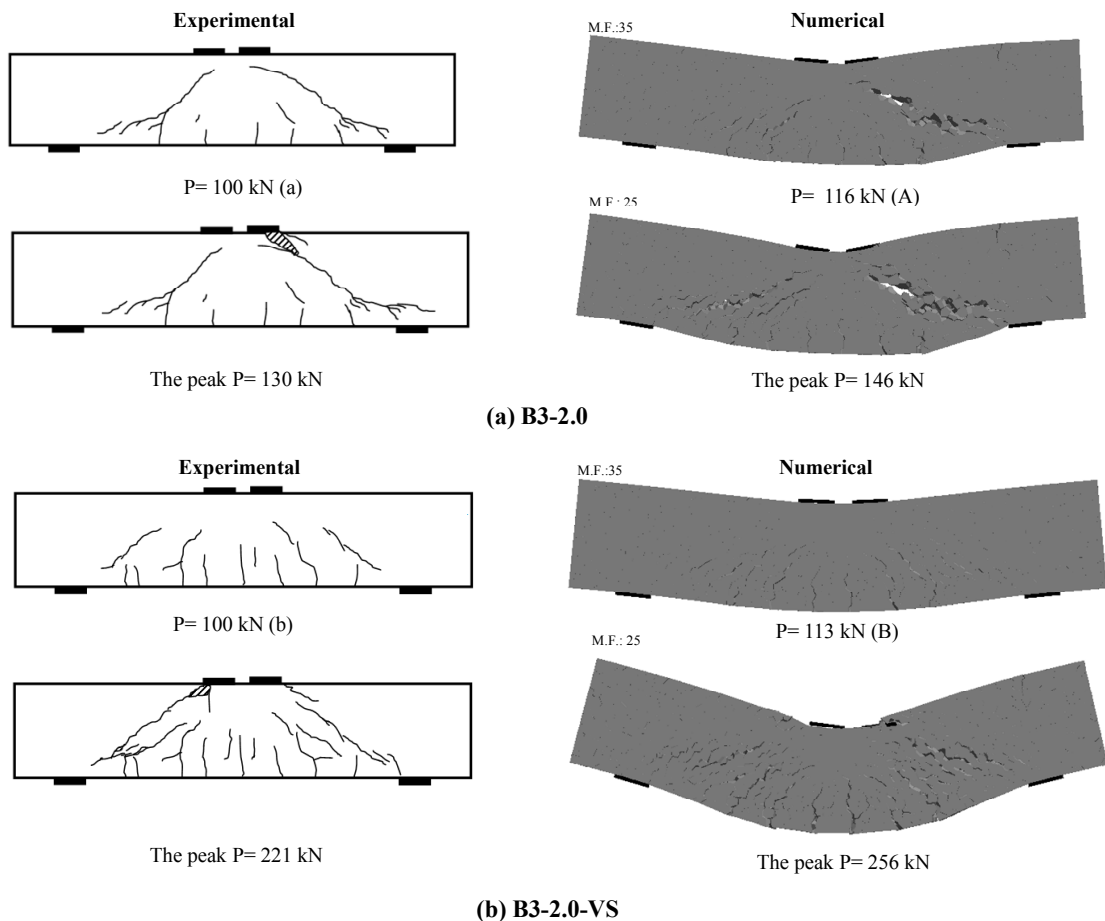
(b) B3-2.0-VS

Fig. 3.34 Crack Pattern (a/d=2.0)

Figure 3.35 shows the comparison of stirrup strains between the analysis and the experiment for B3-2.0-VS specimen. The yielding of stirrups before the peak load is observed in the experiment and the analysis. The experimental and the numerical strain values are similar as seen in Fig. 3.35. On the other hand, the range of strain values in the side "R", in which the failure occurs, is significantly wide. That confirms the effect of diagonal crack is dominant in this case similarly with the a/d=1.5 case.
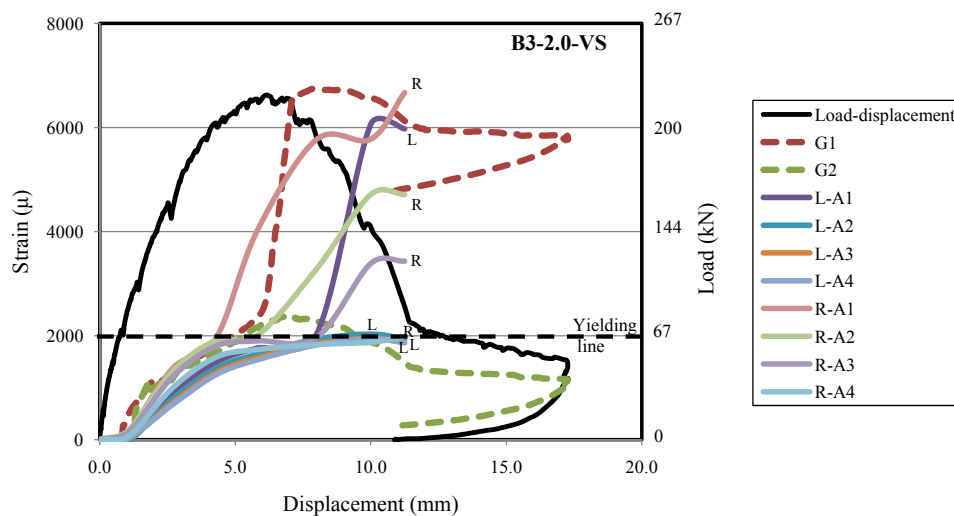
Fig. 3.35 Strain of Stirrups (B3-2.0-VS)

3.5 Summary and Conclusions

A series of beam having a/d=0.5 to 2.0 are tested and analyzed in order to demonstrate the applicability of 3-D RBSM on deep beams. The comparison of the numerical and the experimental results show that, 3-D RBSM can simulate the deep beam behavior such as load-displacement curves, crack pattern and strain of stirrups significantly well. Moreover, 3-D RBSM can also simulate the local and micro behavior as well as the macro behavior. Therefore, the simulation capability of the numerical method, which is 3-D RBSM, is confirmed.

4. Effect of Stirrup on Shear Failure Mechanism

4.1 Introduction

In this chapter, the effect of stirrups on the shear failure mechanism and load carrying capacity of deep beams is investigated in detail and the occurrence of the B and the D-regions defined by the ACI 318-05 code (2005) are clarified. In order to achieve that, a number of beams are designed and analyzed. The load carrying capacity and the shear failure mechanism are investigated in detail by evaluation of load-displacement curves, crack pattern, 3-D deformed shapes, strut behavior and stress distribution and crack widths as well as the strain of stirrups. Finally, the load carrying capacity and shear failure mechanism of deep beams with stirrup is clarified.

4.2 Analyzed Specimens

The specimen details are given in Table 4.1. The overview of the specimens for a/d=0.5, 1.0, 1.5 and 2.0 is the same with that is given in Fig. 3.1 in Chapter 3. However, the compressive strength of concrete (fc') is set to 25 MPa for all specimens. Moreover,

specimens with a/d=3.0 are also analyzed in order to demonstrate the difference between deep beams and slender beams. Three specimens are analyzed for each a/d radio including no stirrup case, with stirrup ratio of ρ_w=%0.45 and ρ_w=%0.9 cases. However, the beam with ρ_w=%0.9 in a/d=3.0 case is not included since the flexural failure was observed. The mesh size in the analysis was 20 mm for all specimens.

Table 4.1 Specimen Details

Specimen	a/d	Shear Span a (mm)	Stirrup		Compressive Strength fc' (MPa)	Peak Loads (kN)
			Spacing (mm)	ρ_w (%)		
B3-0.5	0.5	120	-	-	25.0	522
B3-0.5-VS	0.5	120	70	0.9	25.0	594
B3-0.5-VS (%0.45)	0.5	120	70	0.45	25.0	568
B3-1.0	1.0	240	-	-	25.0	331
B3-1.0-VS	1.0	240	70	0.9	25.0	376
B3-1.0-VS (%0.45)	1.0	240	70	0.45	25.0	359
B3-1.5	1.5	360	-	-	25.0	203
B3-1.5-VS	1.5	360	70	0.9	25.0	296
B3-1.5-VS (%0.45)	1.5	360	70	0.45	25.0	257
B3-2.0	2.0	480	-	-	25.0	150
B3-2.0-VS	2.0	480	70	0.9	25.0	260
B3-2.0-VS (%0.45)	2.0	480	70	0.45	25.0	232
B3-3.0	3.0	720	-	-	25.0	91
B3-3.0-VS (%0.45)	3.0	720	70	0.45	25.0	157

4.3 The Effect of Stirrup

Figure 4.1.(a) shows the comparison the shear forces (Vc) between the analysis that is the results of no stirrup cases and the equation of Niwa (1983), which was given in Chapter 3. On the other hand, Figure 4.1.(b) gives the comparison of the shear force provided by arrangement of stirrups (Vs=V-Vc). Vs is given for numerical results of with stirrup case as well as the one calculated by truss analogy for both ρ_w=%0.9 and ρ_w=%0.45 cases due to a/d ratio. To calculate the effect of stirrup by truss analogy, Equation [4.1] is considered.

$$V_s = \frac{A_w.f_{wy}}{s} \cdot \frac{d}{1.15} \qquad \text{[4.1]}$$

where;

d   : Effective depth (mm)

A_w : Total area of stirrup

f_{wy} : Yielding strength of stirrup (N/mm^2), and

s   : Spacing of stirrup

Figure 4.1.(b) may be divided into three region based on the shear failure mechanism and the effect of stirrup on the load carrying capacity. In the region of a/d less than 1.0, the value of Vs increase in smaller a/d. This region is defined as Region 1. From a/d=0.5 to 1.0, the stirrup effect (Vs) decreases and it has smallest value at a/d=1.0. Then, Vs increases again up to a/d=2.0. The effect of stirrup becomes significant for a/d=1.5 and 2.0. Therefore, the region from a/d=1.0 to 2.0 is defined as Region 2. After a/d=2.0, which is defined as Region 3, Vs is almost constant and it does not depend on a/d that agree with the results obtained from truss analogy. The effect of stirrup on the shear failure mechanism and load carrying capacity for each region is discussed in detail in the following.

(a) Concrete Contribution   (b) Stirrup Contribution
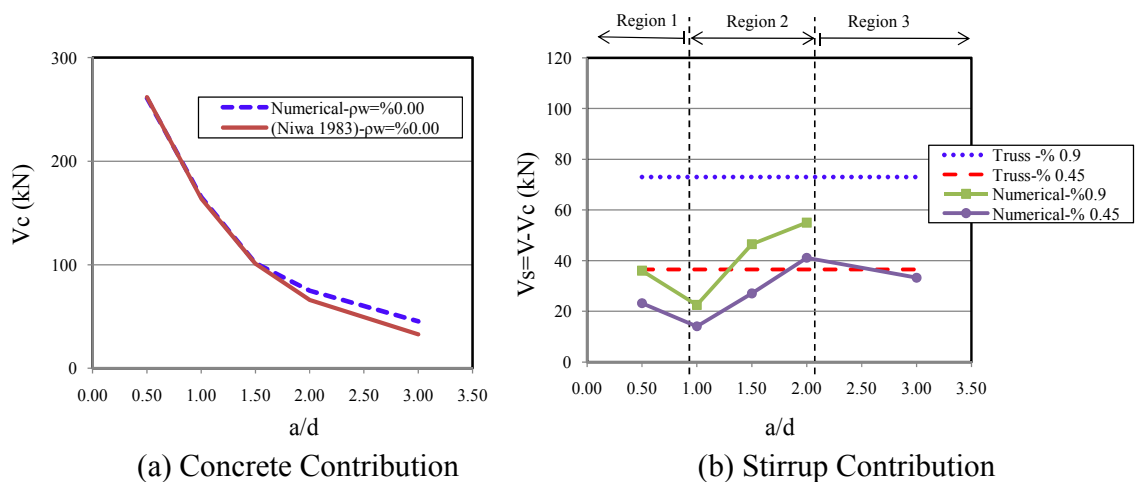
Fig. 4.1 Comparison of Shear Force

4.3.1 Region 1

4.3.1.1 a/d=0.5 case

The load displacement curves of B3-0.5, B3-0.5-VS and B3-0.5-VS (%0.45) are given in Fig. 4.2. The load and ductility increase in the beams with stirrup, however the increase in load is not sensitive to stirrup ratio as seen in the figure. Moreover, the crack pattern is similar in both B3-0.5 and B3-0.5-VS cases as discussed in Chapter 3 that is an arrangement of the stirrup does not affect the crack pattern.
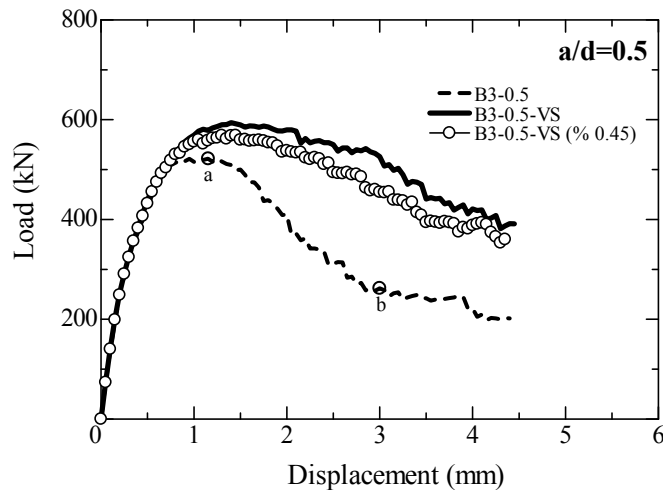
Fig. 4.2 Load-Displacement Curves (a/d=0.5)

Figure 4.3.(a) and (b) shows the principal stress distribution on the middle longitudinal beam section and on the cross section at the mid-shear span at the peak loads for B3-0.5 and B3-0.5-VS respectively. The maximum stress range is set to 32.5 MPa (1.3fc'). The distribution is similar for B3-0.5 and B3-0.5-VS. High stress concentration occurs along the strut in both cases as seen in the figure. Therefore, the load is mainly transferred from bearing plates to support based on the strut action by an effective strut.

53

In order to investigate the effect of stirrup, the stress difference between B3-0.5-VS and B3-0.5 is given in Figure 4.3.(c). The figure is obtained by subtracting the principal stress value of B3-0.5-VS from B3-0.5 at the peak load. That is, the figure demonstrates the increase of the principal stress caused by only stirrup. As seen in the Fig. 4.3.(c), the increase of stress is observed only near the sides of the bearing and support plates, where the localization behavior occurs in deep beams. The behavior is confirmed by the comparison of cross-sectional stress distribution between B3-0.5 and B3-0.5-VS (See Fig. 4.3). The stress increase may contribute the increase of maximum load.

(a) B3-0.5

(b) B3-0.5-VS

(c) Difference
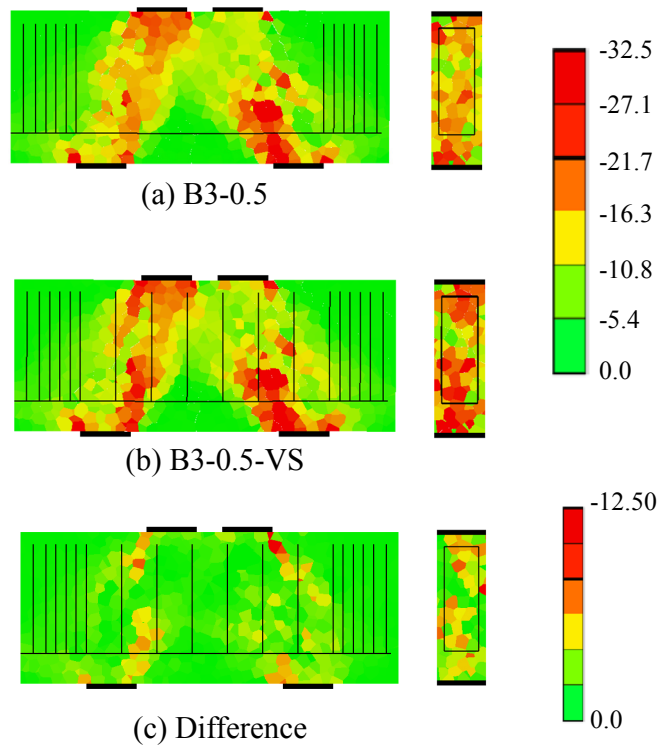
Fig. 4.3 Stress Distribution (a/d=0.5)
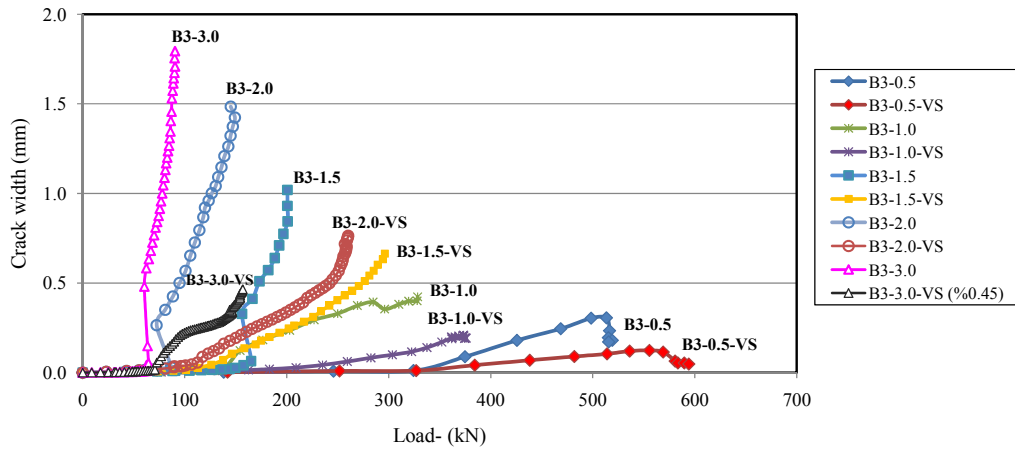
Fig. 4.4 Comparison of Crack Width

Figure 4.4 shows the comparison of the shear crack widths between B3-0.5 and B3-0.5-VS. As seen in the figure, the crack widths are limited and the growth rate is relatively small for both cases. Moreover, stirrups do not yield in a/d=0.5 case as discussed in Chapter 3. That is, the effect of stirrup on the crack width is not significant and therefore the stirrup does not contribute to the shear strength mechanism.
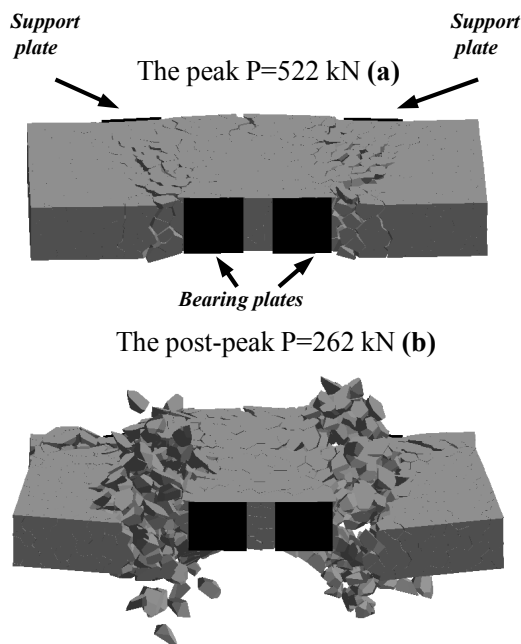
Fig. 4.5 3-D Deformed Shapes (a/d=0.5)

Figure 4.5 shows 3-D deformed shapes for B3-0.5 specimen at the peak (a) and a post-peak load (b), which are also labeled on Fig. 4.2. In order to investigate the lateral deformation and spalling of concrete on the beam surface clearly, the figures are rotated along the longitudinal beam axis. The location of support and bearing plates after rotation are labeled on the figure. 3-D deformed shapes in this chapter are magnified by a factor of 25. At the peak load (a), the concrete spalling is observed within the strut and a large amount of concrete spalling occurs in the post-peak region (b). It is understood that; in a/d=0.5 case, the lateral deformation is dominant rather than the vertical deformation. The stirrup resists against the lateral deformation discussed above and provides the confinement within the strut. Therefore, the increase of load and ductility in stirrup cases are caused by the confinement effect due to the stirrup rather than the stirrup effect on the vertical direction. The beam effect represented by the B-region does not occur. Therefore, the entire beam is considered as the D-region, in which the confinement effect of stirrup is dominant.

4.3.2 Region 3

4.3.2.1 a/d=3.0 case

Figure 4.6 shows the load displacement curves for B3-3.0 and B3-3.0-VS (%0.45) specimens. The load and ductility significantly increase in B3-3.0-VS (%0.45) case as expected. Figure 4.7 shows the comparison of the crack pattern at the peak load. The figures are magnified by a factor of 20. As seen the Fig. 4.7.(a), the damage localized on one main diagonal crack that lead a diagonal shear failure in B3-3.0 case. On the other hand, many shear cracks form in B3-3.0-VS (%0.45) specimen (see Fig. 4.7.(b)). The effect of stirrup on the crack width is also confirmed by Fig. 4.4. That is the crack width significantly decreases due to stirrup arrangement.
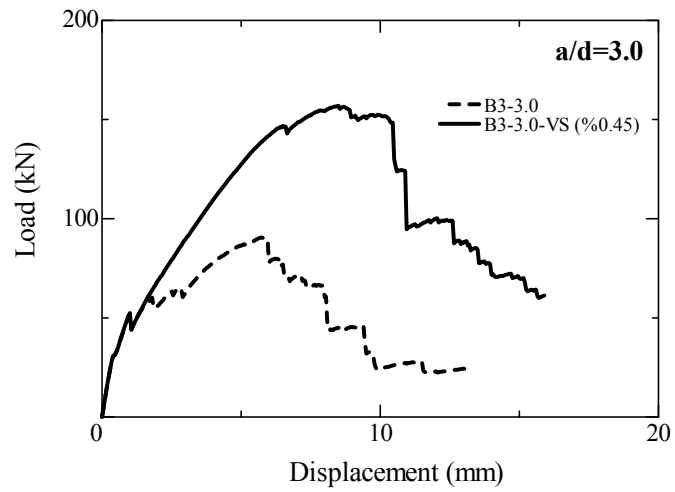
Fig. 4.6 Load-Displacement Curves (a/d=3.0)
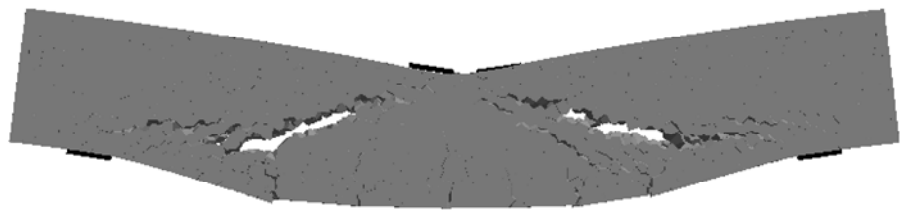
(a) B3-3.0
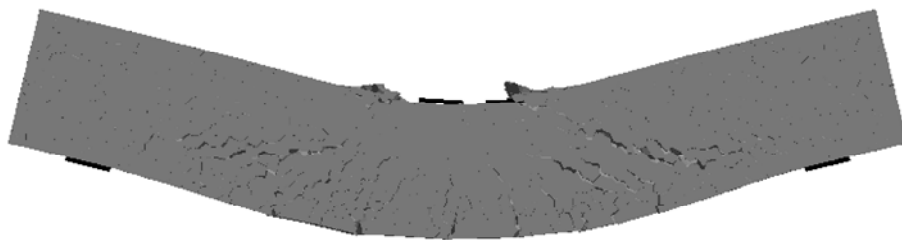
(b) B3-3.0-VS-(%0.45)

Fig. 4.7 Crack Pattern at the Peak Load

Figure 4.8.(a) and (b) shows the principal stress distribution in compression along the middle longitudinal section for B3-3.0 and B3-3.0-VS (%0.45) specimens respectively. In B3-3.0 case, a stress flow is observed from the bearing plates to supports. On the other hand,

in B3-3.0-VS (%0.45) case, stress is distributed in a wide area and the clear difference of stress distribution is observed due to the effect of stirrup.

The principal stress difference between B3-3.0-VS and B3-3.0 is given in Figure 4.8.(c). The beam effect caused by stirrup in slender beams can be investigated clearly from the figure. It can be observed that the stress flow is based on the truss analogy. That is, the compressive top chord and diagonal struts appears which is superposed with stress distribution of no stirrup case. Therefore, the beam action (B-region) is observed from a distance from the bearing and support plates. Therefore, it is confirmed that, the B and the D-regions are formed separately in slender beams as defined in ACI-318-05.

(a) B3-3.0

(b) B3-3.0-VS-(%0.45)

Compression chord

Diagonals   (c) Difference
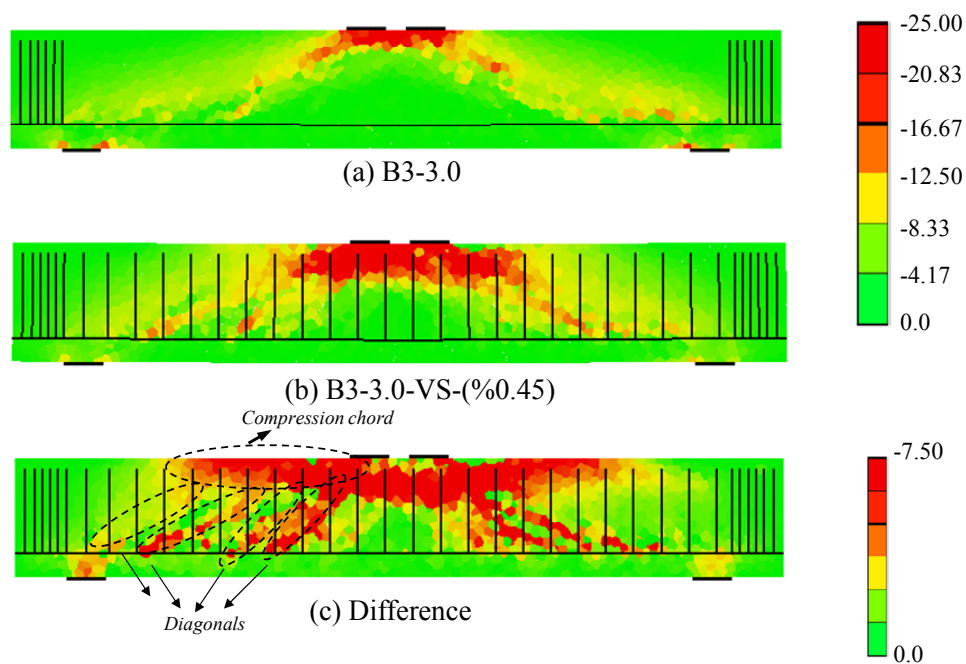
Fig. 4.8 Stress Distribution (a/d=3.0)

These results confirm the design concept based on the truss analogy for slender beams given in JSCE 2007 and ACI-318-05, where the shear strength of the beam can be calculated

as V=Vc+Vs. That is, Vc remains after occurrence of diagonal crack and Vs is superposed. Moreover, the numerical results agreed well with the truss analogy in Region 3 as shown in Fig. 4.1.(b).

4.3.3 Region 2

The load displacement curves of a/d=1.0, 1.5 and 2.0 cases are given in Fig. 4.9, 4.10 and 4.11 respectively. In all cases, the increase in load as well as ductility is observed in the beams with stirrup. The increase rate increases with larger a/d ratio that was already confirmed in Fig. 4.1.(b). Moreover, the load displacement curves in the post-peak are more sensitive to stirrup ratio for larger a/d cases.
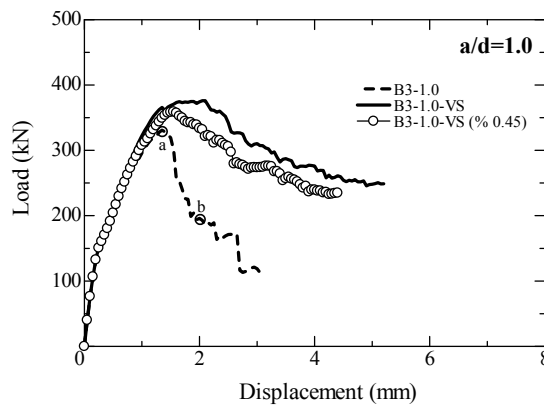
Fig. 4.9 Load-Displacement Curves (a/d=1.0)
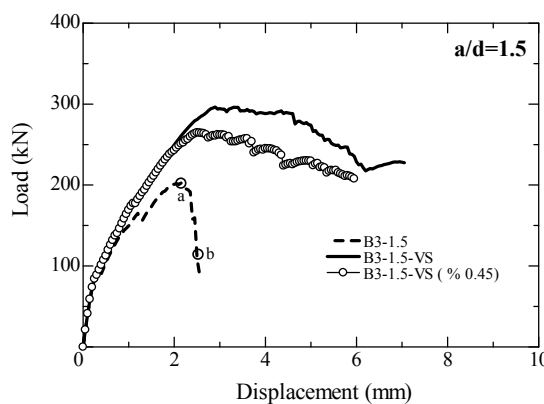
Fig. 4.10 Load-Displacement Curves (a/d=1.5)
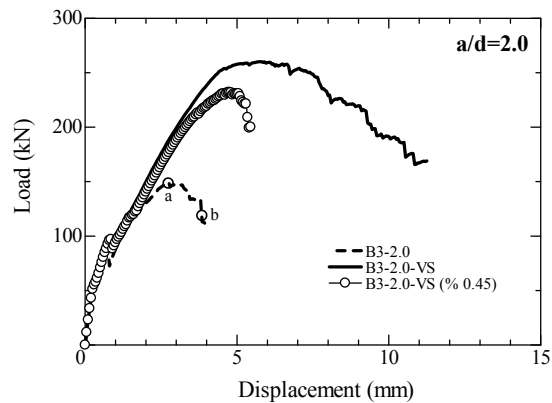
Fig. 4.11 Load-Displacement Curves (a/d=2.0)

Strain of stirrups for a/d=1.0, 1.5 and 2.0 was already discussed in Chapter 3. A similar behavior is also observed in this section. In a/d=1.0 case, only one of the stirrups within the shear span reaches to yielding strain near the peak load. On the other hand, two stirrups in a/d=1.5 case and three stirrups in a/d=2.0 yield before the peak. It confirms that, the stirrup effect increases for larger a/d ratios.

The comparison of the crack pattern for a/d=1.0, 1.5 and 2.0 was also given in Chapter 3. In a/d=1.0 case, the number of cracks slightly increases in B3-1.0-VS case due to the stirrup. For a/d=1.5 and 2.0 cases, the number of the cracks remarkably increases in with stirrup cases compared to no stirrup ones, which provides more energy absorption that leads to increase in load and ductility.

The comparison of the shear crack widths between with and without stirrup cases for a/d=1.0, 1.5 and 2.0 cases are given in Fig. 4.4. In a/d=1.0 case, the crack widths are small and the growth rate is also limited for both B3-1.0 and B3-1.0-VS cases. That is, the effect of stirrup on the crack development is limited. For a/d=1.5 case, the crack width and the growth rate are high for B3-1.5 specimen. On the other hand, the crack widths and growth rate

decrease significantly in B3-1.5-VS case that shows the effectiveness of stirrups on preventing the crack development. Similarly with B3-1.5 specimen, the crack width and the growth rate are significantly high for B3-2.0 specimen while the crack widths and growth rate decrease significantly in B3-2.0-VS case. That is, stirrup is effective for shear resistance mechanism.

3-D deformed shapes of B3-1.0, B3-1.5 and B3-2.0 specimens for the peak and a post-peak load are given in Fig. 4.12, 4.13 and 4.14 respectively. In a/d=1.0 case, concrete spalling is observed at the peak load (a) and it increases in the post peak (b). However, the amount of the spalling is smaller compared to the B3-0.5 case. On the other hand, the lateral deformation, which refers concrete spalling on the beam surface along beam width direction, is observed only near the bearing plate in B3-1.5 specimen and it is not dominant on the behavior. In B3-2.0 specimen, the lateral deformation is not notable as seen in the figure. Therefore, it may be noted that, stirrup is effective for shear resistance mechanism in Region 2 and the confinement effect and lateral deformation remarkably decrease with increase of a/d.

Support plate

The peak P= 331 kN **(a)**

Support plate

Bearing plates

The post-peak P= 196 kN **(b)**
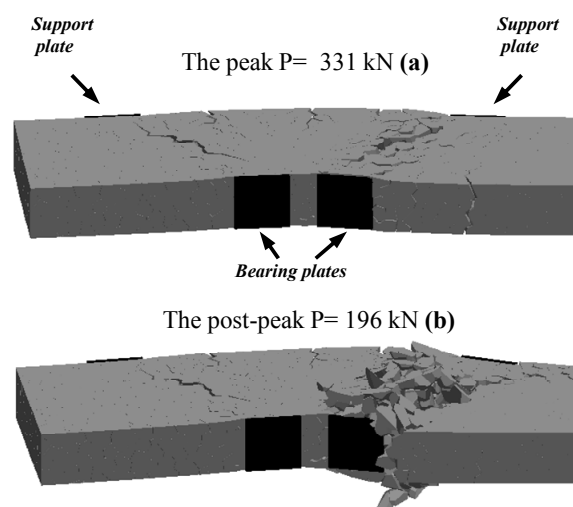
Fig. 4.12 3-D Deformed Shape (a/d=1.0)

The peak P= 203 kN **(a)**

Bearing plates

The post-peak P= 110 kN **(b)**

Fig. 4.13 3-D Deformed Shape (a/d=1.5)

The peak P= 149 kN **(a)**

Bearing plates

The post-peak P= 113 kN **(b)**
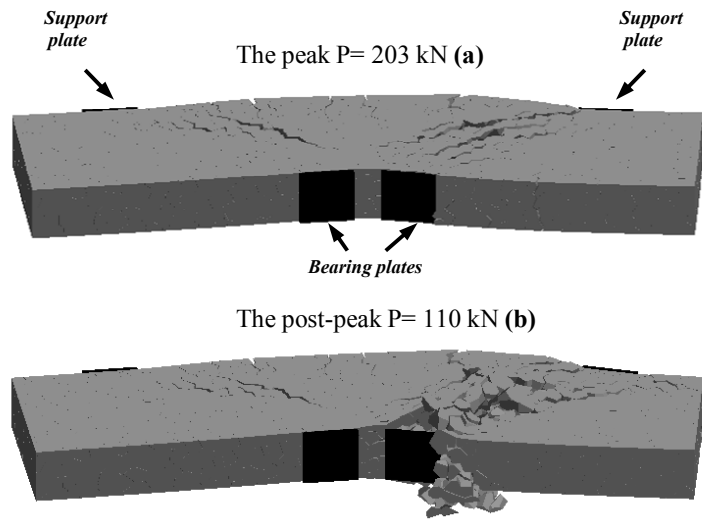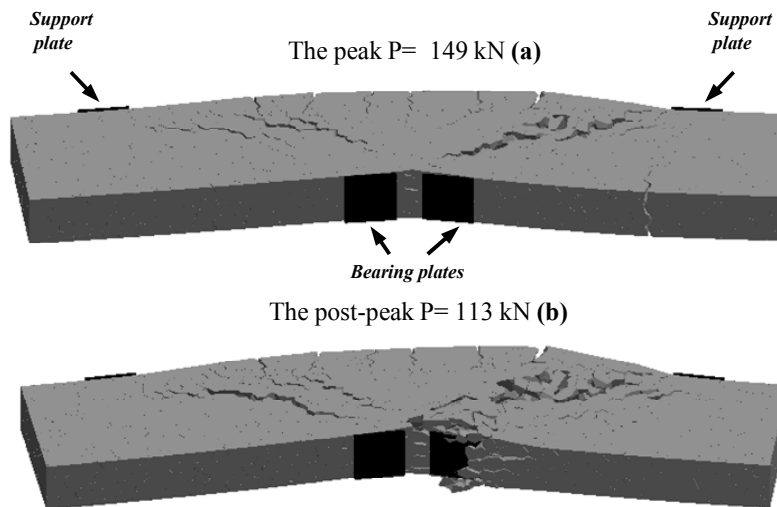
Fig. 4.14 3-D Deformed Shape (a/d=2.0)

The principal stress distribution for a/d=1.0, 1.5 and 2.0 cases are shown in Fig. 4.15, 4.16 and 4.17 respectively. Figure 4.15.(a) and (b) shows the stress distribution for B3-1.0 and B3-1.0-VS specimens. The load is transferred from bearing plates to support by a

continuous strut. In B3-1.0-VS case, the strut width slightly increases due to the stirrup.

(a) B3-1.0

(b) B3-1.0-VS

(c) Difference
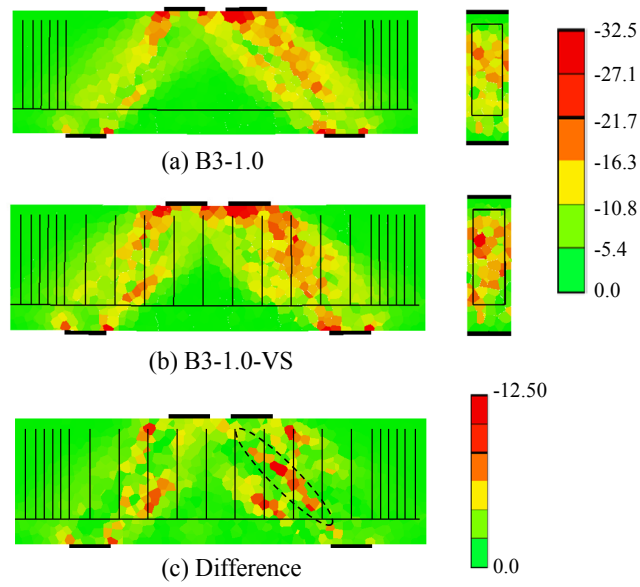
Fig. 4.15 Stress Distribution (a/d=1.0)

(a) B3-1.5

(b) B3-1.5-VS

(c) Difference
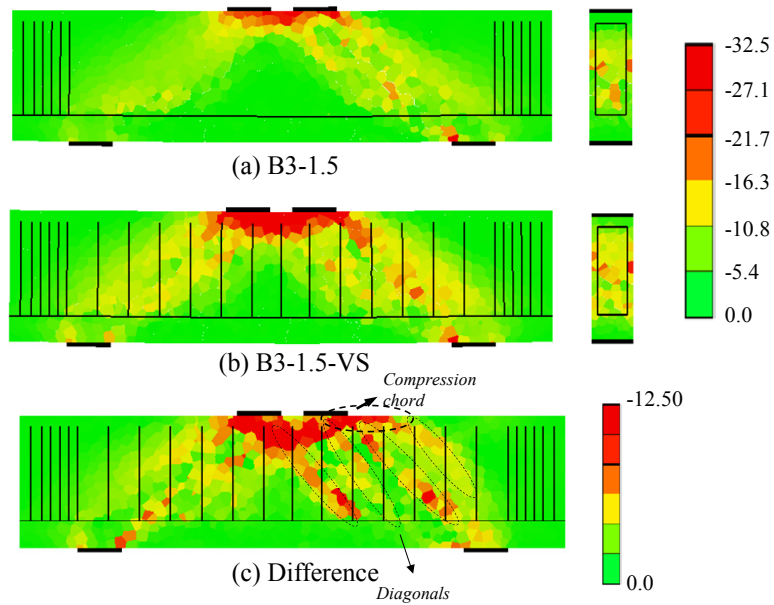
Fig. 4.16 Stress Distribution (a/d=1.5)
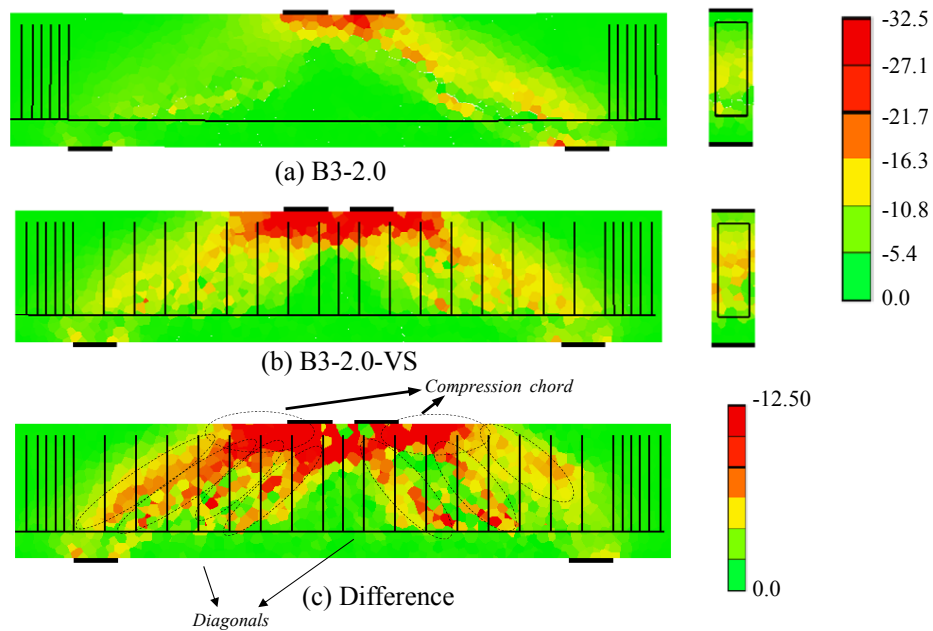
Fig. 4.17 Stress Distribution (a/d=2.0)

The stress distribution for B3-1.5 and B3-1.5-VS specimens is given in Fig. 4.16.(a) and (b) respectively. The stress concentration between the bearing plates occurs due to bending effects. A weaker strut behavior is observed and the stress values within the strut are smaller for both B3-1.5 and B3-1.5-VS compared to a/d=0.5 and 1.0 cases. Moreover, the strut continuity is weak near the support as seen in the figures. On the other hand, the strut width increases remarkably in B3-1.5-VS case due to the stirrup arrangement.

Figure 4.17.(a) and (b) shows the principal stress distribution for B3-2.0 and B3-2.0-VS specimens. The stress concentration between bearing plates also occurs due to bending effects. Similarly with a/d=1.5 case, the strut behavior is weaker compared to a/d=0.5 and 1.0 cases. The strut continuity from bearing plates to support is weak especially near the support plates in both B3-2.0 and B3-2.0-VS cases. On the other hand, the strut width increases significantly in B3-2.0-VS case.

The comparison of cross-sectional stress at the mid-shear span for a/d=1.0, 1.5 and 2.0 cases are also shown in Fig. 4.15, 4.16 and 4.17 respectively. The stress of the cross-section values slightly increase in B3-1.0-VS, however the effect is smaller compared to a/d=0.5 case. On the other hand, there is no high stress state and the confinement effect is not observed in B3-1.5-VS and B3-2.0-VS cases since the lateral deformation is not dominant. Therefore, these results also confirmed that stirrup is does not work for confinement in Region 2.

The principal stress difference for a/d=1.0, 1.5 and 2.0 are given in Fig. 4.15.(c), 4.16.(c) and 4.17.(c) respectively in order to investigate the occurrence of the B and D-region and clarify the load carrying mechanism. Figure 4.15.(c) shows the difference for a/d=1.0 case. On the main strut direction, a sub-strut is formed that contributes to strut action, which is also confirmed by stress increase near the mid-height cross-section (See Fig. 4.15.(b)). However, a compression chord on the top of the beam does not occur. That is, the beam effect and a similarity with truss analogy do not appear clearly. Therefore, no B-region occurs and the entire beam should be be considered as a single D-region in a/d=1.0 case.

The principal stress difference for a/d=1.5 and 2.0 cases are given in Fig. 4.16.(c) and 4.17.(c). The difference for a/d=1.5 and 2.0 cases are similar, which is also similar with a/d=3.0 case. As seen in the figures, sub-struts are formed from top of the beam to longitudinal reinforcement level continuously and a compression chord occurs on the top of the shear span that is similar with the truss analogy. Therefore, the stirrup also contributes to load transfer by occurrence of the beam effect. That is the beam action (B-region) is also effective on the shear failure mechanism as well as the strut action. Moreover, truss analogy is more dominant on the behavior rather than the strut action. As a result, the B and the D-regions are superposed in a/d=1.5 and 2.0 cases. This result is different from ACI 318-0.5

Code, in which the entire member considered as a single D-region for deep beams.

4.4 Summary and Conclusions

In order to investigate the shear failure mechanism and load carrying capacity of deep beams, several beams with a/d=0.5 to 3.0 are designed and analyzed. Then, the numerical results are investigated in detail by evaluation of load-displacement curves, crack pattern, 3-D deformed shapes, strut behavior and stress distribution and crack widths as well as the strain of stirrups.

Based on the numerical results, the beams are classified into three regions considering the effect of stirrup on the shear failure mechanism and load carrying capacity. In region 1, the beams with a/d=0.5 is included, in which 3-D effects and lateral deformation rather than the vertical one are dominant on the shear strength. In this case, there is no effect of stirrups along the vertical direction. The load increases due to confinement effect provided by stirrups. In this case, the strut action is dominant on the behavior and the entire member is considered as a single D-region as defined in ACI 318-0.5 code.

In region 3, the slender beams with a/d=3.0 are included. By comparing the stress distribution between with and without stirrup cases, the occurrence of compression chords and compression diagonals due to stirrup is demonstrated which agrees with truss analogy. It is clarified that, the B and D-regions are formed separately as defined in ACI 318-0.5 for slender beams. It is confirmed that Vs can be superposed to Vc to obtain the shear strength.

In region 2, the beams with a/d=1.0, 1.5 and 2.0 are included. In this region, stirrup is effective along vertical direction. In a/d=1.0 case, the lateral deformation is also observed, however it is smaller compared to a/d=0.5 case. There is limited effect of stirrup in this case

and the stirrup contributes to strut action that is dominant on the behavior. Therefore, the entire member should also be considered as a single D region for a/d=1.0 case. On the other hand, the effect of stirrup is significant in a/d=1.5 and 2.0 cases. The load as well as the ductility increase significantly. The occurrence of compression chords and compression diagonals due to stirrup is also obsorbed in this case. That is, the mechanism of beams with stirrup shows similar behavior with the truss analogy. Both strut action and truss effect provided by stirrup contributes to load carrying mechanism. Moreover, truss analogy is more dominant on the behavior rather than the strut action. As a result, the B and the D-regions are superposed in a/d=1.5 and 2.0 cases. This result is different from ACI 318-0.5 Code, in which the entire member considered as a single D-region for deep beams.

For future study, these results should be extended and generalized for deep beams by evaluation of more wide range of specimens with various parameters such as size and stirrup ratio (%).

5. *Three-Dimensional Effects in Short Deep Beams*

5.1 Introduction

In chapter 4, it was clarified that three-dimensional effects and lateral deformation is important for deep beams with smaller a/d ratios. In this chapter, in order to clarify 3-D effects in short deep beams, 3-D behavior as well as the size and shape effect resulting from beam width is investigated. In order to achieve that, short deep beams with a/d=0.5 and having different size and widths are tested, and the failure mechanism is discussed in order to determine the effect of size and shape resulting from the beam width on behavior. The tested beams are simulated by 3-D RBSM and the results, such as the load-displacement curve, deformation, and failure depths on the strut, are compared. Moreover, the analyses are expanded to include various width cases to clarify the effect of beam width.

5.2 Experimental Program

Two series of specimens as described in Table 5.1 were tested in order to investigate the 3-D effects in short deep beams with a/d=0.5 and without stirrups in shear spans. Figure 5.1

shows the dimensions of the tested specimens. BS2bw and BS4bw series have the height of 200 mm and 400 mm respectively. The beam length and height of the beams in each series are the same, while the beam widths are different as indicated. That is, BS2bw series has three specimens with beam widths of 100, 200 and 300 mm while the other dimensions for each specimen are the same. In this series, the effect of the beam width on behavior is investigated. BS4bw series has two specimens with beam widths of 100 and 200 mm. In this case, shape effect resulting from the beam width is also clarified. Moreover, BS2bw and BS4bw series are compared in order to investigate the size effect.

The longitudinal reinforcement ratio was kept constant in each series. Relatively large plate widths were used to prevent bearing failure on the loading point. Mixture proportion of concrete is given in Table 5.2. Specimens were cured with water after remolding.

Table 5.1 Properties of Test Specimens

Specimen	Beam Length L (mm)	Overall Height h (mm)	Effective Depth d (mm)	Beam Width b (mm)	Shear Span a (mm)	a/d	Plate Width (mm)	Longitudinal Reinforcement As (mm^2)	ρ_s (%)	Compressive Strength fc' (MPa)
BS2bw100	500	200	160	100	80	0.5	80	396(2D10+2D13)	2.48	20.1
BS2bw200	500	200	160	200	80	0.5	80	792(4D10+4D13)	2.48	19.5
BS2bw300	500	200	160	300	80	0.5	80	1188(6D10+6D13)	2.48	19.5
BS4bw100	1000	400	320	100	160	0.5	160	826 (2D13+2D19)	2.58	20.1
BS4bw200	1000	400	320	200	160	0.5	160	1653(4D13+4D19)	2.58	19.5

Table 5.2 Concrete Mixture Proportion

G$_{max}$	Water-Cement Ratio	Mass Per Unit Volume (kg/m^3)			
(mm)	W/C (%)	Water W	Cement C	Sand S	Gravel G
15	0.56	166	294	779	990

* An admixture was used having an amount of 0.4% of Cement

Fig. 5.1 Overview of Specimens

Figure 5.2 shows the experimental setup for four-point loading that was applied to the test specimens. The load was distributed on the loading points using a steel beam. Steel rollers were used between the loading plates and the steel beam. 4 LVDT for support deflections and 1 LVDT for mid-span deflection were used to obtain the beam displacements. The relative mid-span deflection was taken into consideration by subtracting the support displacements.
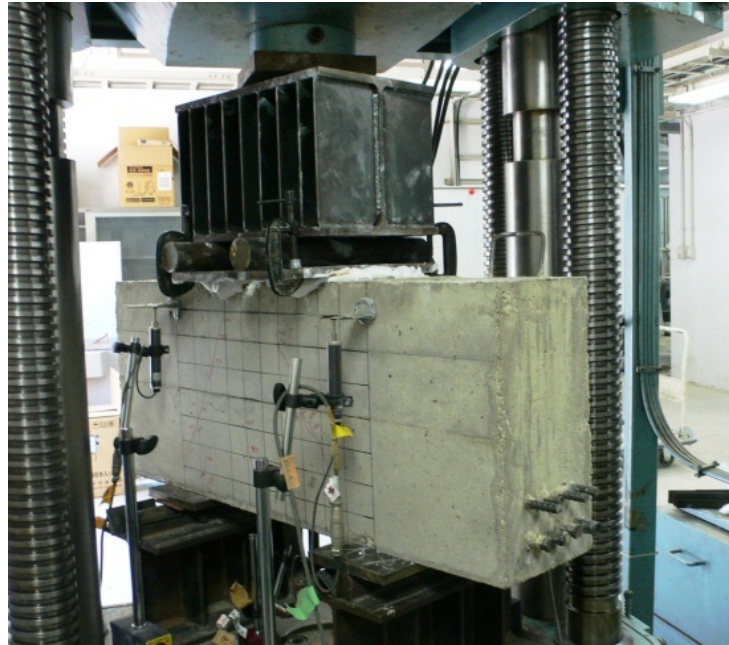
Fig. 5.2 Experimental Setup

5.3 Experimental Results

5.3.1 BS2bw Series

Figure 5.3 shows the load-displacement curves of the BS2bw100, BS2bw200 and BS2bw300 specimens. The peak loads are 469 kN, 971 kN and 1457 kN respectively. Failure patterns of the specimens are given in Fig. 5.4. In BS2bw100 case, the beam failed in shear compression with spalling of concrete along the entire strut. The amount of spalling increases in further post-peak loads. In this case, the spalling localized only on the one side of the beem as seen in the figure. Similarly with the BS2bw100 specimen, the beam also failed in shear compression with spalling of concrete along the entire strut in BS2bw200 and BS2bw300 cases. However, the damage and spalling are distributed to two sides of the beams. Moreover, amount of the spalling relative to the beam widths reduces by increase of the beam widths.
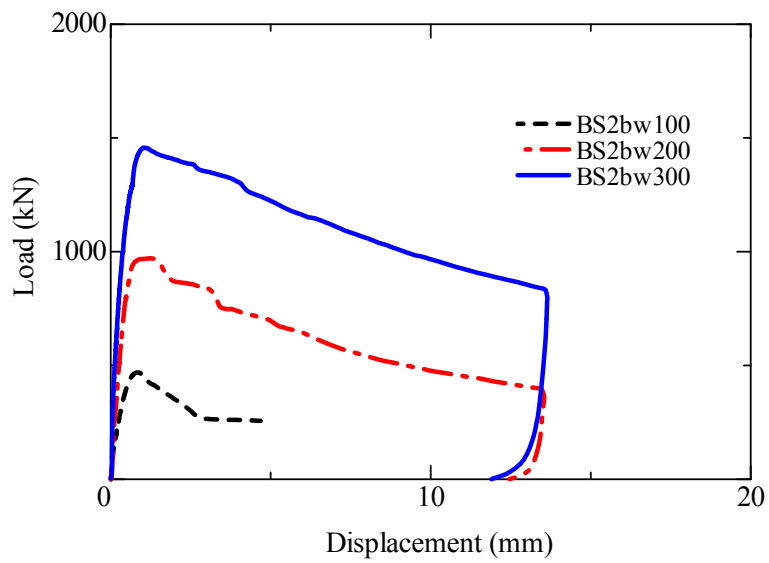
Fig. 5.3 Load-Displacement Curves (BS2bw)

(a) BS2bw100

(b) BS2bw200

(c) BS2bw300
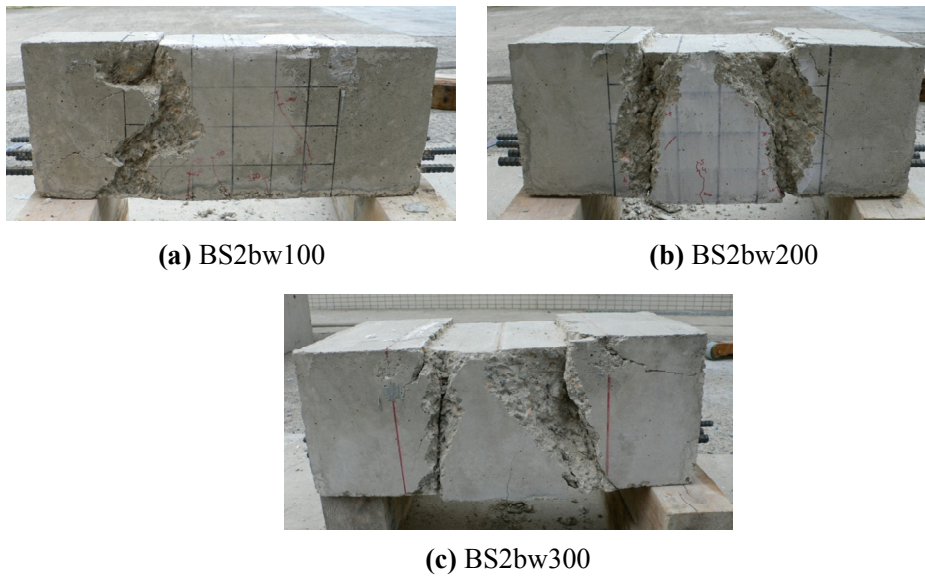
Fig. 5.4 Failure of Specimens

5.3.2 BS4bw Series

The load-displacement curve of the BS4bw100 specimen is shown by the dashed line in Fig. 5.5. The peak load is 751 kN. Sudden shear failure occurred and no post-peak region was measured, as shown in the figure.
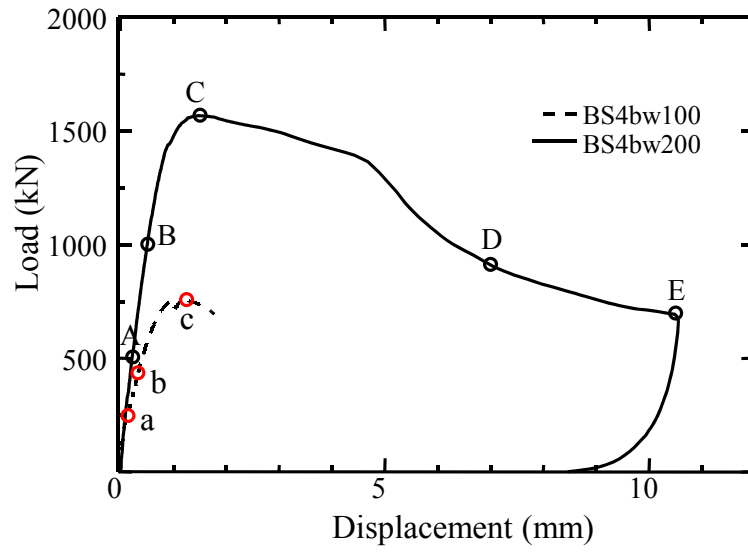
Fig. 5.5 Load-Displacement Curves (BS4bw)
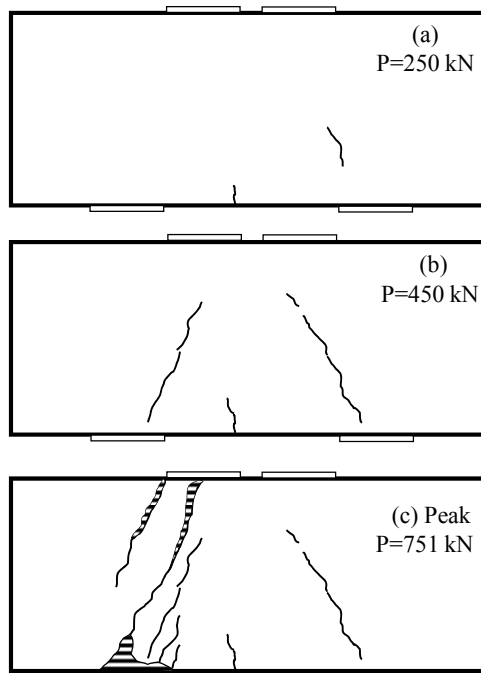
Fig. 5.6 BS4bw100 Crack Patterns

Figure 5.6 shows the crack pattern of the beam up until peak load. The first shear crack

was formed in the lower part of the strut together with a mid-span bending crack at P=250

kN (a). At P=450 kN, shear cracking was propagated and another shear crack occurred on the other side (b). At peak load (c), two shear cracks, one from the outer side of the loading plate, and another running from the support to the loading point, developed and the beam suddenly failed in shear-compression failure with spalling of the concrete, indicated by the shaded areas. Failure pattern of the specimen is given in Fig. 5.7.

Fig. 5.7 Failure of BS4bw100

The load-displacement curve of the BS4bw200 specimen is shown by the solid line in Fig. 5.5. The peak load is 1568 kN and ductile softening behavior can be observed in the post-peak region.

Figure 5.8 shows the crack pattern of the beam. The first shear crack developed from the support to the upper part of the strut at P=500 kN (A). Then, another shear crack occurred on the other side together with mid-span bending cracks at P=1000 kN (B). At peak load, new shear cracks were developed that connected to the loading plates that led to shear compression failure with spalling of the concrete (C). In the post-peak region, the spalling of concrete and lateral deformation increased (D) and developed along the entire strut (E) as shown in the figures. Failure pattern of the specimen is given in Fig. 5.9.
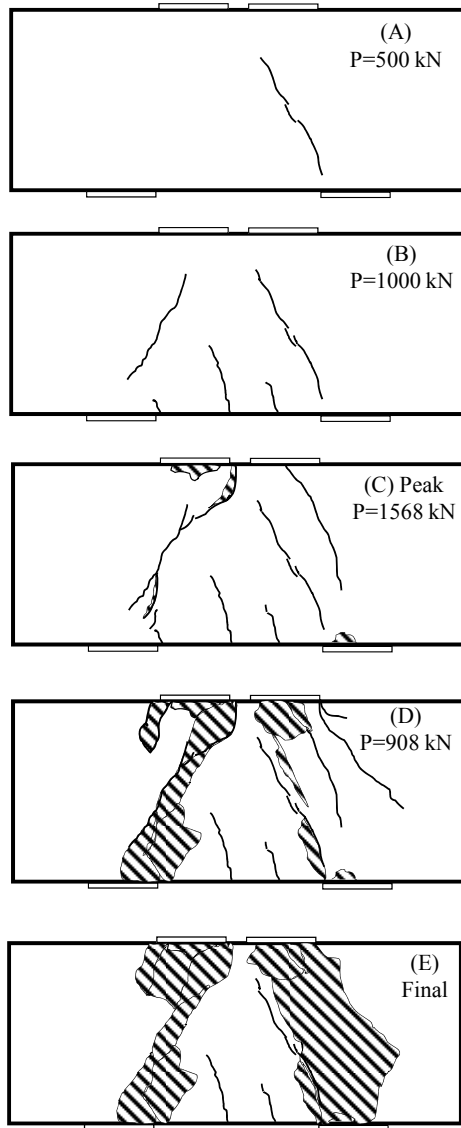
Fig. 5.8 BS4bw200 Crack Patterns

Fig. 5.9 Failure of BS4bw200

5.4 Numerical Results

5.4.1 Comparison of Numerical and Experimental Results

The details of tested specimens and the experimental results are introduced in Section 5.3. The tested BS4bw100 and BS4bw200 beams are simulated by 3-D RBSM and the load-displacement curves and crack patterns are compared. The mesh size in the numerical analysis was 22 mm for each case.
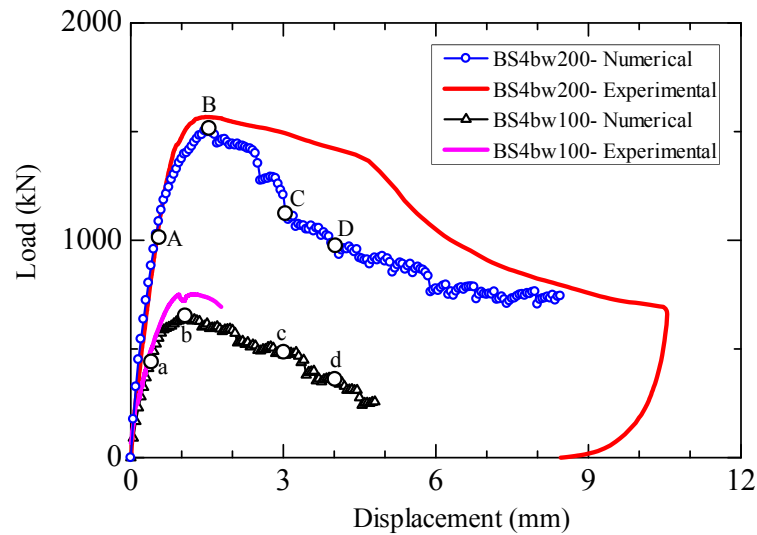
Fig. 5.10 Load-Displacement Curves

The load-displacement curves of the experimental results and analysis for BS4bw100 are compared as shown in Fig. 5.10. The numerical peak load is 638 kN, which is lower than the experimental result, which is 751 kN. The comparison of crack patterns at the numerical pre-peak load P=452 kN (labeled 'a' in Fig. 5.10) and at the peak load (b) are shown in Fig. 5.11. The numerical deformed shapes are magnified by a factor of 60. Reasonable agreement between analysis and the experimental results is observed, as seen in the figure. However, the damage mainly localizes only one side of the beam in the experiment. On the other hand, the

damage is distributed to two side of the beam in the analysis since the specimen is homogeneous. Therefore, more energy is absorbed in the analysis that is the reason of why a brittle sudden failure is not observed in the analysis as distinct from the experiment (See Fig 5.10).

| P=450 kN | P=452 kN | (a) |

| P=751 kN | P=638 kN | (b) |

Experimental   Numerical
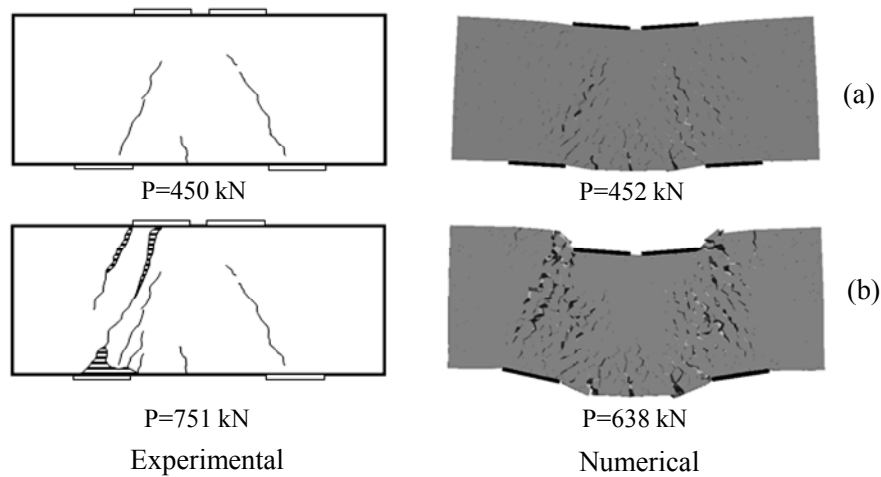
Fig. 5.11 BS4bw100 Crack Patterns

The comparison of the load-displacement curves for BS4bw200 is also given in Fig. 5.10. The numerical peak load is 1513 kN, which is slightly lower than the experimental result, which is 1568 kN. The curves show reasonably good agreement in both the pre-peak and post-peak regions. The comparison of crack patterns at the numerical pre-peak load P=1028 kN (A) and at the peak load (B) are shown in Fig. 5.12. The numerical deformed shapes are magnified by a factor of 60. As seen in the figure, reasonable agreement between analysis and the experimental results is observed.

P=1000 kN   P=1028 kN   (A)

P=1568 kN   P=1513 kN   (B)

Experimental   Numerical
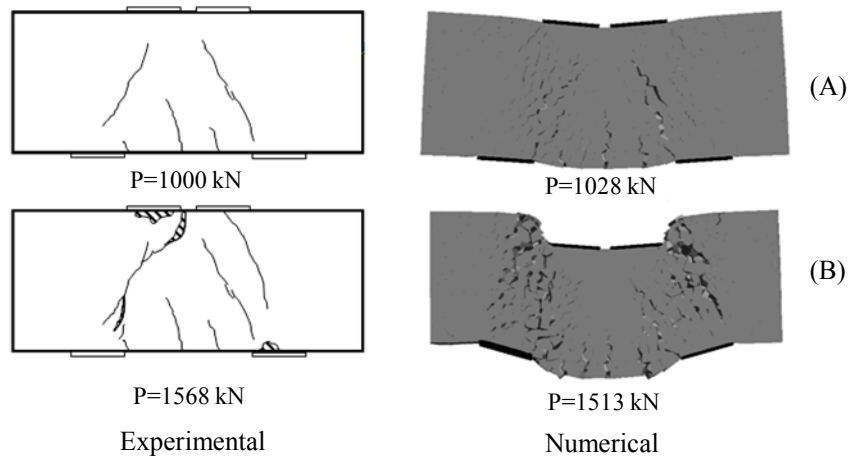
Fig. 5.12 BS4bw200 Crack Patterns

5.4.2 3-D Deformed Shapes

A failure mechanism can be investigated in detail by the 3-D-RBSM as it provides the 3-D deformed shape. Figures 5.13.(a) and (b) show 3-D deformed shapes at the peak and post-peak loads for BS4bw100 and BS4bw200, respectively. To indicate the failure behavior clearly, the deformed shapes are magnified by a factor of 20.

At peak load, no significant lateral deformation is observed along the compression strut for either of the cases (b, B). The lateral deformation is formed after peak load (c, C) and it increases in further post-peak loads (d, D) as shown in the figures. The lateral deformation behavior appears to be similar for each case, judging by a comparison of the figures from peak load to post-peak loads. The large lateral deformation in the post-peak region is in agreement with the spalling behavior in the experiment. Moreover, relative lateral deformation is significantly higher in the case of BS4bw100, which is similar to the experimental results. Therefore, 3-D behavior is important in understanding the post-peak behavior of RC short deep beams, and the 3-D RBSM can show this behavior realistically.

(a) BS4bw100　　　　　　　　　　**(b)** BS4bw200
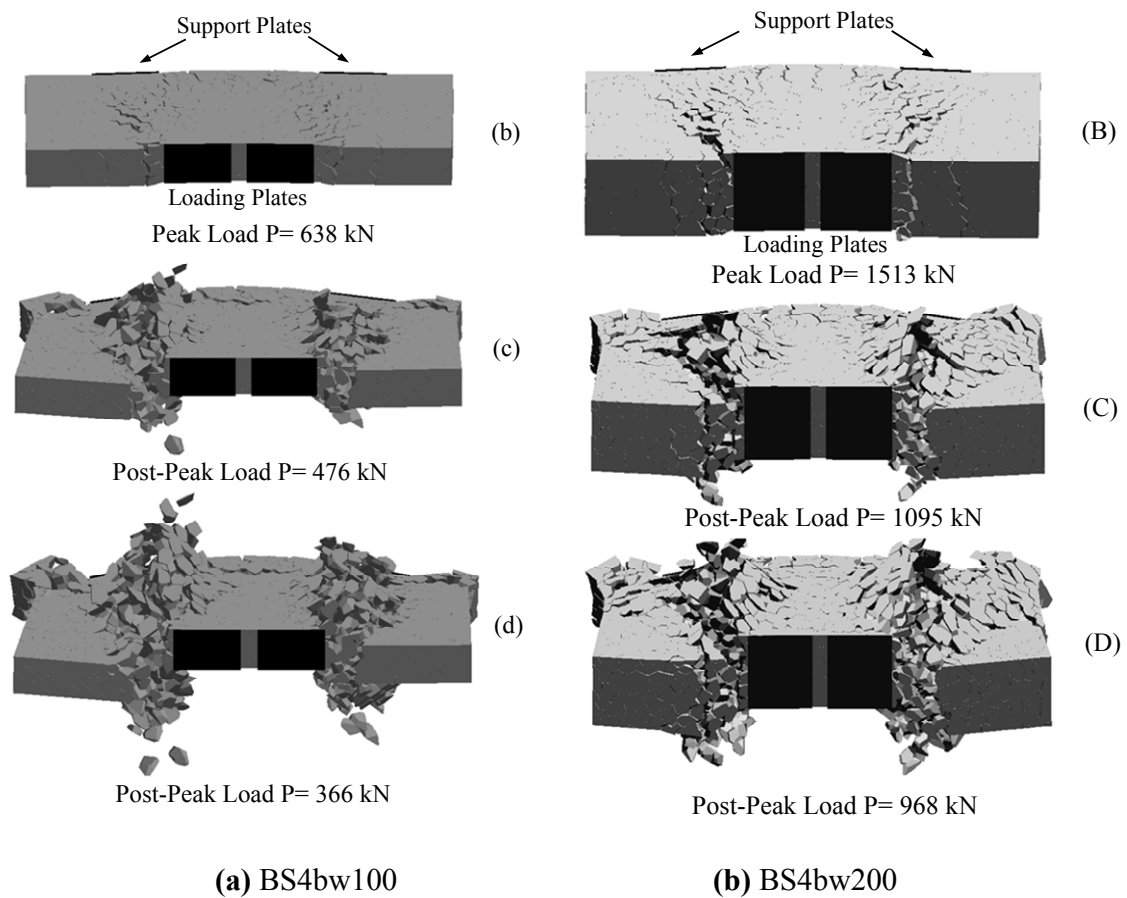
Fig. 5.13 3-D Deformed Shapes

5.4.3 Compression Strut

The principal stress distribution on the longitudinal middle section of BS4bw200 is shown in Fig. 5.14. The maximum stress range is set to 19.50 MPa, which is the compressive strength of concrete (fc'). Figure 5.14.(a) shows the principal stress distribution at pre-peak load P=1028 kN (A). The strut initiation is shown in the figure. Figure 5.14.(b) shows the principal stress distribution at the peak load (B). The strut can be seen clearly in the figure. At post-peak load P=1095 kN (C), the stress decreases near the loading plates, where it remains similar near middle height of the beam and support plates (Fig. 5.14.(c)).

(a) Pre-Peak P= 1028 kN

(b) Peak P= 1513 kN

(c) Post-Peak P= 1095 kN

	-19.50
	-16.25
	-13.00
	-9.75
	-6.50
	-3.25
	0.00
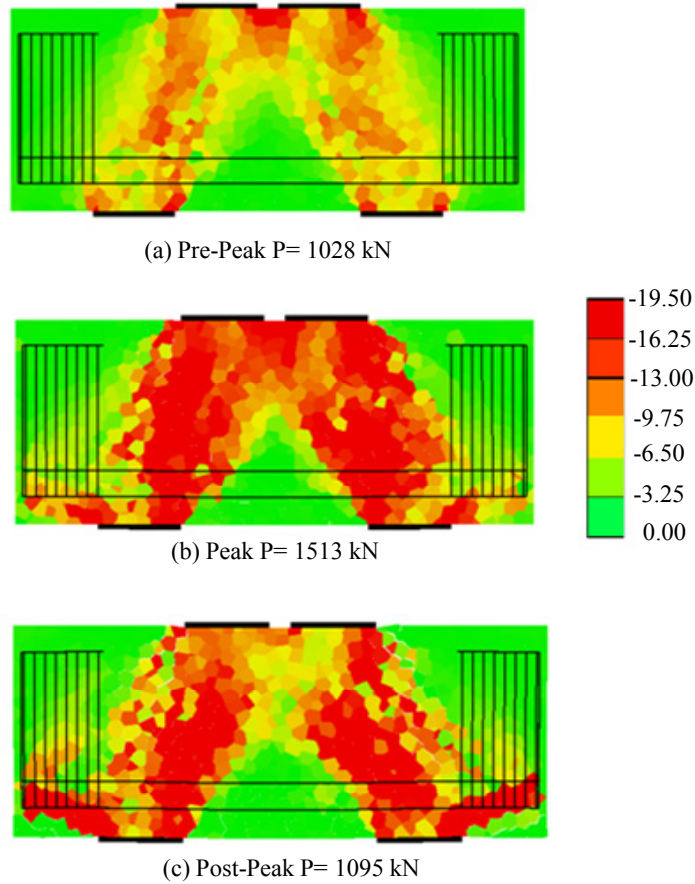
Fig. 5.14 Principal Stress Distribution on Longitudinal Middle Section

In order to discuss the 3-D effect in short deep beam, strut widths along the strut are compared using Fig. 5.14. The strut is determined by the area where the stress is greater than 0.5 fc' and the measured widths are normalized by plate width. The widths are measured near the loading point (Point1), the middle height of the beam (Point 2), and the support point (Point 3) shown in Fig. 5.15.(a).

A comparison of normalized strut widths at Points 1, 2 and 3 is given in Fig. 5.15.(b). The widths are measured on both the surface and middle longitudinal sections.

80

(a) Strut Measurement Points
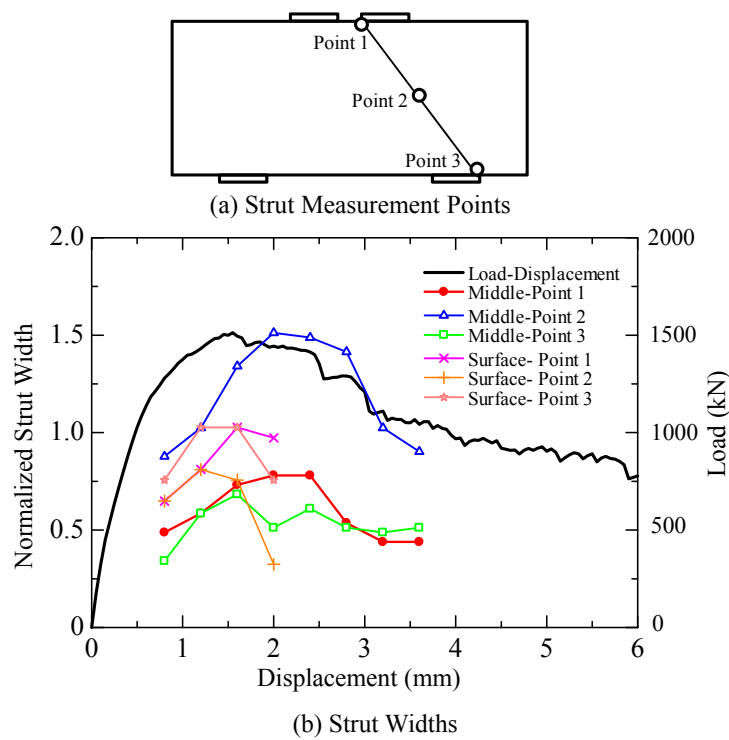
(b) Strut Widths

Fig. 5.15 Comparison of Strut Widths

In the pre-peak region, the widths increase in all cases. Near the peak load, the strut width at Point 2 is about 1.5 times of the plate width on the middle section, while it is smaller than the plate width on the surface section. At Points 1 and 3, the widths on the surface section reach the plate width near the peak load. On the middle section, the strut widths are less than the plate width.

On the surface section, the strut disappears just after the peak load, and no post-peak region is observed due to spalling of concrete on the surface. On the other hand, the strut on the middle section is observed in further post-peak loads because of confining effect in the middle of the beam. At Points 1 and 2 on the middle, the widths decrease in a similar way as with the load-displacement curve in the post peak, where the strut is almost constant at Point 3.

Figure 5.16 shows the change of the normalized stress along the compression strut. The stress values are measured near the loading point (Point1), the middle height of the beam (Point 2), and the support point (Point 3) shown in Fig. 5.15.(a). The stress is measured both on the middle and surface longitudinal section for three points separately. The stress values are normalized by compressive strength of concrete (fc').

The stress values near the peak load on the middle section are significantly greater than the stress on the surface section. The stress of point 1 on the middle section reaches to almost two times of the one on the surface section. In the post-peak region, the stress on point 2 (middle-height) on the surface section suddenly decrease due to spalling of concrete. On the other hand, in the case of middle section, the stress value exceeds 1.5 times of fc' that shows the confining effect of concrete on the middle section. Moreover, the stresses on point 1 and 3 on the middle section are also greater than the ones on the surface section. That is the stress along the strut shows different behavior between middle and surface section.
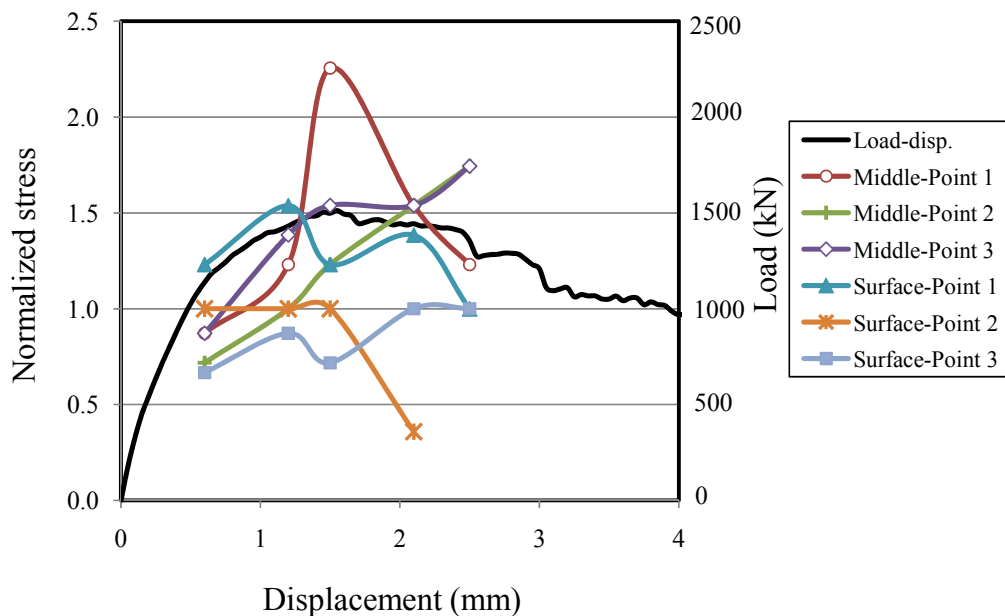
Fig. 5.16 Comparison of Stress

The results show the reason for the different behavior between surface and middle sections are the confining effect in the middle part of the beam after concrete spalling on the surface.

5.5 Shape Effect

5.5.1 Effect of beam width

The experimental results of BS2bw100, BS2bw200 and BS2bw300 specimens are compared in order to investigate the effect of beam width in BS2bw series. Figure 5.17 shows the comparison of nominal shear stress for the specimens. In the pre-peak region, there is no effect of the beam width. Moreover, there is no significant difference in the maximum shear stress values. On the contrary, the post-peak behavior is different. More ductile behavior in the post peak region is observed by increase of the beam width as seen in the figure.
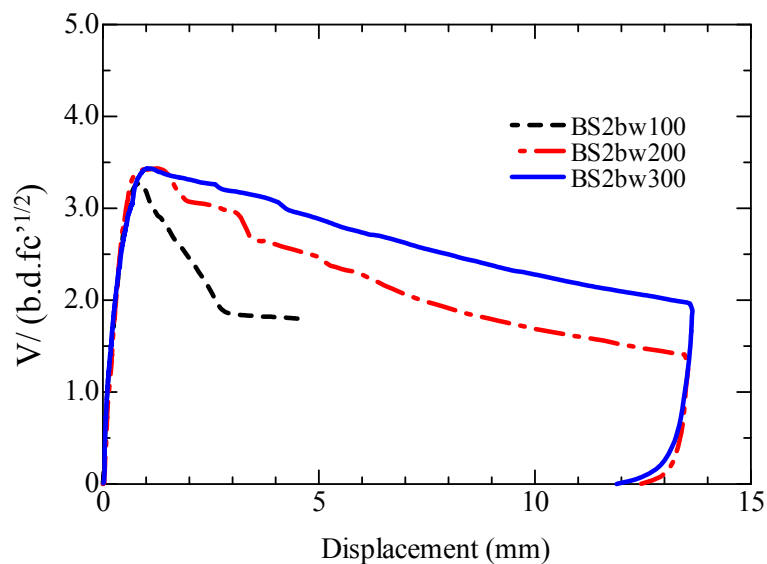
Fig. 5.17 Nominal Shear Stress (BS2bw)

In order to investigate the effect of beam width in BS4bw series, the experimental results of BS4bw100 and BS4bw200 specimens are compared. Figure 5.18 shows the comparison of nominal shear stress for the specimens. As seen in the figure, there is no effect from beam width in the pre-peak region. The maximum shear stress is slightly higher for BS4bw200 case. On the contrary, the post-peak behavior is different.
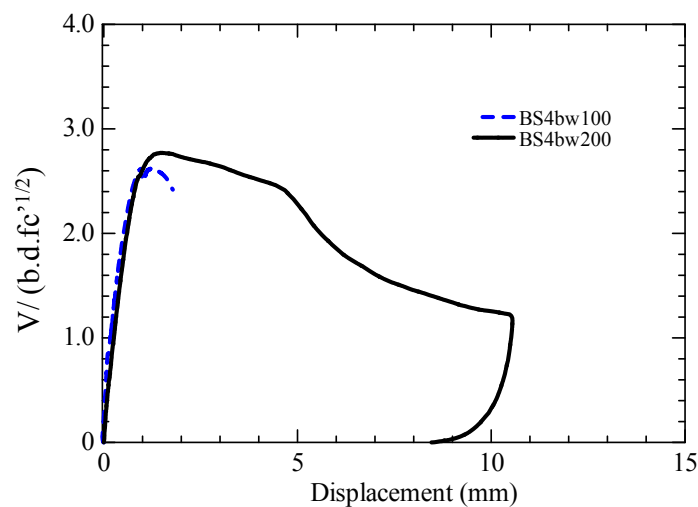
Fig. 5.18 Nominal Shear Stress (BS4bw)

Figure 5.19.(a) shows the final failure pattern of BS4bw100 specimen. The beam failed suddenly under shear compression as a result of excessive lateral deformation and spalling of concrete on the surface. The lateral deformation was observed only on one of the compression strut of the beam. On the other hand, the beam with the larger width (BS4bw200) shows softening behavior in the post-peak region as seen in Fig.5.18. The final failure pattern of the beam is shown in Fig. 5.19.(b). Lateral deformation and spalling of concrete formed along the strut surface. The beam continued to carry the load as there was sufficient interior concrete, as opposed to the case for BS4bw100. Moreover, the lateral deformation occurred on two of the compression strut of the beam in the early post-peak

region, which is another reason for softening behavior. However, the damage was localized only on one side of the beam in further post-peak loads. This behavior is confirmed by the change of slope after a mid-span displacement of about 5 mm in the softening part (see Fig. 5.18).
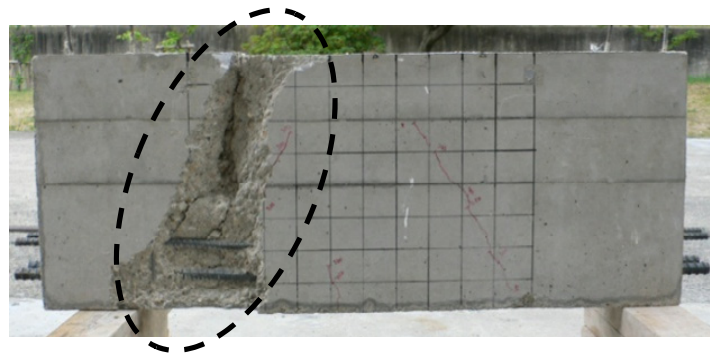
(a) BS4bw100
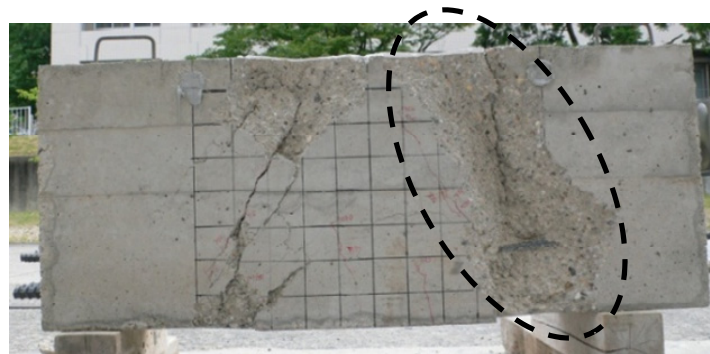
(b) BS4bw200

Fig. 5.19 Final Failure Pattern

The comparison of the relative failure depths along the beam width on the failed beams is shown in Fig. 5.20. The sum of the depth measured on the two surface of the strut is taken into account and it is given as a percentage relative to the beam width. The depth near the loading point in the narrower beam extends to 74% of the beam width as seen in the figure, whereas it is only 27% in the wider beam. It is clearly understood that sudden failure occurred in BS4bw100 as the remaining interior concrete near the loading point was

relatively small to carry the load toward to the strut, after the large amount of concrete spalling. Otherwise, the load could have been transmitted from loading points to the support in the post-peak region of BS4bw200 as there was sufficient remaining interior concrete and, therefore, ductile behavior was observed. In the figure, the absolute failure depths are given within the parenthesis on the points. The remaining thicknesses of the BS4bw100 beam are only 26 mm, 40 mm and 61 mm near the loading point, middle height of the strut, and support point, respectively, while 146 mm, 85 mm and 152 mm values were recorded for the BS4bw200 beam. The reason for sudden failure can be clearly understood through this comparison, that is, the remaining thickness, especially near the loading point, is too small to carry the load after the peak in BS4bw100. On the other hand, it was significantly higher in the BS4bw200 beam, which could transmit the load from the loading points to support along the strut.
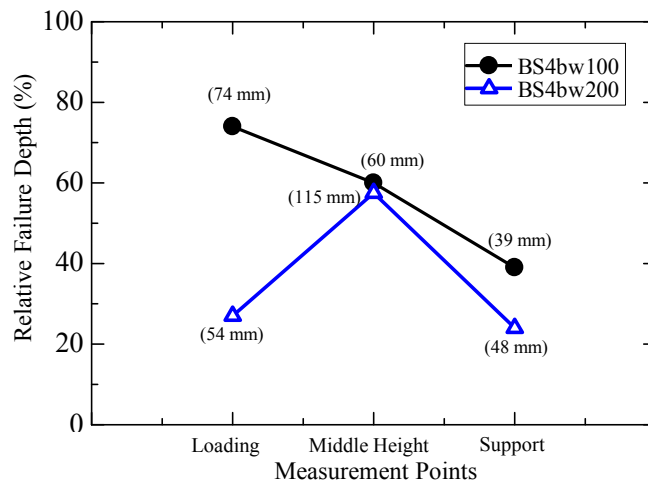
Fig. 5.20 Comparison of Relative Failure Depths

The effect of beam width on short deep beam behavior is also investigated numerically for BS4bw series. In addition to the BS4bw100 and BS4bw200 specimens, the analyses are

extended to specimens having larger beam widths of 300 mm and 400 mm given in Table 5.3 in order to clarify the effect of beam width. The length and the height of specimens are the same for all cases where only the widths are different, that is: 100 mm, 200 mm, 300 mm and 400 mm.

Table 5.3 Properties of Specimens

Specimen	Beam Length L(mm)	Overall height h (mm)	Effective Depth d (mm)	Beam Width (mm)	Shear Span (mm)	a/d	Plate Width (mm)	Longitudinal Reinforcement As (mm^2)	ρ_s (%)	fc' (MPa)
BS4bw300	1000	400	320	300	160	0.5	160	2479	2.58	20.0
BS4bw400	1000	400	320	400	160	0.5	160	3306	2.58	20.0

Figure 5.21 shows a comparison of nominal shear stress due to beam width. The shear stress shows increment with the increase in beam width. Moreover, more ductile behavior in the post-peak region is observed in the case of larger beam widths, as shown in the figure. The results agree with the observations from the experiments.
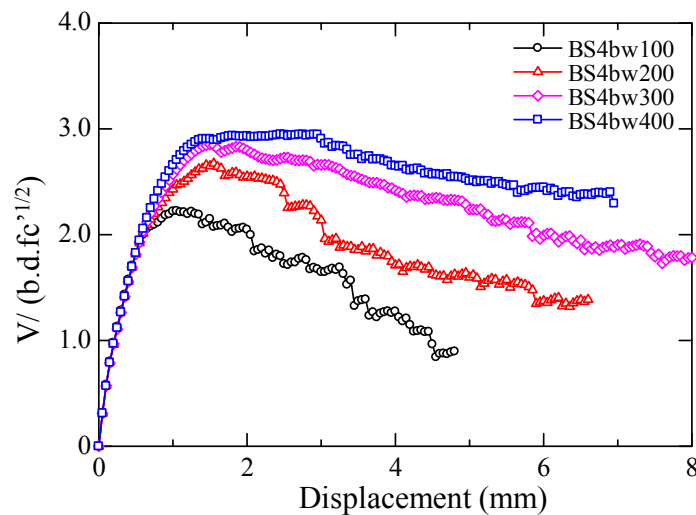
Fig. 5.21 Nominal Shear Stress Due to Beam Width

The principal stress distribution of the cross-sectional area at the middle of the shear span is shown in Fig. 5.22. The maximum compressive stress range is set to 40 MPa. The

stress is measured at mid-span displacement values of 1 mm, 3 mm and 4.5 mm. In the case of b=100, no stress concentration is observed after the peak load. The result agreed with the experimental results, in which a large amount of lateral deformation was observed and no interior concrete remained. Therefore, sudden failure occurred just after peak load was reached.
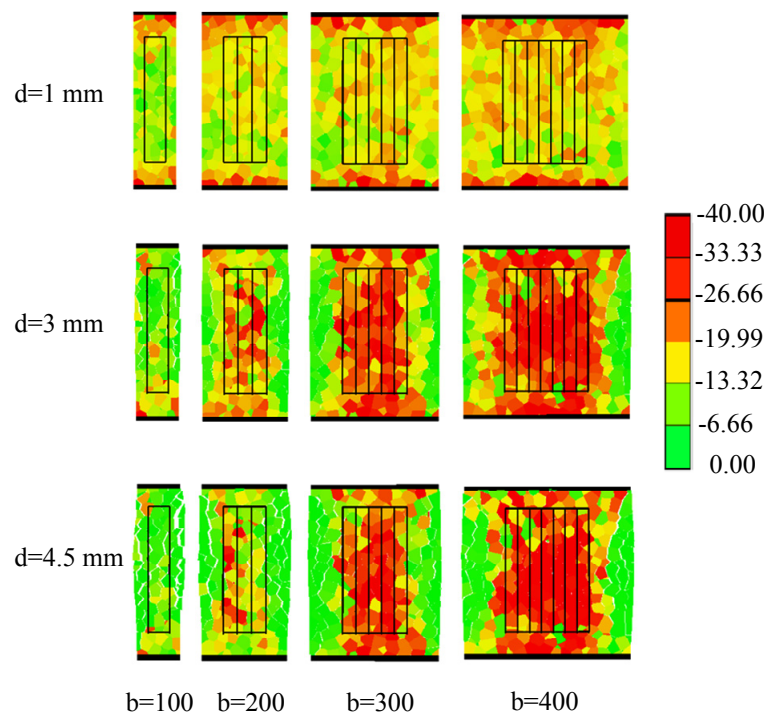
Fig. 5.22 Principal Stress Distribution on Cross-Sectional Area

On the other hand, in the b=200 case, the stress near the surface decreases due to spalling of concrete and stress concentration occurs at post-peak (d=3.0 mm) on the core concrete and then it decreases at post-peak (d=4.5 mm), where the maximum stress on the cross-section is 43 MPa that is 2.2 times that of fc'. Other than that, the stress concentration in the case of b=300 and 400 is observed both at post-peak (d=3.0 mm) and at post-peak (d=4.5 mm). The maximum stress at d=4.5 mm is 55 MPa (2.75fc') and 63 MPa (3.15fc') for

the b=300 and 400 mm cases respectively. The higher maximum stress is induced due to confinement effect in core concrete for the larger beam widths. Therefore, the 3-D stress state in concrete is dominant for larger widths.

The stress release area near the surface increases on the middle-height of the beam and it decreases near the loading and support points. The tendency agrees with the absolute failure depth of the experimental result of BS4bw200 (see Fig. 5.20). The depths of the stress release area are almost similar with the different widths. Therefore, the relative failure depth decreases by the increase of beam width that leads to more ductile behavior for higher beam widths. Thus, the effect of beam width in short deep beams is clearly understood. Namely, a large amount of spalling occurs in the case of smaller beam widths that may cause sudden failure due to a lack of interior concrete remaining in place. On the other hand, interior concrete is still available to resist the loads in the post-peak region due to the confinement effect in the case of larger beam widths.

5.5.2 Effect of depth

The nominal shear stress between BS2bw100 and BS4bw100 specimens are compared as shown in Fig. 5.23 in order to investigate the effect of the effective depth (d) in short deep beams. The depth of the BS4bw100 is 2 times of the BS2bw100 specimen. As seen in the Fig. 5.23, similar behavior is observed in the pre-peak region. However, the nominal shear strength as well as the post-peak behavior is different. The maximum shear stress is remarkably larger in BS2bw100, which has smaller size. On the other hand, the post-peak behavior of BS2bw100 specimen is observed where no post-peak behavior is observed in BS4bw100 case, which has larger depth, due to sudden failure of the beam after the peak load. That is, the shape effect resulting from the depth is significant in short deep beams.
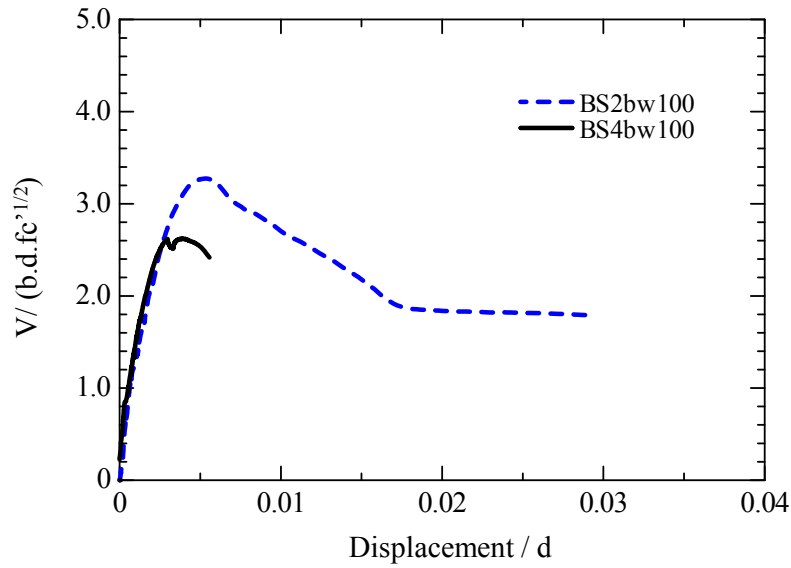
Fig. 5.23 Effect of Depth on Nominal shear stress

5.6 Size Effect

To investigate the size effect in short deep beams, the nominal shear stress for the BS2bw100 and the BS4bw200 specimens are compared as shown in Fig. 5.24. All dimensions of the BS4bw200 are 2 times of the BS2bw100 specimen. As seen in the figure, the behavior in the pre-peak region is similar in both cases. However, the maximum shear stress is larger in BS2bw100 specimen, which has smaller size. On the other hand, BS4bw200 specimen shows more ductile behavior in early post-peak loads compared to BS2bw100 case. Then, the slope of the curve becomes similar in the further post-peak loads as seen.
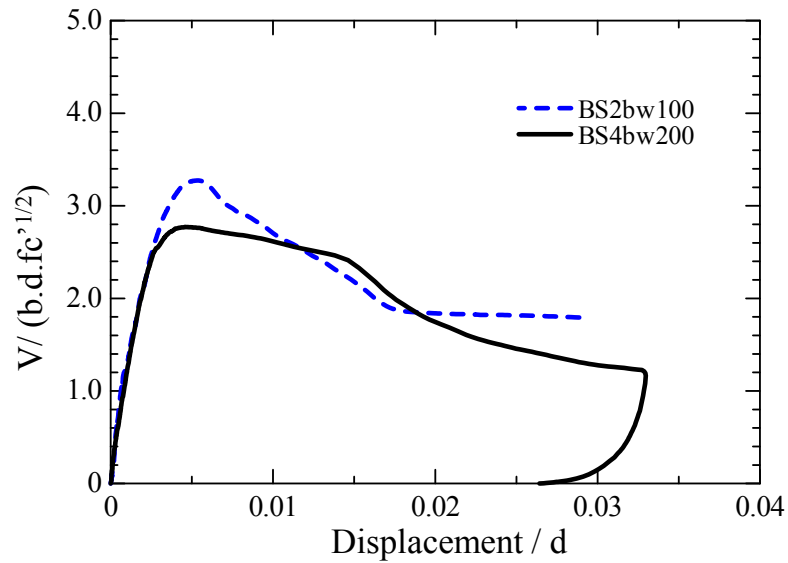
Fig. 5.24 Size Effect on Nominal shear stress

5.7 Summary and Conclusions

In order to clarify 3-D behavior as well as the shape effect resulting from beam width in short deep beams, two series of specimens, which are BS2bw and BS4bw series, with a/d=0.5 and without stirrups were tested. BS2bw and BS4bw series have the height of 200 mm and 400 mm respectively.

In BS2bw series, the beams failed in shear compression with spalling of concrete for all beam width cases. However, more ductile behavior is observed by increase of the beam width.

In BS4bw series, sudden failure occurred in the smaller width beam due to the relatively large amount of concrete spalling, and more ductile behavior is obtained in wider beam. The effect of beam width on the behavior of short deep beams is observed clearly.

The beams of BS4bw100 and BS4bw200 are simulated by the 3-D RBSM, and the

results in terms of load-displacement curve and crack pattern agree reasonably well with the experimental results. Furthermore, 3-D deformations as well as the strut width on the surface and middle longitudinal sections are investigated. The importance of the 3-D effects resulting from the spalling of concrete on the surface, and the confinement effects in the middle section is confirmed.

The effect of beam width in short deep beams is investigated numerically by comparing four beams having widths of 100 mm, 200 mm, 300 mm and 400 mm where the height of the specimens is the same. As with the experiments, ductile behavior is observed as a result of the increase in beam width. Moreover, the effect of beam width, spalling behavior on the surface, and the confinement effect in the middle section are clarified by 3-D RBSM. The ductile behavior resulting from the increase in beam width is caused by the difference of the core concrete width and the confinement effect of the core concrete.

Shape effect resulting from the depth is investigated by comparing the nominal shear stress between BS2bw100 and BS4bw100 specimens. The depth of BS4bw100 is 2 times of BS2bw100 specimen. The nominal shear strength is larger in the smaller beam and the post-peak behavior is observed. However, no post-peak region is observed in the larger beam due to sudden failure just after the peak load. That is, the effect of depth on behavior is significant in short deep beams.

Size effect in short deep beams are investigated by comparing BS2bw100 and BS4bw200 specimen, which has two times dimension of BS2bw100. The maximum shear stress increases in BS2bw100 and more ductile behavior in early post-peak region are observed in BS4bw200 specimen.

6. A New Horizontal Stirrup Arrangement for Short Deep Beams

6.1 Introduction

In short deep beams having shear span to depth ratio (a/d) less than 1.0, the compressive shear failure occurs with spalling of concrete along the compression struts. Moreover, three-dimensional behavior is important for short deep beams as discussed in the previous chapters. On the other hand, it was clarified that there is no significant effect of stirrup along the vertical direction in deep beams with a/d less than 1.0 as discussed in Chapter 3 and 4. This means that, no effective reinforcement method in order to enhance the structural performance of short deep beams has been proposed yet.

In this chapter, a new reinforcement method named "horizontal stirrup arrangement" is proposed for short deep beams by considering three-dimensional effects, which was confirmed by the experimental and the numerical results in the previous chapters. In this method, stirrups are placed within the shear span horizontally along the beam height. The proposed stirrup design provides the increase of load carrying capacity of a short deep beam as well as the ductility by confinement effect of horizontal stirrups. The effectiveness of the

horizontal stirrup arrangement is confirmed by both experimentally and numerically.

6.2 Experimental Program

Five series of short deep beams including various specimen sizes and volumetric ratios were designed and tested as described in Table 6.1. The dimensions and details of the specimens of BS2, BS3, B3-0.5, BS3-200 and B3-1.0 series are given in Fig. 6.1, 6.2, 6.3, 6.4 and 6.5. In Table 6.1, S_v and S_l represents the spacing of vertical and horizontal stirrups respectively. Four series have a/d ratio of 0.5 and one series have a/d ratio of 1.0, which is also investigated in order to demonstrate different behavior of deep beams with horizontal stirrup for larger a/d ratio.

BS2 series has three specimens including control beam (BS2), the beam with vertical stirrup (BS2-VS) and the beam with horizontal stirrup (BS2-LS). The beam width and height is 100 mm and 200 mm respectively for each specimen. In this series, the effects of vertical and horizontal stirrups are compared and the effectiveness of horizontal stirrup is confirmed.

BS3 series has four specimens including control beam (BS3) and three beams with horizontal stirrups (BS3-LS70-h, BS3-LS70, BS3-LS35) having different volumetric ratios. The beam width and height are 150 mm and 300 mm respectively for each specimen, which has 1.5 times size of BS2 series. By this series, size effect in deep beams with horizontal stirrups is investigated by comparing BS2 series. Moreover, the effect of volumetric ratio on behavior is examined.

B3-0.5 series has four specimens including control beam (B3-0.5), the beam with vertical stirrup (B3-0.5-VS) and two beams with horizontal stirrups (B3-0.5-LS70, B3-0.5-LS35) having different volumetric ratios. The beam width and height are 100 mm and 300

mm respectively for each specimen, where the width of BS3 series is 1.5 times of the width of B3-0.5 series. In this series, the effects of vertical and horizontal stirrups on behavior for larger beam sizes are compared. The effect of volumetric ratio for horizontal stirrup cases is examined. Moreover, the shape effect resulting from the beam height is investigated by comparing BS2 series.

BS3-200 series has two specimens including control beam (BS3-200) and a beam with horizontal stirrup (BS3-200-LS). The beam width and height are 200 mm and 300 mm respectively for each specimen, of which beam width is 2.0 times of the one in B3-0.5 series. By comparison of BS3, B3-0.5 and BS3-200 series, the shape effect resulting from the beam width for h=300 mm case is investigated. Moreover, the effect of volumetric ratio due to the change in the beam width is examined.

B3-1.0 series has three specimens including control beam (B3-1.0), the beam with vertical stirrup (B3-1.0-VS) and a beam with horizontal stirrup (B3-1.0-LS). The shear span to depth ratio (a/d) is 1.0, which is also investigated in order to demonstrate different behavior of deep beams with horizontal stirrup for larger a/d ratio.

Figure 6.6 shows the experimental setup for four-point loading that was applied to the test specimens. The load was distributed to the bearing plates using a steel beam. Steel rollers were used between the loading plates and the steel beam. A mid-span and support deflections were measured and a relative mid-span deflection was taken into consideration by subtracting the support displacements.

Mixture proportion of concrete is given in Table 6.2. The same mixture proportion was used for all specimens, however the casting dates and the durations between casting and tests were different for the series. Specimens were cured with water after remolding.
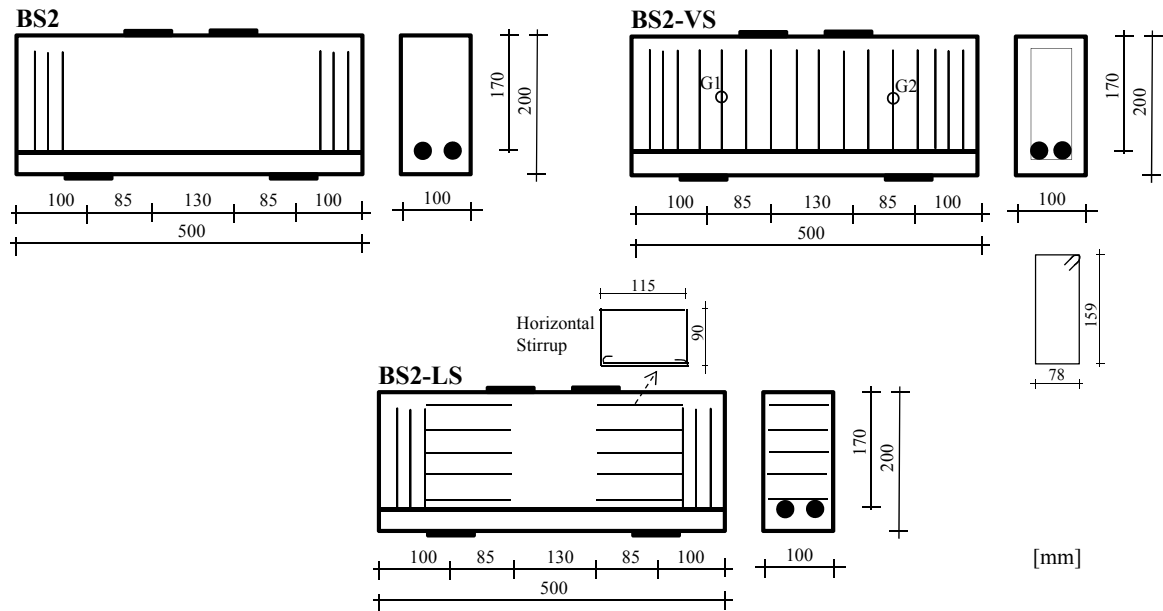
Fig. 6.1 Overview of BS2 Series
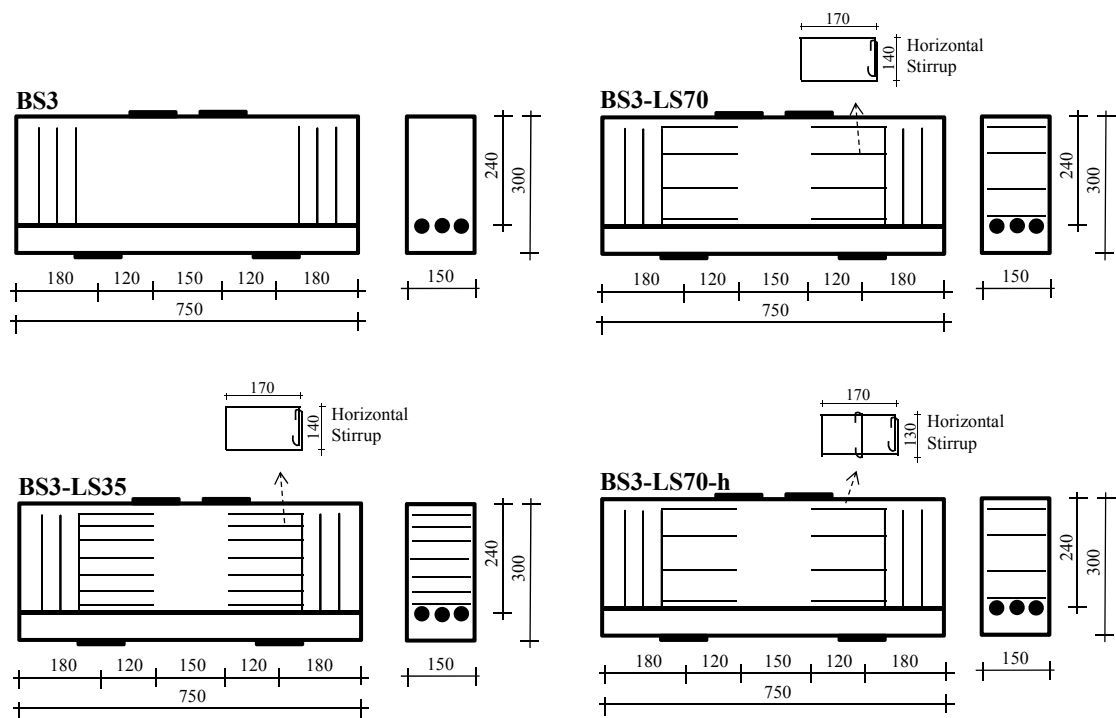
Fig. 6.2 Overview of BS3 Series

96

Table 6.1 Details of Specimens

Series	Specimen	a/d	Beam Width b(mm)	Beam Height h (mm)	Plate Width h (mm)	Longitudinal Reinforcement			Stirrup			Volumetric Ratio	Compressive Strength fc' (MPa)
						As mm²)	fy (N/mm²)	ρ_t (%)	fyw (N/mm²)	S_v	S_l		
BS2	BS2	0.5	100	200	60	774.2 (2D22)	345.0	4.55	-	-	-	-	20.5
	BS2-VS		100	200	60				345.0	35	-	0.021	20.5
	BS2-LS		100	200	60				345.0	-	35	0.029	20.5
BS3	BS3	0.5	150	300	100	1520.1 (3D25)	396.0	4.22	-	-	-	-	17.2
	BS3-LS70-h		150	300	100				368.0	-	70	0.011	17.2
	BS3-LS70		150	300	100				368.0	-	70	0.010	20.6
	BS3-LS35		150	300	100				368.0	-	35	0.017	17.2
B3-0.5	B3-0.5	0.5	100	300	100	774.2 (2D22)	372.2	3.23	-	-	-	-	32.6
	B3-0.5-VS		100	300	100				388.2	70	-	0.009	32.6
	B3-0.5-LS70		100	300	100				388.2	-	70	0.010	32.6
	B3-0.5-LS35		100	300	100				388.2	-	35	0.017	32.6
BS3-200	BS3-200	0.5	200	300	100	1548.4 (4D22)	372.2	3.23	-	-	-	-	28.6
	BS3-200-LS		200	300	100				388.2	-	70	0.007	28.6
B3-1.0	B3-1.0	1.0	100	300	100	774.2 (2D22)	372.2	3.23	-	-	-	-	35.7
	B3-1.0-VS		100	300	100				388.2	70	-	0.008	35.7
	B3-1.0-LS		100	300	100				388.2	-	70	0.010	35.7

Table 6.2 Concrete Mixture Proportion

G_{max} (mm)	Water-Cement Ratio W/C (%)	Mass Per Unit Volume (kg/m^3)			
		Water W	Cement C	Sand S	Gravel G
15	0.56	166	294	779	990

* An admixture was used having an amount of 0.4% of Cement
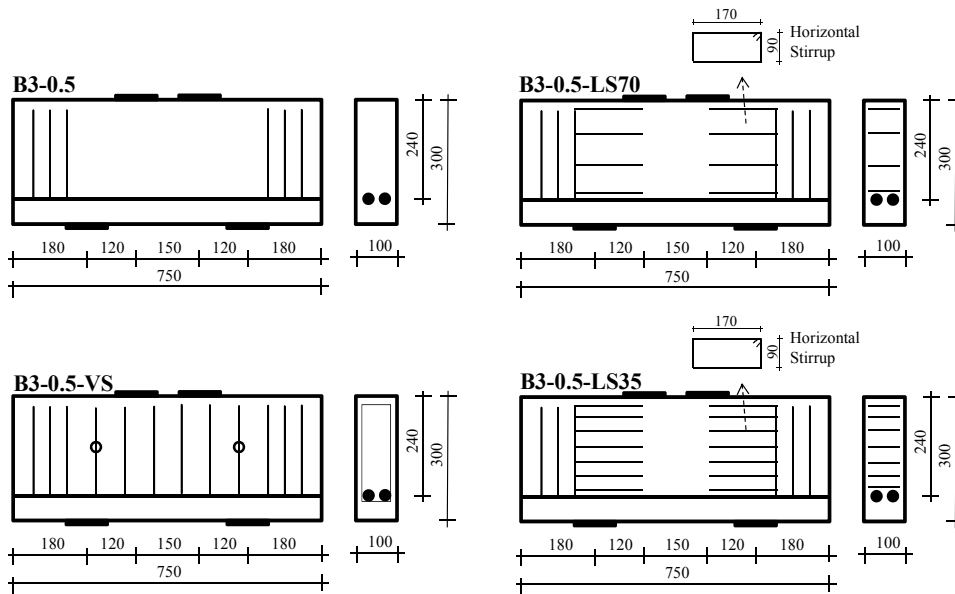
Fig. 6.3 Overview of B3-0.5 Series
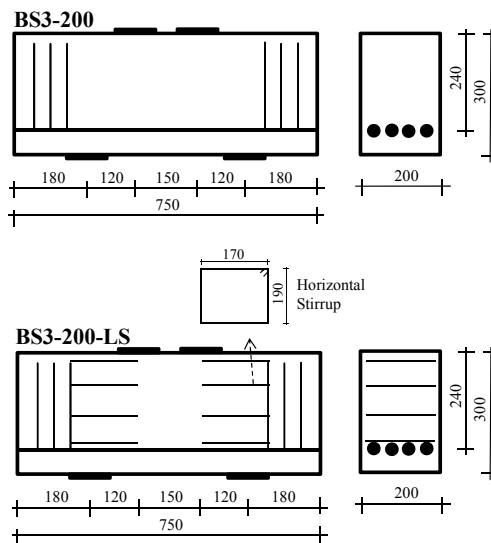
Fig. 6.4 Overview of BS3-200 Series

98
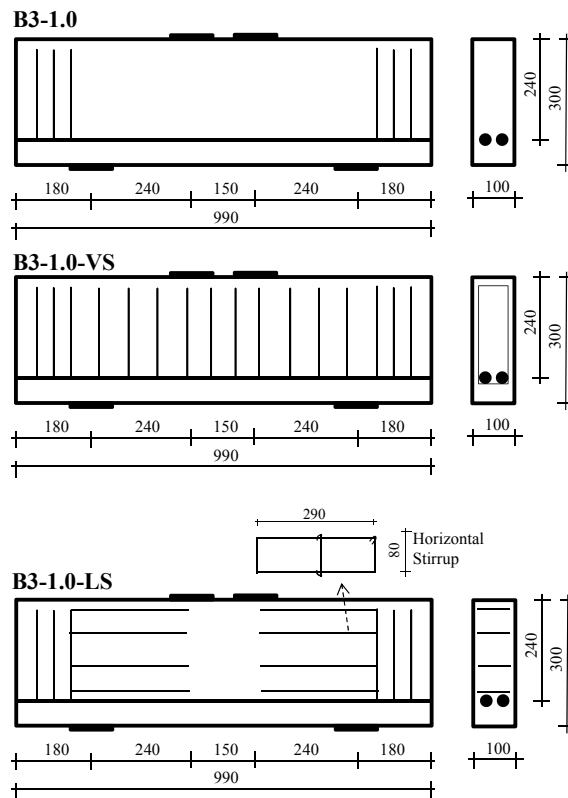
Fig. 6.5 Overview of B3-1.0 Series

Fig. 6.6 Experimental Setup

99

6.3 Experimental Results

6.3.1 BS2 Series

The comparison of load displacement curves for BS2, BS2-VS and BS2-LS specimens is given in Figure 6.7. The load-displacement curve of BS2 is shown by dashed line where the curve of BS2-VS is given by dashed-dotted line. The peak load of BS2 and BS2-VS specimens are 314 kN and 300 kN respectively. There is no effect of vertical stirrup on the peak load as seen in the figure. Figure 6.8.(a) shows the strain of vertical stirrup in BS2-VS specimen. The strain measurement points are given in Figure 6.1. The vertical stirrup did not yield before the post-peak load of P=262 kN as shown in Figure 6.8.(a). Therefore, the vertical stirrup does not increase the peak load. On the other hand, more ductile behavior is observed after the post-peak load of P=262 kN between BS2 and BS2-VS due to yielding of vertical stirrup hereafter.
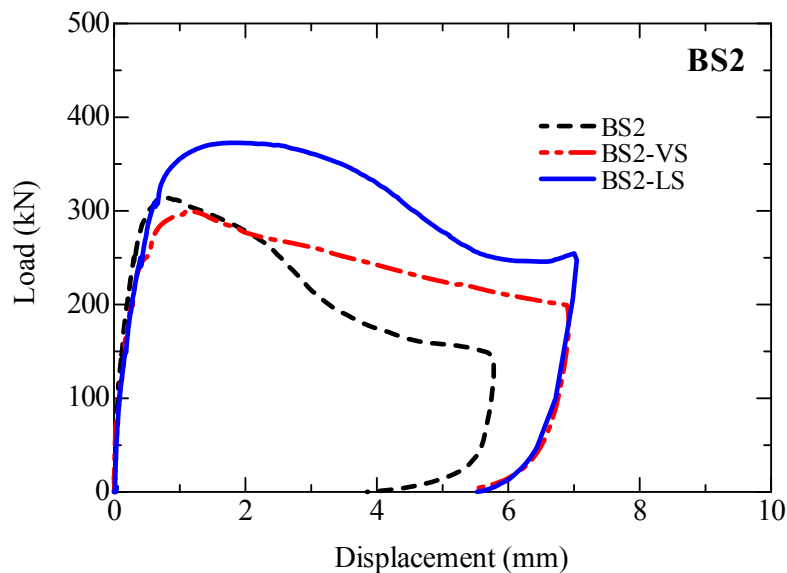
Fig. 6.7 Load-Displacement Curves

The load-displacement curve of BS2-LS specimen is given by solid line in Figure 6.7. The peak load is 373 kN, which is higher value than that of no horizontal stirrup case (BS2) and vertical stirrup case (BS2-VS). Hence, the use of proposed horizontal stirrup increases the peak load significantly. Moreover, the curve of BS2-LS specimen shows more ductile behavior compared to BS2 specimen. That is, the horizontal stirrup is effective for short deep beams having a/d=0.5 and it increases the load capacity as well as the ductility. Figure 6.8.(b) shows the strain of horizontal stirrups in BS2-LS specimen. The strain measurement points are given in Figure 6.8.(c). One of the horizontal stirrups yielded as shown. Moreover, most of the stirrups have the larger strain values than that of vertical stirrups before the peak load. Therefore, the horizontal stirrups are effective by providing the confinement effect within the compression strut.

Figure 6.9.(a) shows the failure of BS2 specimen. As seen in the figure, the compressive shear failure occurred leaded by diagonal shear crack with large amount of spalling of concrete. In BS2-VS specimen, the main shear crack occurs steeply between vertical stirrups as seen in Figure 6.9.(b). The failure of BS2-LS beam is given in Figure 6.9.(c). The horizontal stirrups within the shear span were reduced the amount of spalling with confinement effect as seen. Moreover, the failure occurred with many shear cracks formed between stirrups rather than one main diagonal crack. Therefore, the energy consumption was increased and more ductile behavior occurred as well as the increase of load capacity.
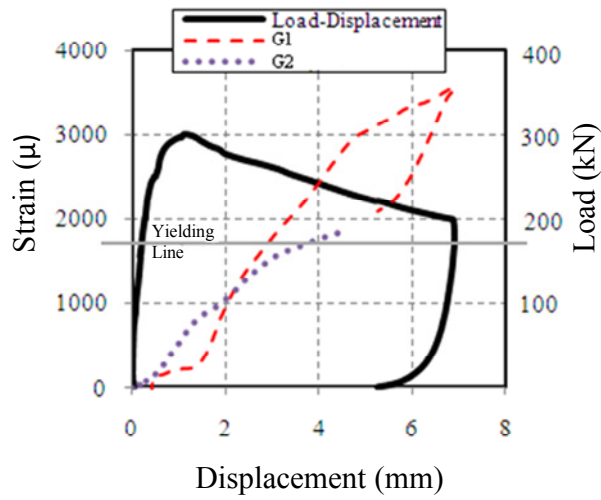
(a) Strain of Vertical Stirrup (BS2-VS)
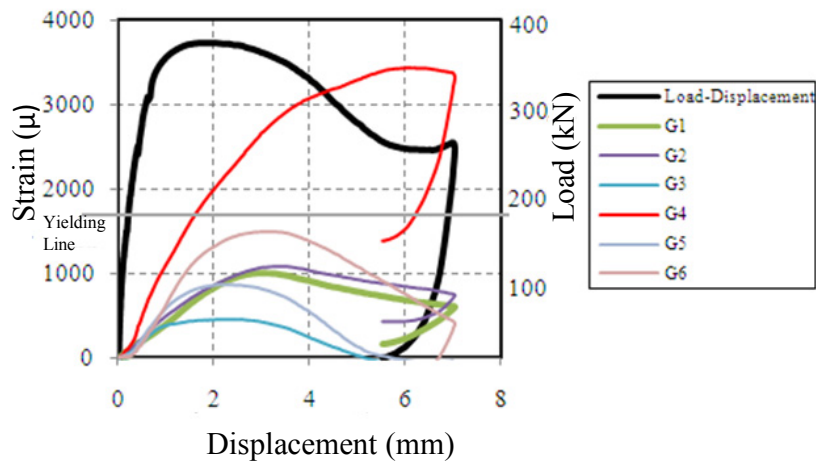
(b) Strain of Horizontal Stirrup (BS2-LS)
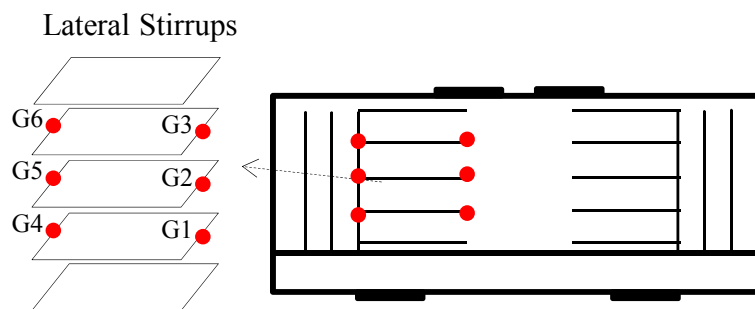
(c) Strain Measurement Locations (BS2-LS)

Fig. 6.8 Strain of Stirrups
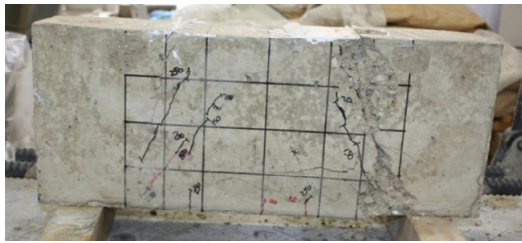
(a) BS2   (b) BS2-VS

(c) BS2-LS

Fig. 6.9 Failure of Specimens

6.3.2 BS3 Series

Figure 6.10 shows the comparison of load displacement curves for BS3, BS3-LS70, BS3-LS35 and BS3-LS70-h specimens. The peak loads are 700 kN, 773 kN, 722 kN and 682 kN respectively. There is no significant increase in load due to horizontal stirrup as seen in the figure. However, only the peak load of BS3-LS70 specimen remarkably increases since the compressive strength of concrete is higher than that of BS3, BS3-LS35 and BS3-LS70-h specimens.

On the other hand, the ductility of beams increases significantly in the case of specimens with horizontal stirrup those are BS3-LS70, BS3-LS35 and BS3-LS70-h. That is the horizontal stirrup is effective to improve the structural behavior by increasing the ductility of the beam.
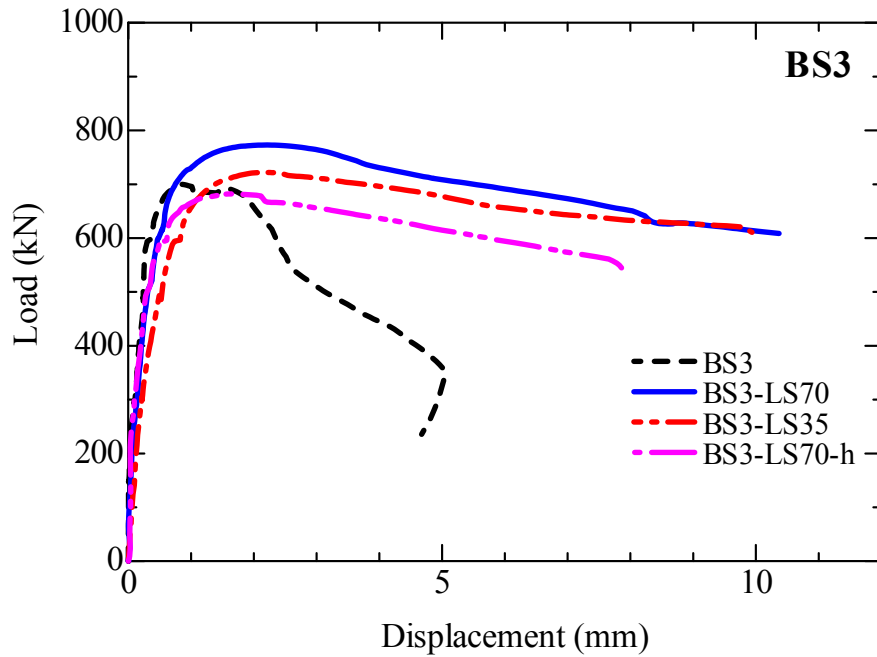
Fig. 6.10 Load-Displacement Curves

Failure of specimens is given in Fig. 6.11. In BS3 specimen, the beam failed in shear compression with spalling of concrete along the struts. One main shear crack lying from bearing plate to support occurred in this case. In BS3-LS70, BS3-LS35 and BS3-LS70-h cases, the beams also failed in shear compression. However, many shear cracks rather than one main crack occurred within the shear span. Moreover, the lengths of the shear cracks are smaller due to limitation of shear crack propagation by horizontal stirrups. The occurrence of many shear cracks causes to more energy absorption that leads to more ductile behavior in beams with horizontal stirrups as shown in Fig. 6.10.
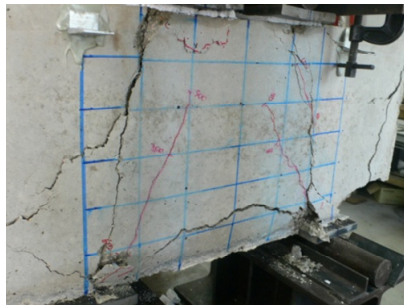
(a) BS3

(b) BS3-LS70-h

(c) BS3-LS35

(d) BS3-LS70

Fig. 6.11 Failure of Specimens

The strain of horizontal stirrups for BS3-LS70 and BS3-LS35 specimens are given in Fig. 6.13 and 6.14 respectively. Strain measurement locations are indicated in Fig. 6.12. The strain values are measured on the two arms of the stirrups; namely, along the beam width and along the beam surface. Figure 6.12.(a) shows the strain measurement locations for BS3-LS70 specimen. G1, G2, G5 and G6 show the strain along the beam surface while G3, G4, G7 and G8 represents the strain along the beam width.
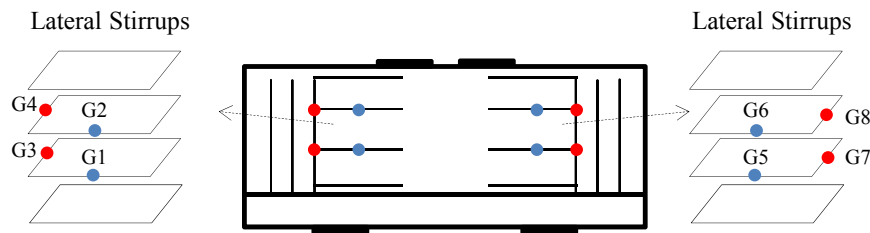
(a) BS3-LS70, B3-0.5-LS70 and BS3-200-LS
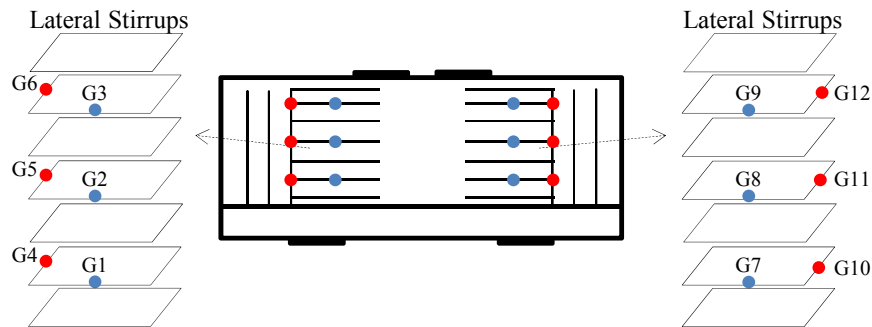
(b) BS3-LS35 and B3-0.5-LS35

Fig. 6.12 Strain Measurement Locations of Horizontal Stirrups

Figure 6.13 shows the strain of horizontal stirrups for BS3-LS70 specimen. The strain values along the beam width (G3, G4, G7 and G8) are below the yielding strain as seen in the figure. On the other hand, the stirrup arms along the beam surface (G1, G2, G5 and G6) yielded in the post peak region. It confirms that, the stirrup arm on the surface side resists the spalling of concrete as a result of confinement effect of horizontal stirrup. Therefore, more ductile behavior in the post peak region is obtained. The strain of horizontal stirrups for BS3-LS35 specimen is shown in Fig. 6.14. Only point G1, which is at the surface side, yielded in this case since the volumetric ratio of BS3-LS35 is significantly larger than that of BS3-LS70 case.
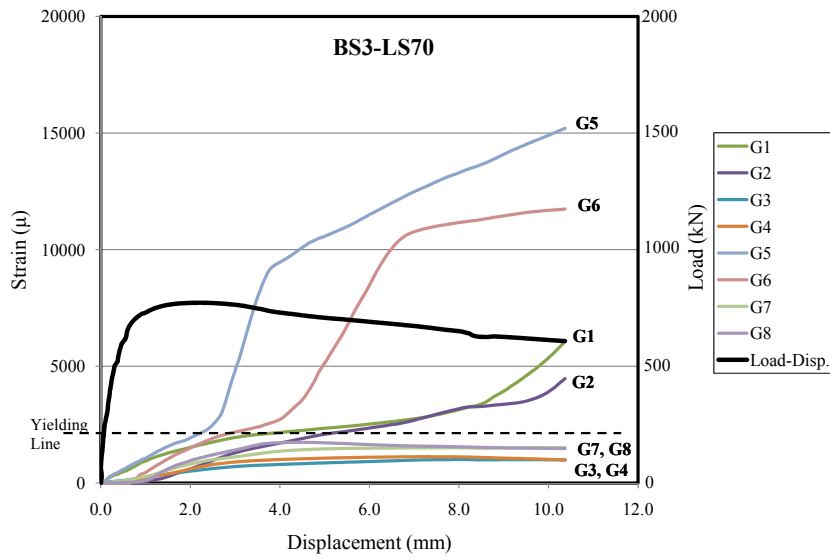
Fig. 6.13 Strain of Horizontal Stirrups (BS3-LS70)
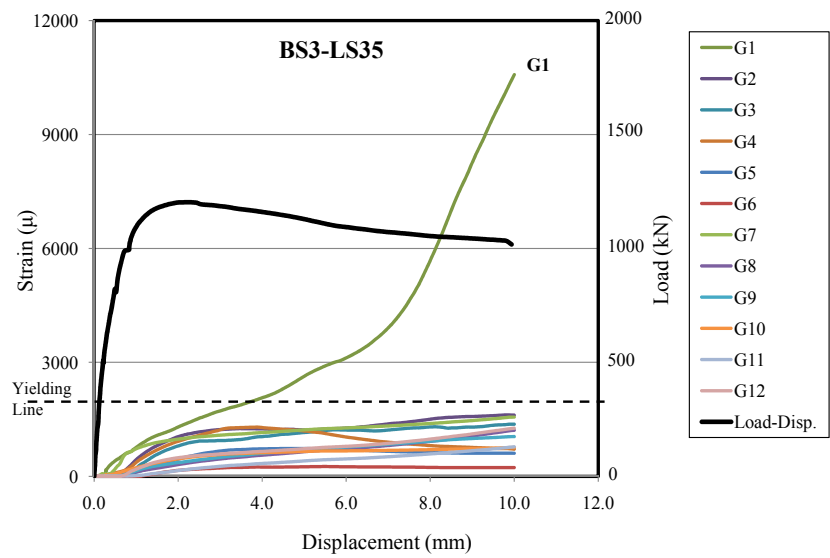
Fig. 6.14 Strain of Horizontal Stirrups (BS3-LS35)

6.3.3 B3 Series

The comparison of load displacement curves for B3-0.5, B3-0.5-VS, B3-0.5-LS70 and B3-0.5-LS35 specimens are shown in Fig. 6.15. The peak loads are 662 kN, 598 kN, 700 kN and 726 kN respectively. There is no effect of vertical stirrup as discussed in Chapter 3. In

B3-0.5-LS70 case, the load as well as the ductility increases as seen in the figure. In the case of B3-0.5-LS35 specimen, which has larger volumetric ratio, the ductility significantly increases as well as the increase in load.
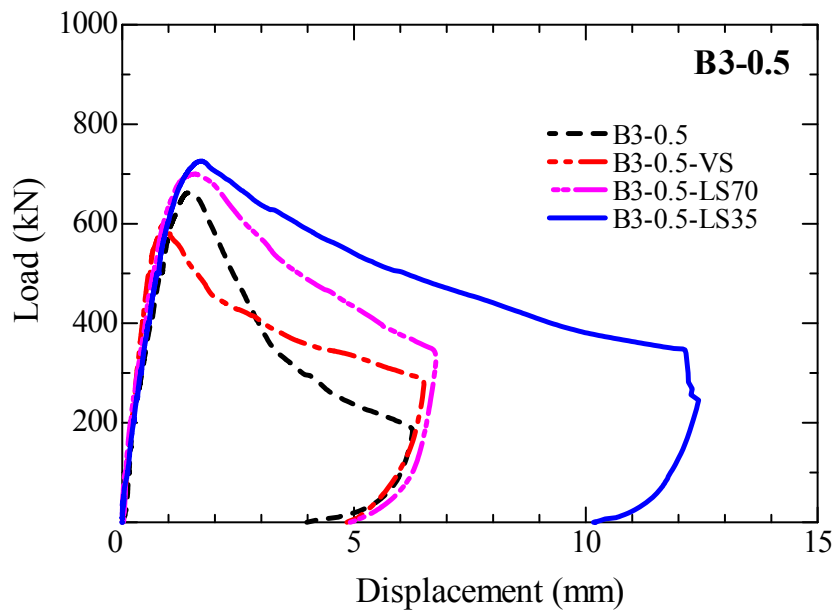
Fig. 6.15 Load-Displacement Curves

Figure 6.16 shows the failure of specimens. In B3 and B3-0.5 specimens, shear compression failure with spalling of concrete occured. One main shear crack lying from bearing plate to support formed in these cases. In B3-0.5-LS70 and B3-0.5-LS70 specimens, many shear cracks rather than one main crack occurred within the shear span and the shear compression failure occurred. The lengths of the shear cracks are smaller due to horizontal stirrups. Similarly with BS3 series, more energy is consumed due to the occurrence of many shear cracks. Therefore, more ductile behavior as well as the increase in load is obtained in beams with horizontal stirrups as shown in Fig. 6.15.
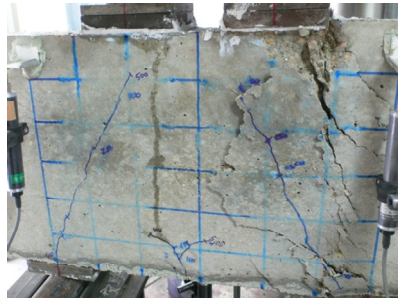
(a) B3-0.5

(b) B3-0.5-VS
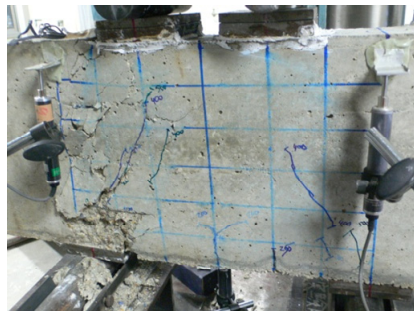
(c) B3-0.5-LS70
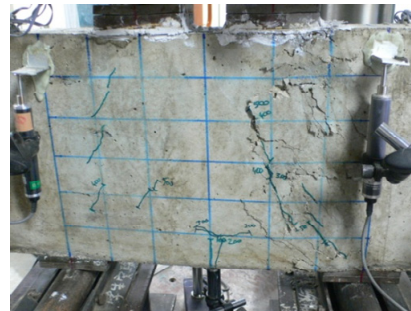
(d) B3-0.5-LS35

Fig. 6.16 Failure of Specimens

The strain values of horizontal stirrups for B3-0.5-LS70 and B3-0.5-LS35 specimens are given in Fig. 6.17 and 6.18 respectively. Strain measurement locations are indicated in Fig. 6.12.

The strain of horizontal stirrups for B3-0.5-LS70 specimen is given in Fig. 6.17. Similarly with BS3-LS70 specimen, the strain values along the beam width are below the yielding strain as seen in the figure. On the other hand, the strain values along the beam surface are larger than that of along the beam width. Moreover, the stirrups yielded at two points (G1 and G2).

The strain of horizontal stirrups for B3-0.5-LS35 specimen is given in Fig. 6.18. Only point G1 at the surface side yielded due to a large volumetric ratio. Moreover, the strain

values along the beam surface are larger than the ones along the beam widths. Therefore, the resistance of the stirrup arm on the surface side against to the spalling of concrete is also confirmed by these results.
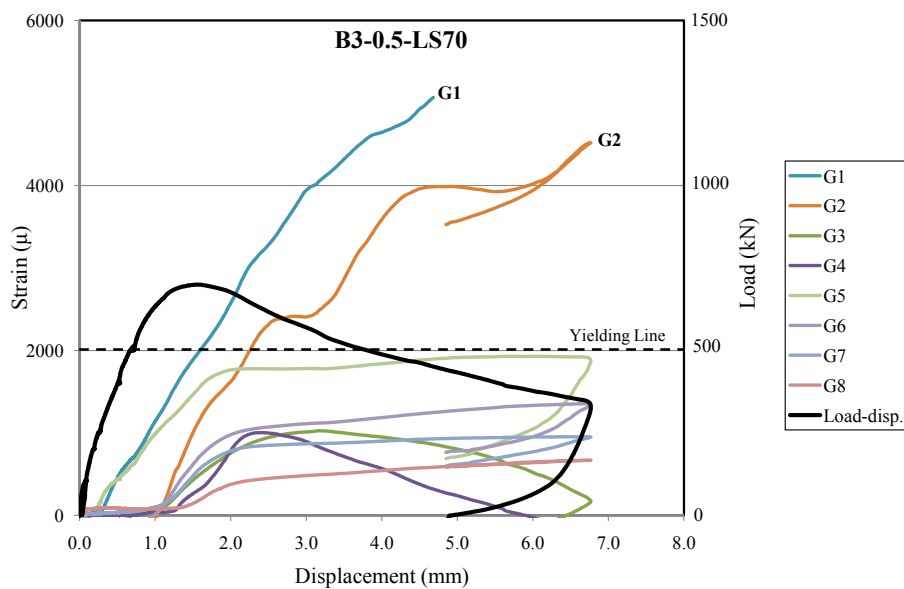
Fig. 6.17 Strain of Horizontal Stirrups (B3-0.5-LS70)
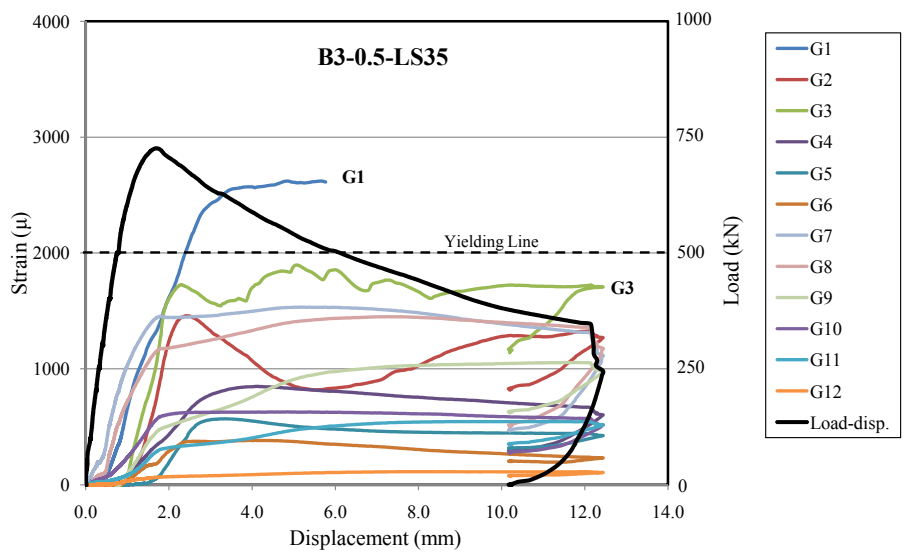
Fig. 6.18 Strain of Horizontal Stirrups (B3-0.5-LS35)

6.3.4 BS3-200 Series

Figure 6.19 shows the comparison of load displacement curves for BS3-200 and BS3-200-LS specimens. The curves were cut since the anchorage failure at the outer ends of the beam occurred in the post-peak region. Therefore, the curves before the anchorage failure are considered in the figure. The peak loads are 1219 kN and 1276 kN for BS3-200 and BS3-200-LS specimens respectively. That is, the arrangement of the horizontal stirrup slightly increases the load carrying capacity. On the other hand, the horizontal stirrup increases the ductility significantly as seen in the figure.
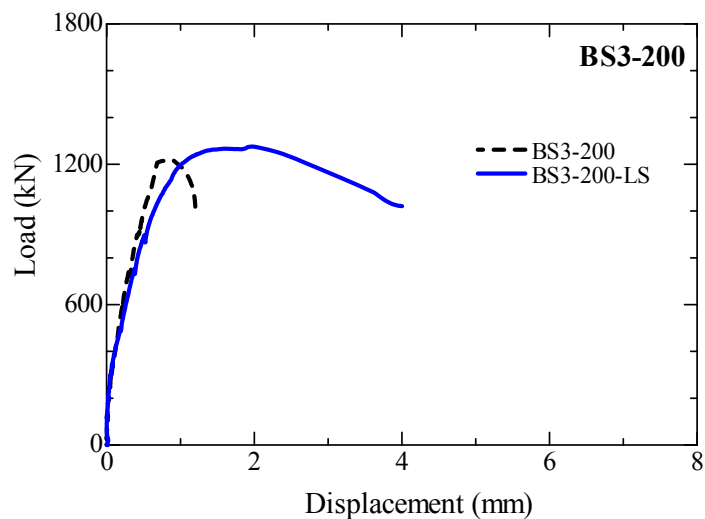
Fig. 6.19 Load-Displacement Curves

Figure 6.20 shows the failure of specimens. In both case, shear compression failure with spalling of concrete occurred. However, the arrangement of the stirrup reduce the spalling of concrete and produce many shear cracks that leads to more ductile behavior in the post-peak region.

(a) BS3-200   (b) BS3-200-LS

Fig. 6.20 Failure of Specimens

Fig. 6.21 shows the strain values of horizontal stirrups for BS3-200-LS specimen. Strain measurement locations are indicated in Fig. 6.12.(a). The strain values along the beam width are very small and none of them yielded as seen in the figure. On the other hand, the strain values along the beam surface are larger than the one along the beam width. Moreover, the stirrups yielded at two points (G1 and G5) while the strain values are close the yielding strain at points G2 and G6 in the post-peak region.
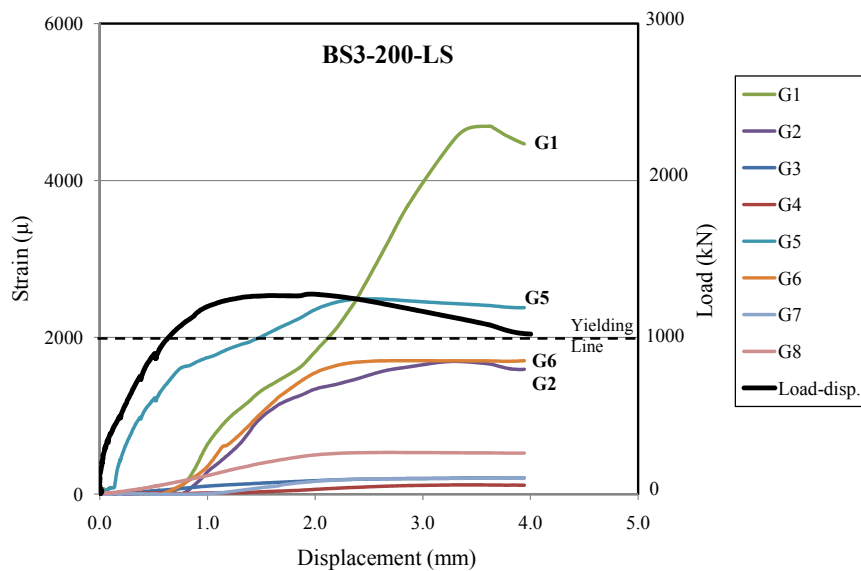
Fig. 6.21 Strain of Horizontal Stirrups (BS3-200-LS)

112

6.3.5 B3-1.0 Series

In order to demonstrate different behavior of deep beams with horizontal stirrup for larger a/d ratio, the beams with a/d=1.0 are investigated and discussed. The experimental load displacement curves for B3-1.0 and B3-1.0-VS and B3-1.0-LS specimens are given in Fig. 6.22. The peak loads are 452 kN, 465 and 452 kN respectively. The results of B3-1.0-LS case shows that, the horizontal stirrup is not effective in the beams with a/d=1.0. Moreover, there is no significant effect of horizontal stirrup on the failure pattern of the specimens as seen in Fig. 6.23.
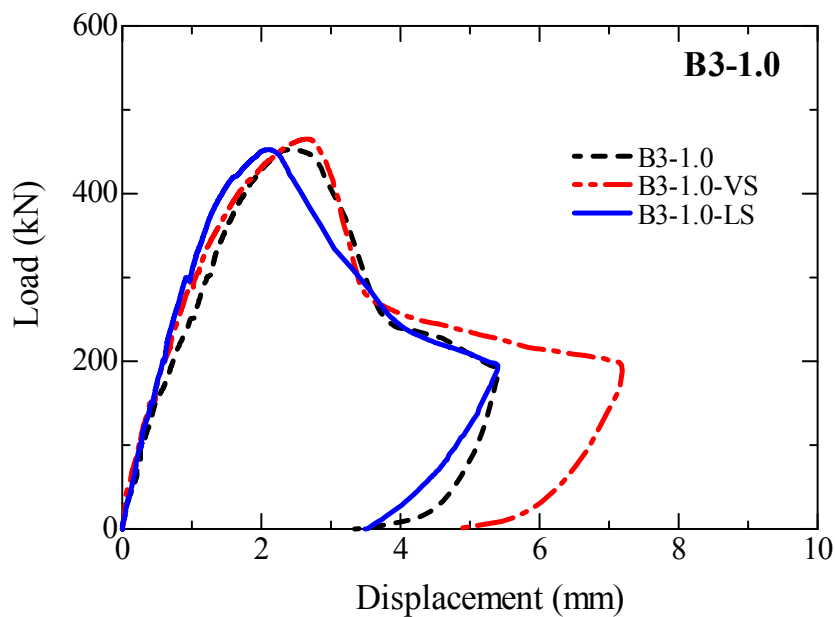
Fig. 6.22 Load-Displacement Curves

(a) B3-1.0

(b) B3-1.0-VS

(c) B3-1.0-LS
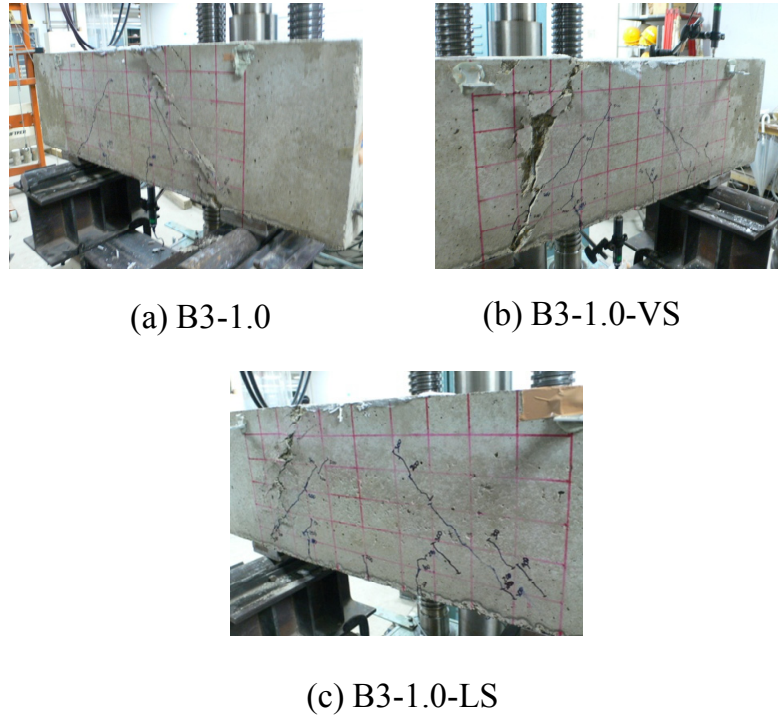
Fig. 6.23 Failure of Specimens

6.4 Applicability of Numerical Results

B3-0.5 and B3-0.5-LS70 specimens are analyzed by 3-D RBSM in order to investigate the effect of horizontal stirrup numerically. The mesh size in the numerical analysis was 20 mm for each case. The numerical results for BS3-200 and B3-1.0 series are also given in Appendix C Figure 6.24 shows the comparison of the experimental and the numerical load-displacement curves for B3-0.5 and B3-0.5-LS70 specimens. A good agreement between the experimental and the numerical results is obtained as demonstrated.

The numerical strain of horizontal stirrups is given in Fig. 6.25. The strain measurement locations for B3-LS70 specimen is shown in Fig. 6.12.(a). The strain values along the beam width (G3, G4, G7 and G8) are indicated in Fig. 6.25.(a) while the strain along the beam surface (G1, G2, G5 and G6) is given in Fig. 6.25.(b). Similarly with the

114

experimental results and BS3 series, the strain values along the beam surface are larger than of the one along the beam width. Therefore, the confinement effect provided by the horizontal stirrup arm along the beam surface direction is also confirmed.
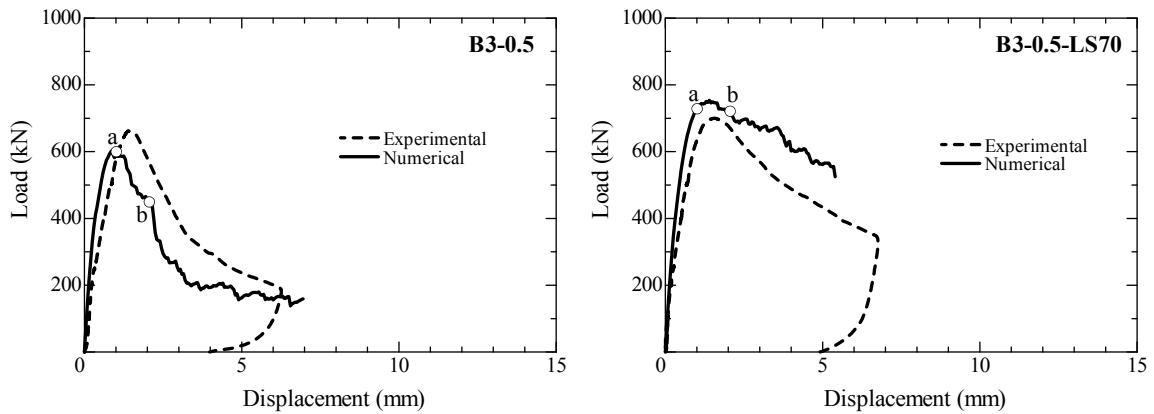
Fig. 6.24 Comparison of Load-Displacement Curves

(a) Along the beam width

(b) Along the beam surface
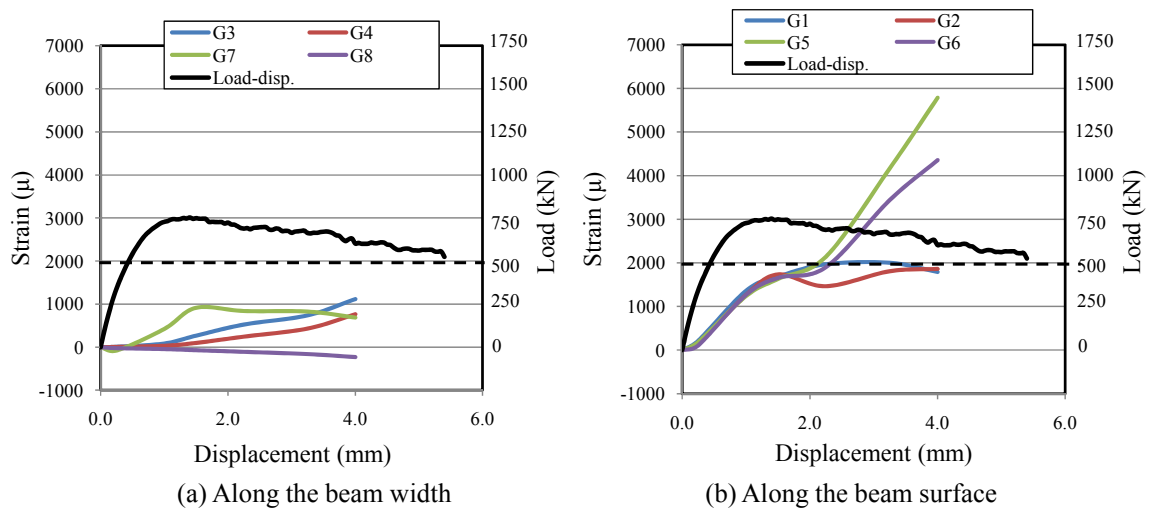
Fig. 6.25 Numerical Strain of Horizontal Stirrups (B3-0.5-LS70)

The comparison of principal stress distribution along the middle longitudinal beam section as well as the stress on the cross-section at the middle of the shear span for B3-0.5

115

and B3-0.5-LS70 specimens is shown in Fig. 6.26. The figures are given at two steps; near the peak load (a) and at a post-peak load (b). The maximum of the stress range is set to 45.0 MPa (1.4*fc'). As seen in the figure, more stress concentration occurs in B3-0.5-LS70 case compared to B3-0.5 specimen.
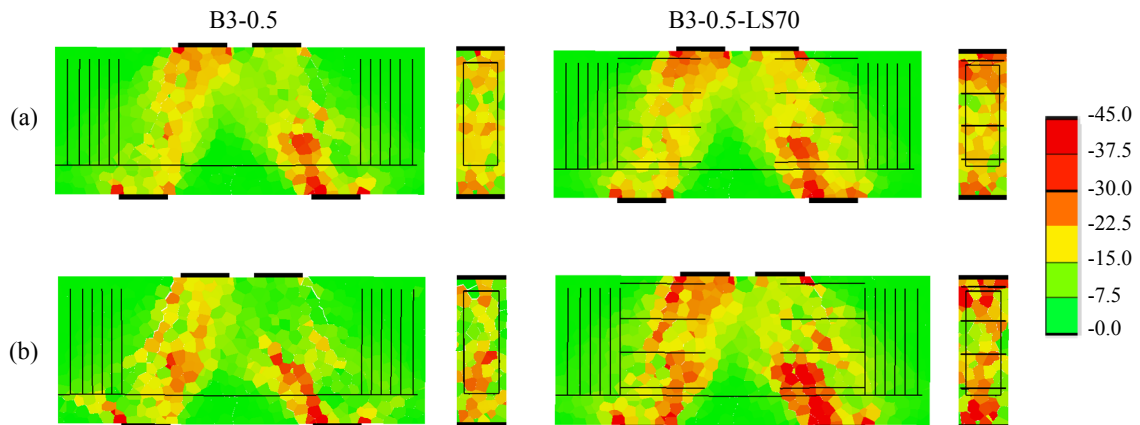
Fig. 6.26 Principal Stress Distribution

The comparison of three-dimensional deformed shapes between B3-0.5 and B3-0.5-LS70 specimens at the post-peak load (b) is shown in Fig. 6.27. A large amount of concrete spalling along the compression struts is observed in B3-0.5 specimen as seen. On the other hand, the spalling of concrete decreases significantly in B3-0.5-LS70 specimen that shows the effectiveness of horizontal stirrup.

(a) B3-0.5

(b) B3-0.5-LS70
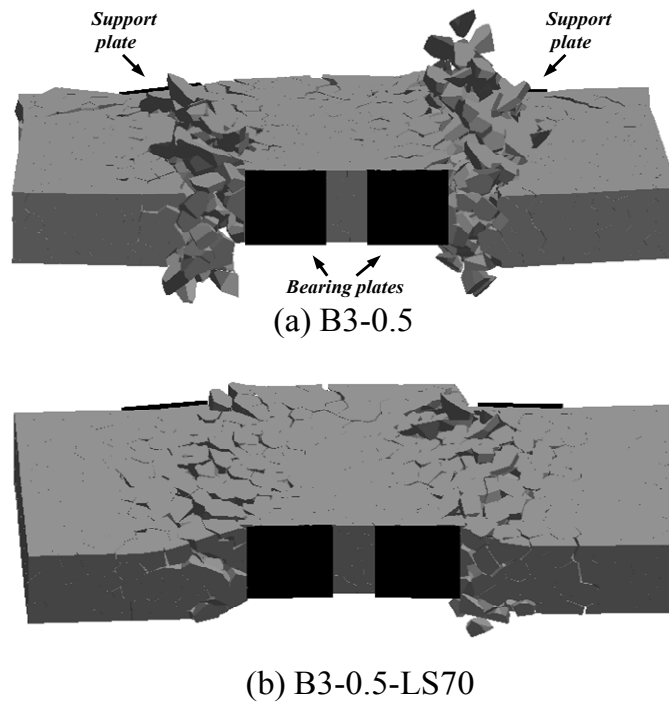
Fig. 6.27 3-D Deformed Shapes

6.5 Effect of Volumetric Ratio on Behavior

In this section, the effect of volumetric ratio on the load carrying capacity as well as the ductility, which is considered by evaluation of energy consumption, in the beams with horizontal stirrup is discussed.

6.5.1 Nominal Shear Strength

Figure 6.28 shows the comparison of nominal shear strength due to volumetric ratio for the series with different sizes. In the JSCE code (JSCE 2002), the design compressive capacity V_{wcd} of web concrete in resisting applied shear forces is calculated as given in Eq. [6.1]. That is, compressive capacity depends on the beam width (b), the effective depth (d) and square root of compressive strength of concrete (f_c'). Therefore, the nominal shear strength used here is given in Eq. [6.2], which is calculated in similar way with Eq. [6.1].

$$V_{wcd} = f_{wcd} \cdot b_w \cdot d / \gamma_b \qquad \qquad [6.1]$$

where $f_{wcd} = 1.25\sqrt{f'_{cd}}$ (N/mm^2) and γ_b is the member factor.

$$V_{nominal} = V/(b.d.\sqrt{f'_c}) \qquad \qquad [6.2]$$

As seen in the Fig. 6.28, the increase in load is observed by increase of volumetric ratio. Moreover, the increment rate of strength due to volumetric ratio is mostly similar for all series. Therefore, the increase of volumetric ratio leads to ascend of nominal strength and load carrying capacity.
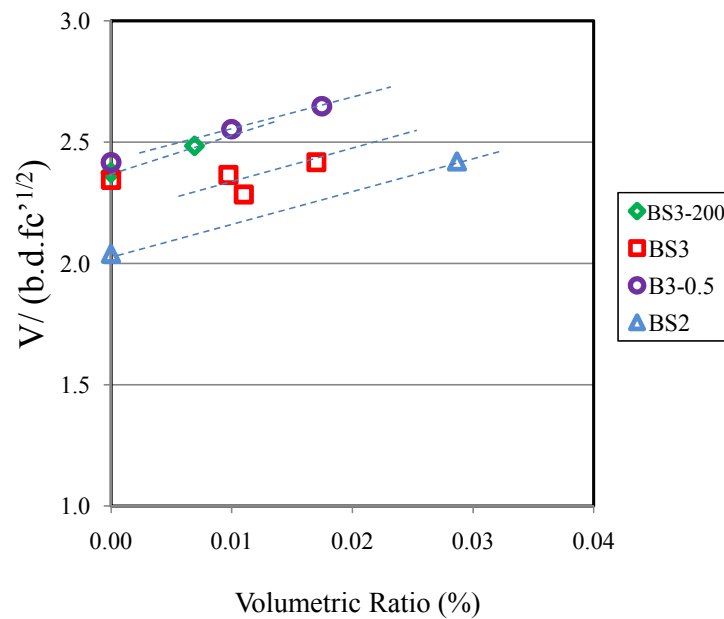
Fig. 6.28 Nominal Shear Strength-Volumetric Ratio

6.5.2 Energy Consumption

In order to investigate the effect of horizontal stirrup on the ductility, the energy consumption of the beams is compared. To achieve that, the area under the load displacement curves is calculated for each beam up to the post-peak load of $0.85.P_{peak}$ as demonstrated in

118

Fig. 6.29. Then, the energy (E) is normalized by the beam width (b), effective depth (d), shear span (a) and square root of compressive strength of concrete (f_c'). Moreover, the energy consumption for each series including a discussion on the energy of pre-peak and the post-peak region separately is given in Appendix D.
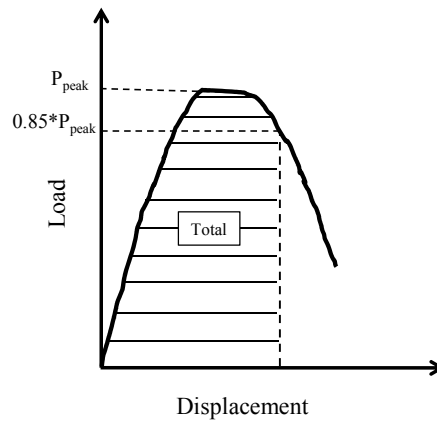
Fig. 6.29 Calculation Method for Energy Consumption

The comparison of energy consumption due to volumetric ratio for the series with different sizes is given in Fig. 6.30. A significant increase in energy is observed by increase of volumetric ratio. In one point in BS3 series, which belongs to BS3-LS70-h specimen, the energy consumption is lower than the one in BS3-LS70 case in spite of the volumetric ratio is slightly higher than BS3-LS70 case. The reason is that, since the horizontal stirrups are divided into two loops by means of reinforcement with hooks at each ends (see Fig. 6.2), the hooks caused the increase of cover thickness that led to the decrease of confined concrete area within the horizontal stirrups. Therefore, a less confinement effect could be provided.
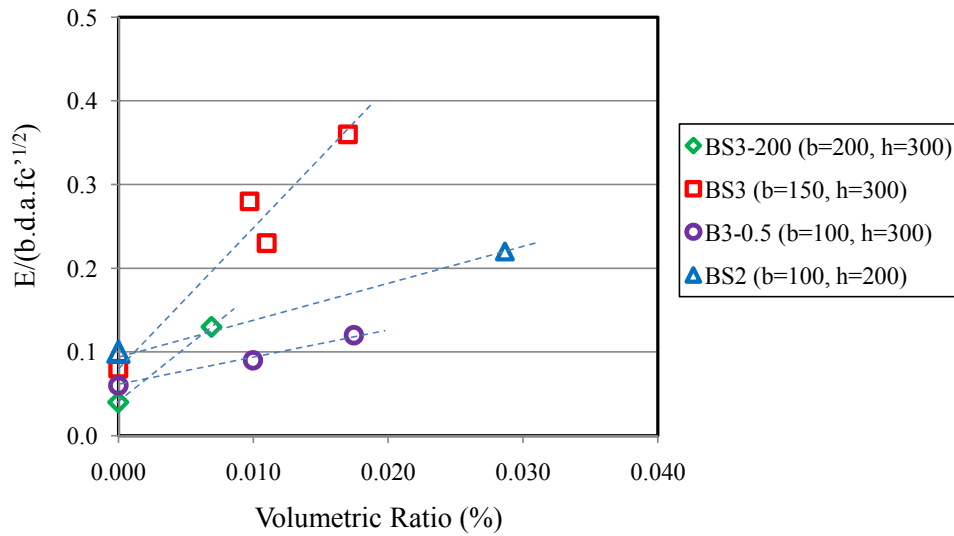
Fig. 6.30 Energy-Volumetric ratio

6.6 Effect of Size and Shape on Behavior

6.6.1 Size Effect

6.6.1.1 Nominal Shear Strength

Figure 6.31 shows the comparison of nominal shear strength due to specimen size, in order to investigate the size dependency of horizontal stirrup arrangement on the load carrying capacity.

The horizontal stirrup cases are compared between BS2 (100x200 mm) and BS3 (150x300 mm) series, where the size of BS3 is 1.5 times of BS2 series. As seen in the figure, the strength in the smaller specimen shows some increase while the increase in larger size case is limited by increasing volumetric ratio. However, it should be kept in mind; the volumetric ratio in the smaller case is higher than the ones in larger size specimens. Therefore, it can be concluded that the size effect on nominal shear strength and load capacity is not dominant.
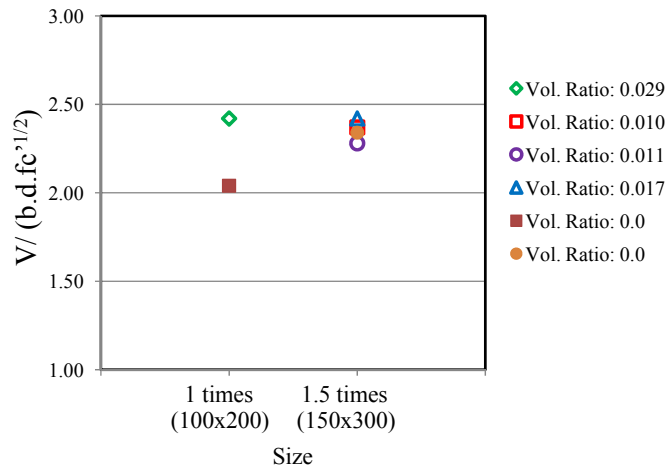
Fig. 6.31 Nominal Shear Strength-Size

6.6.1.2 Energy Consumption

The comparison of energy due to specimen size is shown in Fig. 6.32, in order to investigate the size dependency of horizontal stirrup arrangement on the ductility. As seen in the figure, the horizontal stirrup provides significantly higher ductility in larger size specimens although the volumetric ratios are smaller in the larger size cases. That is the effect of horizontal stirrup on the ductility increases significantly by increase of the size of the specimens.
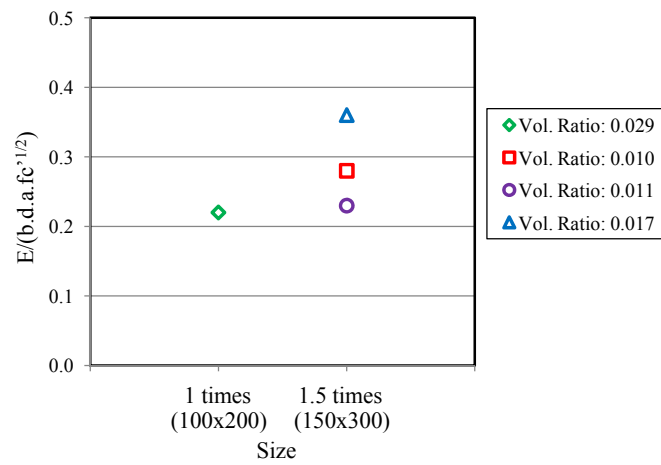
Fig. 6.32 Energy-Size

6.6.2 Effect of Beam Width

6.6.2.1 Nominal Shear Strength

In this section, the effect of horizontal stirrup on nominal shear strength due to the beam width is investigated. In order to achieve that, the nominal strength of the specimens with different beam width while having the same volumetric ratios is compared.

The comparison of nominal strength between B3-0.5-LS70 and BS3-LS70 specimens, which have the same volumetric ratio of 0.010 and the same effective depth *(d)* of 240 mm is shown in Fig. 6.33. The nominal shear strength in the control beams (Vol. ratio: 0.0) are also given in the figure. The beam widths are 100 mm and 150 mm for B3-0.5-LS70 and BS3-LS70 specimens respectively. That is, only the beam widths are different. As seen in the figure, there is no significant difference between the smaller and larger width cases.

Figure 6.34 shows the comparison of nominal strength between B3-0.5-LS35 and BS3-LS35 specimens, which have the same volumetric ratio of 0.017 and the same effective depth *(d)* of 240 mm while the beam widths are also different (100 mm and 150 mm). Similarly with the previous case, the effect of beam width on nominal strength and load carrying capacity is not significant.
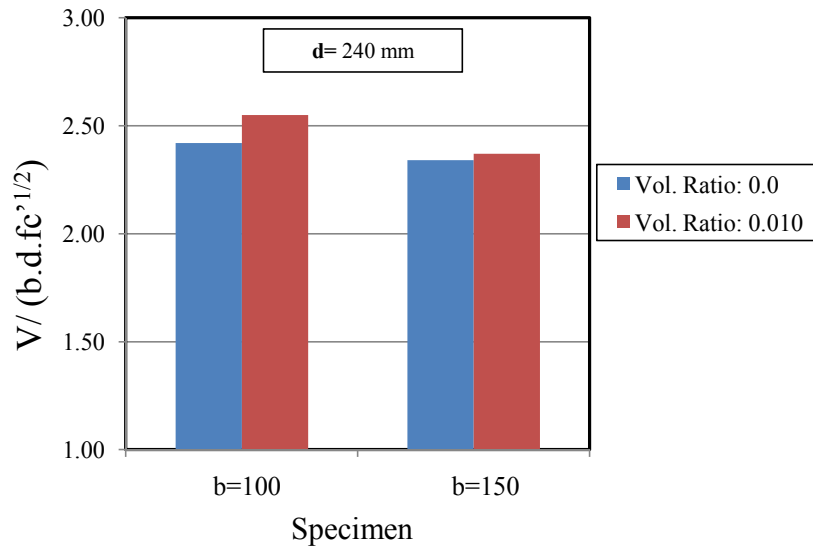
Fig. 6.33 Effect of Beam Width on Nominal Shear (d=240 mm; Vol. ratio: 0.010)
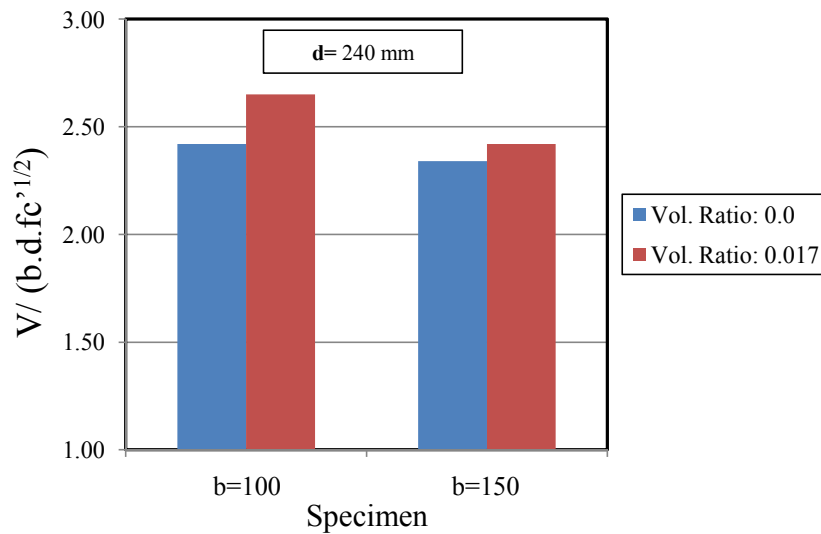
Fig. 6.34 Effect of Beam Width on Nominal Shear (d=240 mm; Vol. ratio: 0.017)

6.6.2.2 Energy Consumption

The change of ductility provided by horizontal stirrup due to the beam width is investigated. In order to achieve that, the energy consumption of the specimens with different beam width while having the same volumetric ratios is compared.

123

The comparison of energy consumption between B3-0.5-LS70 and BS3-LS70 specimens, which have the same volumetric ratio of 0.010 and the same depth of 240 mm, is shown in Fig. 6.35. As seen in the figure the energy consumption increase about 3 times in the case of the specimen with b=150 mm. That is, the effectiveness of the horizontal stirrup increases significantly by increase of the beam width of the specimen.
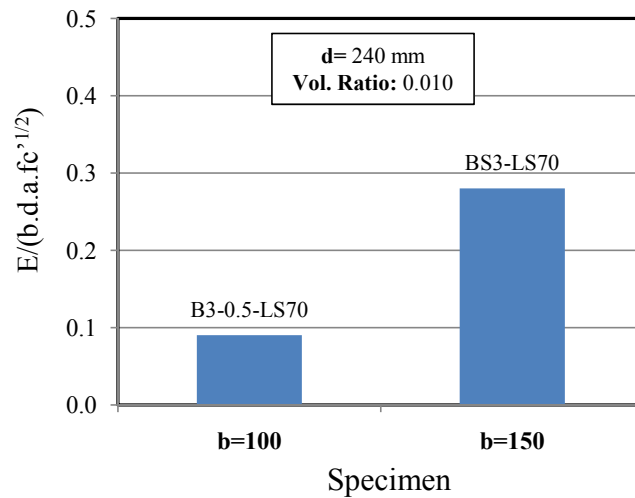
Fig. 6.35 Effect of Beam Width on Ductility (d=240 mm; Vol. ratio: 0.010)

Figure 6.36 shows the comparison of energy consumption between B3-0.5-LS35 and BS3-LS35 specimens, which have the same volumetric ratio of 0.017 and the same depth of 240 mm. Similarly with the previous case, the energy consumption increases about 3 times in the case of the specimen with b=150 mm. This means that, the horizontal stirrup is more effective in the beams with larger widths while the other parameters and dimensions are the same.
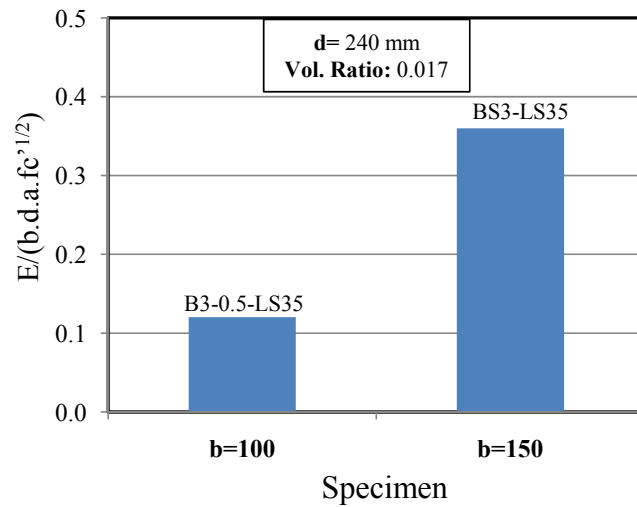
Fig. 6.36 Effect of Beam Width on Ductility (d=240 mm; Vol. ratio: 0.017)

6.7 Summary and Conclusion

In this chapter, a new horizontal stirrup arrangement is proposed for short deep beams by considering three-dimensional effects. In order to investigate the proposed model, four series of deep beams with a/d=0.5 and one series of deep beam with a/d=1.0 are tested and also analyzed. The load displacement curves, crack patterns, strain of horizontal stirrups, strength distributions of the beams as well as 3-D deformed shapes are investigated in detail. It is shown that, the horizontal stirrup provides a significant increase of ductility of a short deep beam as well as the load carrying capacity by confinement effect of horizontal stirrups.

The increase of volumetric ratio enhances the nominal shear strength that is load carrying capacity. On the other hand, the investigation of size effect on the strength shows that the specimen with smaller size shows some increase in the strength by increasing volumetric ratio while the increase in larger size case is limited. However, it should be kept in mind; the volumetric ratio in the smaller case is higher than the ones in larger size specimens. Moreover, it is difficult to understand the size effect from only these specimens

125

since the dimensions are limited, where the dimension of larger size specimens is 1.5 times of the smaller size. However, as a general comment, it can be concluded that the size effect on nominal shear strength is not dominant based on available results.

On the other hand, the effect of horizontal stirrup on the ductility of the beams increases significantly by increase of the size of the beams as well as the beam width (b). Moreover, the increase of volumetric ratio leads to more energy consumption and therefore more ductile behavior is observed in the beams with larger volumetric ratio.

7. Summary and Conclusions

7.1 Conclusions

The main purpose of this study is to evaluate the shear failure mechanism of deep beams. Firstly, the numerical tool, which is 3D RBSM, is introduced. Then the applicability of 3D RBSM on deep beams is verified. The effect of stirrup in deep beams in terms of load carrying capacity and shear failure mechanism is investigated. Afterwards, 3D effects as well as the size and shape effect in short deep beams are presented. Finally, a new horizontal stirrup arrangement for short deep beams is proposed. The conclusions are given as the fallows.

1) In order to verify the applicability of 3-D RBSM on deep beams, a series of beam having a/d=0.5 to 2.0 are tested and analyzed. The numerical and the experimental results are compared in terms of the load-displacement curves, crack pattern and strain of stirrups. A good agreement is demonstrated. It is confirmed that, 3-D RBSM can simulate the local and micro behavior as well as the macro behavior. Therefore, the applicability of 3D RBSM on deep beams is confirmed.

2) The shear failure mechanism and load carrying capacity of deep beams are clarified by investigating the numerical results of load-displacement curves, crack pattern, 3-D deformed shapes, strut behavior and stress distribution and crack widths as well as the strain of stirrups. Therefore, the beams are classified into three regions based on the effect of stirrup.

2.1   Region 1 includes the beams with a/d=0.5, in which 3-D effects and lateral deformation is dominant on the shear strength. No effect of stirrups along the vertical direction is observed. Confinement effect provided by stirrups leads to the increase in load. In this case, the entire member is considered as a single the D-region where the strut action is dominant on the behavior.

2.2   In region 3, the slender beams having a/d=3.0 are included. The occurrence of compression chords and compression diagonals, which agrees with truss analogy, due to stirrup is clarified by comparing the stress distribution between with and without stirrup cases. The B and D-regions occur separately in this region that agrees with ACI 318-0.5 code for slender beams. It is confirmed that the shear strength V can be obtained by sum up Vs and Vc.

2.3   In region 2, the beams with a/d=1.0, 1.5 and 2.0 are included. The stirrup is effective along vertical direction in this region. In a/d=1.0 case, the lateral deformation is also observed, however it is smaller compared to a/d=0.5 case. The stirrup effect is limited in this case. The strut action is dominant on the behavior and the entire member should be considered as a single D region. On the other hand, the stirrup is significantly effective in a/d=1.5 and 2.0 cases. The load as well as the

ductility increase significantly due to an arrangement of stirrup. The occurrence of compression chords and compression diagonals due to stirrup is also observed in this case from stress figures. That is, the truss analogy is effective on the behavior of beams with stirrup. The load carrying mechanism is based on both strut action and truss effect provided by stirrup. Moreover, truss analogy is more dominant on the behavior rather than the strut action. As a result, the B and the D-regions are superposed in a/d=1.5 and 2.0 cases. This result is different from ACI 318-0.5 Code, in which the entire member is taken into consideration as a single D-region for deep beams with a_v/h less than 2.0.

3) The effect of 3-D behavior on the strength and ductility for deep beams having a/d=0.5 and without stirrup are clarified experimentally and numerically.

3.1   The evaluation of experimental results shows that, more ductile behavior is observed due to the increase in beam width. The reason is that, the core concrete width is limited after spalling on the surface in smaller width case and the increase of confinement effect of the core concrete in larger width cases is observed.

3.2   The numerical results are also confirmed the effect of 3-D behavior. It is shown that, the spalling of concrete on the surface, and the confinement effects in the middle section is significant. Moreover, it is numerically confirmed that the 3-D behavior is influenced to the strength and ductility depending on the width.

4) By considering three-dimensional effects in short deep beams, a new horizontal stirrup method is proposed. The effectiveness of the proposed model is verified by several experimental results as well as the analyses.

4.1   It is shown that, the horizontal stirrup increases the ductility significantly as well as the load carrying capacity by confinement effect provided by horizontal stirrups.

4.2   The nominal shear stress, or the load carrying capacity, enhances by increase of the volumetric ratio of the beams. In the beams with horizontal stirrups, there is no significant effect of size and shape resulting from the beam width on load carrying capacity. This means that, the size and shape effect is not dominant on load capacity in the case of deep beams with horizontal stirrup.

4.3   The ductility of beams with horizontal stirrup, which is measured based upon energy consumption, increases significantly by increase of the specimen size and by increase of the beam width.

4.4   Energy consumption in the beams with horizontal stirrup enhances significantly by increase of the volumetric ratio. Therefore, a significant improvement on the ductility of beams is provided by confinement effect of horizontal stirrups.

7.2 Recommendations for Future Study

In this study, the shear failure mechanism and load carrying capacity of deep beams with stirrup were clarified by several experimental and numerical results. Therefore, the shear behavior of RC deep beams was understood. However, the range of investigated specimens is limited. For future study, numerical and experimental results on deep beams should be extended including the beams with various parameters such as specimen size, width and depth, stirrup ratio, the strength of reinforcement as well as the compressive

strength of concrete and so on. Therefore, a new design method to evaluate the shear strength of RC deep beams should be proposed based on the results obtained from this study.

A new horizontal stirrup arrangement based on several experimental and numerical results of beams with horizontal stirrups is proposed in this study. The effect of volumetric ratio and size as well as the shape on the beams with horizontal stirrups is clarified. For future study, equations to evaluate the ductility and the shear strength of short deep beams with horizontal stirrup should be proposed. To achieve that, the experimental and the numerical results are extended including various specimens with different parameters such as size and volumetric ratio, of which effects on the behavior are discussed in this study.

References

ASCE-ACI Committee 445, (1998). "Recent approach to shear design of structural concrete." Journal of Structural Engineering 124(12), 1375–1417.

ACI Committee 318, (2005). "Building code requirements for structural concrete (ACI 318-05) and commentary (ACI 318R-05)". Farmington Hills (MI): American Concrete Institute.

Ashour, A.F., (2000). "Shear capacity of reinforced concrete deep beams." Journal of Structural Engineering, ASCE, 126, 1045–1052.

Ashour, A.F., Alvarez, L.F. and Toropov, V.V., (2003). "Empirical modelling of shear strength of RC deep beams by genetic programming." Computers and Structures, 81(5),331–338.

Averbuch, D. and de Buhan, P., (1999). "Shear design of reinforced concrete deep beams: a numerical approach." Journal of Structural Engineering, ASCE, 125(3), 309-318.

Bazant, Z.P., (1986). "Mechanics of distributed cracking." Appl Mech Rev, ASME, 39(5), 675–705.

Bazant, Z.P. and Pijaudier-Cabot, G., (1988). "Nonlocal continuum damage, localization instability and convergence." J. Appl. Mech, 55, 287–293.

Bazant, Z.P., (1976). "Instability, ductility, and size effect in strain softening solids." J Engng Mech Div, ASCE, 102: 331–344.

Bolander, J.E., Shiraishi, T. and Isogawa, Y., (1996). "An adaptive procedure for fracture simulation in extensive lattice networks." Engineering Fracture Mechanics, 54, 325-34.

Bazant, Z.P. and Kazemi, M.T., (1991). "Size effect on diagonal shear failure of beams without stirrups." ACI Structural Journal, 88(3), 268-276.

Bolander, J.E., Hong, G.S. and Yoshitake, K., (2000). "Structural concrete analysis using Rigid-Body-Spring Networks." Computer-Aided Civil and Infrastructure Engineering, 15, 120-133.

Bolander, J.E. and Hong G.S., (2002). "Rigid-Body-Spring Network modeling of prestressed concrete members." ACI Structural Journal, 99 (5), 595-604.

Comite Euro-International du Beton, (1990). "CEB-FIB model code 1990 first draft." CEB, Paris.

JSCE, (2002). "The Standard Specifications for Concrete Structures." Tokyo: Japan Society of Civil Engineers.

JSCE, (2007). "Standard Specifications for Concrete Structures." Tokyo: Japan Society of Civil Engineers. [In Japanese].

Kuo, W.W., Cheng, T.J. and Hwang, S.J., (2010). "Force transfer mechanism and shear strength of reinforced concrete beams." Engineering Structures, 32, 1537-1546.

Kawai, T., (1978). "New discrete models and their application to seismic response analysis of structures." Nuclear Engineering and Design, 48, 207-229.

Kostovos, M.D. and Newman, J.B., (1978). "Generalized stress-strain relations for concrete model." Journal of Engineering Mechanics, ASCE, 125,845-856.

Kotsovos, M.D. and Pavlovic, M.N., (2004). "Size effects in beams with small shear span-to-depth ratios." Computers&Structures, 82, 143-156.

Kosa, K., Umemoto, Y., Nishioka, T. and Kobayashi, H., (2005). "Experimental studies on failure mode in the deep Beam." Journal of Structural Engineering, JSCE 51A,1283-1290. [In Japanese].

Kosa, K., Wakiyama, T., Nishioka, T. and Kobayashi, H., (2006). "Effect of shear span ratio on the fracture of deep beams." Doboku Gakkai Ronbunshuu E, 62(4), 798-814. [In Japanese].

Mau, S.T. and Hsu T.T.C., (1989). "Formula for the shear strength of deep beams." ACI Structural Journal, 86(5), 516–523.

Mazars, J. and Pijaudier-Cabot, G., (1986). "Continuum damage theory: Application to concrete." Internal Report 71, LMT, Cachan.

Meguro, K. and Hakuno, M., (1989). "Fracture analysis of concrete structures by the modified distinct element method." Structural Engineering/Earthquake Engineering, 6(2), 283–294.

MacGregor, J.G., (1997). "Reinforced concrete: mechanics and design." (3rd ed.), Prentice Hall, Upper Saddle River, NJ.

Mau, S. and Hsu, T.T.C., (1987). "Shear strength prediction for deep beams with web reinforcement." ACI Structural Journal, 84, 513–523.

Mörsch, E., (1920). "Der eisenbetonbau-seine theorie und anwendung (Reinforced concrete construction – Theory and application)." 5th Ed., Wittwer, Stuttgart, Vol. 1, Part 1.

Mörsch, E., (1922). "Der eisenbetonbau-seine theorie und anwendung (Reinforced concrete construction – Theory and application)." 5th Ed.,Wittwer, Stuttgart, Vol. 1, Part 2

Niwa, J., (1983). "Equation for shear strength of reinforced concrete deep beams based on FEM analysis." Proceedings of JCI 2nd Colloquium on Shear Analysis of RC Structures, 119-126.

Nagai, K., Sato, Y. and Ueda, T., (2005). "Mesoscopic Simulation of Failure of Mortar and Concrete by 3D RBSM." Journal of Advanced Concrete Technology, JCI, 3(3), 385-402.

Ritter W (1899). "Die Bauweise Hennebique. Schweizerische Bauzeitung." **33**, 59–61.

Rogowsky, D.M., MacGregor, J.G. and Ong, S.Y., (1986). "Test of reinforced concrete deep beams." ACI Structural Journal, 83, 614–623.

Smith, K.N. and Vantsiotis, A.S., (1982). "Shear strength of deep beams." ACI Structural Joutnal, 79, 201–213.

Schlaich, J., Schäfer, K. and Jennewein, M., (1987). "Toward a Consistent Design of Structural Concrete", PCI Journal, Special Report, 32(3).

Sanad, A. and Saka, M.P., (2001). "Prediction of ultimate shear strength of reinforced-concrete deep beams using neural networks." Journal of Structural Engineering, ASCE, 127 (7), 818–828.

Salamy, M.R., Kobayashi, H. and Unjoh, S., (2005). "Experimental and analytical study on RC deep beams." Asian Journal of Civil Engineering (Building and Housing), 6(5), 409-421.

Saito, S. and Hikosaka, H., (1999). "Numerical analysis of reinforced concrete structures using spring network model." Journal of Materials, Concrete Structures and Pavements, JSCE, No.627/V-44, 289-303.

Saito, S., (1999). "Fracture analyses of structural concrete using spring networks with random geometry." PhD thesis, Fukuoka, Kyushu University.

Suga, M., Nakamura, H., Higai, T. and Saito, S., (2001). "Effect of bond properties on the mechanical behavior of RC beam." Proceedings of Japan Concrete Institute, 23(3), 295-300.

Shi, G.H. and Goodman, R.E., (1989). "Generalization of two-dimensional discontinuous deformation analysis for forward modelling." International Journal for Numerical and Analytical Methods in Geomechanics, 13, 359–380.

Schlangen, E., (1993). "Experimental and numerical analysis of fracture process in concrete." Ph.D Thesis, Delft University of Technology, Netherlands.

Schlangen, E. and van Mier J.G.M., (1992). "Experimental and numerical analysis of micromechanisms of fracture of cement-based composites." Cement & Concrete Composites, 14, 105–118.

Tan, K.H., Kong, F.K., Teng, S. and Weng, L.W., (1997). "Effect of web reinforcement on high strength concrete deep beams." ACI Structural Journal, 94(5), 572–582.

Tan, K.H. and Cheng, G.H., (2006). "Size effect on shear strength of deep beams: investigating with strut-and-tie model." Journal of Structural Engineering, ASCE, 132(5), 673-685.

Tanimura, Y., Sato, T., Watanebe, T. and Matsuoka, S., (2004). "Shear Strength of Deep Beams with Stirrups." Journal of Materials, Concrete Structures and Pavements, 2004-05 NO.760 V-63. [In Japanese].

Tan, K.H. and Lu, H.Y., (1999). "Shear behavior of large reinforced concrete deep beams and code comparisons." ACI Structural Journal, 96 (5), 836–845.

Tang, C.Y. and Tan, K.H., (2004). "Interactive mechanical model for shear strength of deep beams." Journal of Structural Engineering, ASCE, 130 (10), 1534–1544.

Van Mier, J.G.M., (1997). "Fracture Processes of Concrete: Assessment of Material Parameters for FractureModels." CRC Press, Inc, Boca Raton, Florida.

Walraven, J. and Lehwalter, N., (1994). "Size effects in short beams loaded in shear." ACI Structural Journal, 91(5), 585-593.

Wang, W., Jiang, D. and Hsu, C.T., (1993). "Shear strength of reinforced concrete deep beams." Journal of Structural Engineering, ASCE, 119 (8), 2294–2312.

Yamamoto, Y., Nakamura, H., Kuroda, I. and Furuya, N., (2008). "Analysis of compression failure of concrete by three-dimensional Rigid Body Spring Model." Doboku Gakkai Ronbunshuu, 64(4), 612-630. [In Japanese].

Yamamoto, Y., (2010). "Evaluation of failure behaviors under static and dynamic loadings of concrete members with mesoscopic scale modeling." PhD thesis, Nagoya University, Nagoya. [In Japanese].

Yang, K.H., Chung, H.S., Lee, E.T. and Eun, H.C., (2003). "Shear characteristics of high-strength concrete deep beams without shear reinforcements." Engineering Structures, 25 (10), 1343–1352.

Zararis, P.D., (2003). "Shear compression failure in reinforced concrete deep beams." Journal of Structural Engineering, ASCE, 129 (4), 544–553.

Zhang, N. and Tan, K.H., (2007). "Size effect in RC deep beams: Experimental investigation and STM verification." Engineering Structures, 29, 3241-3254.

Appendix A

SHEAR STRENGTH DESIGN

The conventional way to evaluate the shear strength of RC beams is to add up a concrete contribution (Vc) and a stirrup contribution (Vs) calculated by truss model, which is a basic tool for analysis and design of RC concrete beams. Truss models were first proposed by Ritter (1899) and then Mörsch (1920,1922) applied the truss models on torsion. In 1987, strut-and-tie models (STM) approach, which is extended from truss models for beams and it is particularly convenient for deep beams, was introduced by Schlaich et al. (1987). In that work, the concept of the B and the D-regions was introduced, where B implies beam or Bernoulli, in which plane sections remain plane, and D means discontinuity or disturbed regions, in which the assumption of the plane sections remain plane is inappropriate (ASCE-ACI Committee 445 1998). That is, a linear strain distribution forms in B regions where the strain distribution is nonlinear in D regions. The whole member becomes D region when a/d ratio is small. In particular, STM is convenient for the design of D region that has a complex internal stress state (ASCE-ACI Committee 445 1998).

ACI 318-0.5 Code (ACI 2005) describes deep and slender beams based on the shear span to height ratio (a_v/h) as shown in Fig. A.1. The occurrence of the B and the D-regions in deep and slender beams are described. Figure A.1.(a) shows the description of a deep beam where a_v/h is less than 2.0. In this case, the entire member is considered as a single the D-region. The limit state for a deep beam is shown in Fig. A.1.(b). The limit shear span to height ratio (a_v/h) is equal to 2.0. The minimum inclination angle of a strut is given as 25 degree. The entire member is also considered as a single the D-region in this case. Strut and tie models

(STM) can be used for the design of the D regions. Figure A.1.(c) shows the description of a slender beam where the shear span to height ratio (a_v/h) is greater than 2.0. In this case, the B-regions also form near the shear span as well as the D-regions formation near the loading and support points. According to the ACI 318-0.5 Code (ACI 2005), the shear strength of a slender beam is calculated by the sum of the shear strength provided by concrete (Vc) and the shear strength provided by shear reinforcement (Vs) as given in Eq. [A.1].

(a) Deep beam, shear span $a_v < 2h$

θ : Min. of 25 deg.
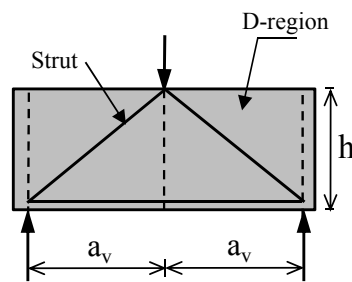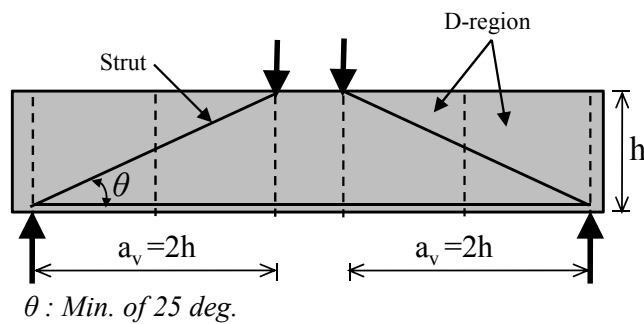
(b) Limit for a deep beam, shear span $a_v = 2h$
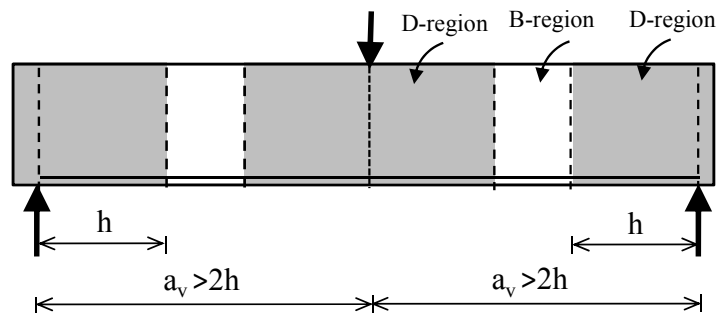
(c) Slender beam, shear span $a_v > 2h$

Fig. A.1 Description of Deep and Slender Beams in ACI 318-0.5 Code (ACI 2005)

$$V_{ACI\,318-05} = V_C + V_S \qquad\qquad [A.1]$$

$$V_C = \frac{1}{6}\sqrt{f_c'}\,b_w d \qquad [N] \qquad\qquad [A.1.a]$$

$$V_S = A_v f_{yt} \frac{d}{s} \leq \frac{4}{6}\sqrt{f_c'}\,b_w d \quad [N] \qquad\qquad [A.1.b]$$

where;

$V_{ACI\,318-05}$	: Nominal shear strength for slender beams
V_C	: Nominal shear strength provided by concrete
V_C	: Nominal shear strength provided by shear reinforcement
f_c'	: Compressive strength of concrete
b_w	: Beam web width
d	: Effective depth (mm)
A_v	: Shear reinforcement area within a spacing *s*
f_{yt}	: Yield strength of transverse reinforcement
s	: Spacing of shear reinforcement

On the other hand, a method to calculate the shear strength of deep beams is given by Eq. [A.2] in The Standard Specifications for Concrete Structures (JSCE 2002). In this method, stirrup contribution is calculated based on truss analogy and then the calculated value is reduced depending on a/d ratio. That is, the stirrup effect decreases for smaller a/d ratio. However, in the JSCE's 2007 Standard Specifications for Concrete Structures (JSCE 2007), the previous method was revised based on the experimental results. The new method is given in Eq. [A.3], in which the effect of stirrup is considered by the increase of concrete

contribution. The effect of stirrup increase by increase of the parameters of stirrup ratio (p_{wb}) and shear span to depth ratio (a_v /d).

$$V_{ydd}= V_{cdd} + V_{sdd} \qquad \text{[A.2]}$$

$$V_{cdd} = \beta_d .\beta_p .\beta_a .f_{dd} .b_w.d /\gamma_b \qquad \text{[A.2.a]}$$

$$f_{dd}=0.19\sqrt{f'_{cd}} , \ (N/mm^2) \qquad \text{[A.2.b]}$$

$$\beta_d=\sqrt[4]{1000/d} \qquad \text{when } \beta_d>1.5, \ \beta_d \text{ shall be } 1.5 \qquad \text{[A.2.c]}$$

$$\beta_p=\sqrt[3]{100p_w} , \qquad \text{when } \beta_p>1.5, \ \beta_p \text{ shall be } 1.5 \qquad \text{[A.2.d]}$$

$$\beta_a= \frac{5}{1+\left(\frac{a_v}{d}\right)^2} \qquad \text{[A.2.e]}$$

$$V_{sdd}= \varphi. V_{sd} \qquad \text{[A.2.f]}$$

$$\varphi=-0.17+0.3(a_v /d)+0.33/p_{wb} \le 1.0 \qquad \text{[A.2.g]}$$

$$V_{sd}=[A_w f_{wyd}(\sin\alpha_s+\cos\alpha_s)/s_s+ A_{pw}\sigma_{pw}(\sin\alpha_p+\cos\alpha_p)/s_p]z/\gamma_b \qquad \text{[A.2.h]}$$

where;

V_{ydd} : Design Shear Capacity

γ_b : It shall be 1.3 in generally

f'_{cd} : Design compressive strength of concrete (N/mm^2)

p_w : Longitudinal tension reinforcement ratio (%)

a_v : Shear Span

d : Effective depth (mm)

V_{sdd} : Design shear strength of shear reinforcement in accordance with Eq. [A.2.f]

V_{sd} : Contribution of shear strength computed with Eq [A.2.h] as in JSCE 2002

p_{wb} : Shear reinforcement ratio (%)

$$V_{cdd} = (\beta_d + \beta_w).\beta_p.\beta_a.f_{dd}.b_w.d / \gamma_b \qquad\qquad [A.3]$$

$$\beta_w = 4.2\sqrt[3]{100p_{wb}}.(a_v/d\text{-}0.75)/\sqrt{f_{cd}} \qquad\qquad [A.3.a]$$

$$\beta_p = \frac{1+\sqrt{100p_w}}{2} \qquad \text{when } \beta_p > 1.5, \beta_p \text{ shall be } 1.5 \qquad [A.3.b]$$

where, V_{cdd} is the design shear capacity and β_d, β_a and f_{dd} are the same with that is given in Eq. [A.3]. γ_b shall be 1.2 in generally.

Appendix B

COMPRESSIVE CYLINDER RESULTS

In order to confirm the proposed parameters for deep beams given in Chapter 2, the compressive cylinders (100 mm x 200 mm) are analyzed for compressive strength of 22.2 MPa, 25.0 MPa, 28.6 MPa and 32.6 MPa, where these strength values belong to deep beam specimens that are analyzed in this study. The same mesh size with deep beam analyses were used. The stress-strain relationship figures are given in Fig. B.1.

fc'=22.2 MPa

fc'=25.0 MPa

fc'=28.6 MPa

fc'=32.6 MPa
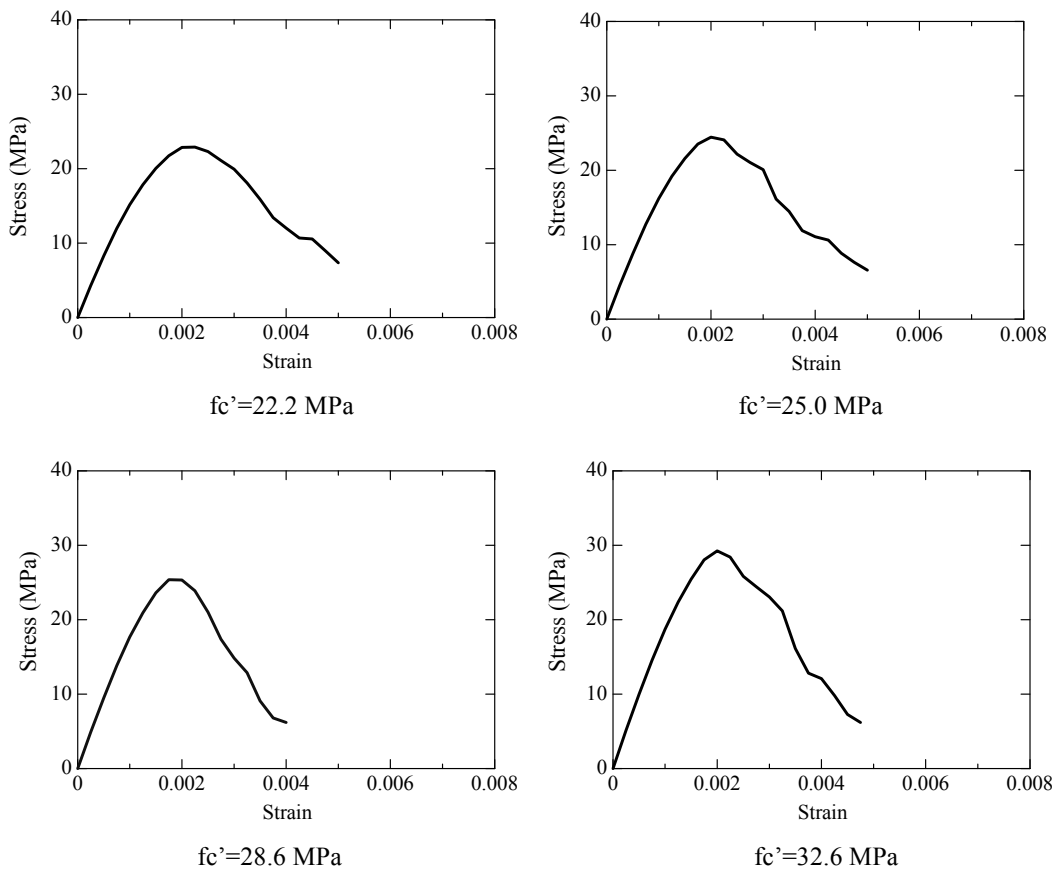
Fig. B.1 Stress-Strain Relationship of Compressive Cylinder Analyses by 3-D RBSM

Appendix C

NUMERICAL ANALYSIS RESULTS FOR CHAPTER 6

C.1 BS3-200 Series

The comparison of the experimental and the numerical load-displacement curves for BS3-200 and BS3-200-LS specimens is shown in Fig. C.1. The experimental and the numerical results agreed well as seen in the figures.
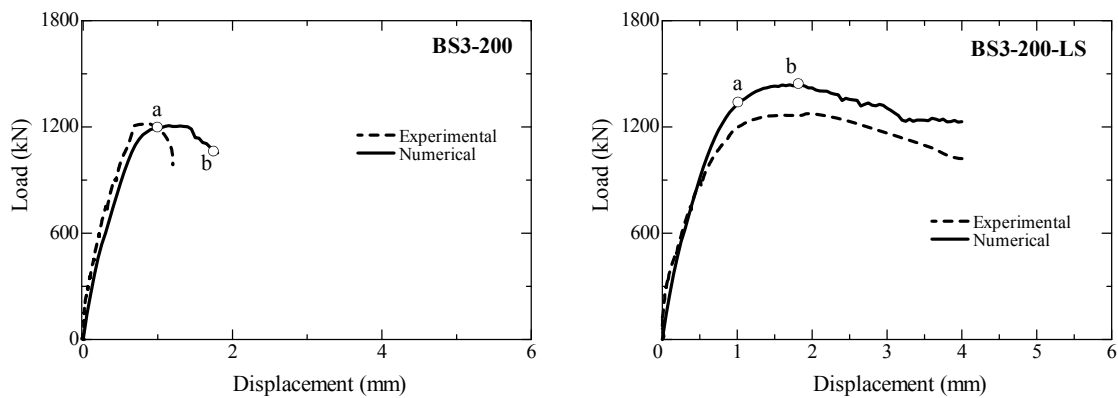
Fig. C.1 Comparison of Load-Displacement Curves

Figure C.2 shows the numerical strain of horizontal stirrups for BS3-200-LS specimen. The strain values along the beam width (G3, G4, G7 and G8) are given in Fig. C.2.(a) while the strains along the beam surface (G1, G2, G5 and G6) are given in Fig. C.2.(b). The strain measurement points are given in Fig. 6.12.(a) in Chapter 6. Similarly with the previous results, the strain values along the beam surface are significantly larger than the one along the beam width and all of them yielded in the post-peak region. Moreover, the strain values of

the horizontal stirrups are significantly larger compared to the previous series since the volumetric ratio is relatively smaller in this case.

(a) Along the beam width
(b) Along the beam surface
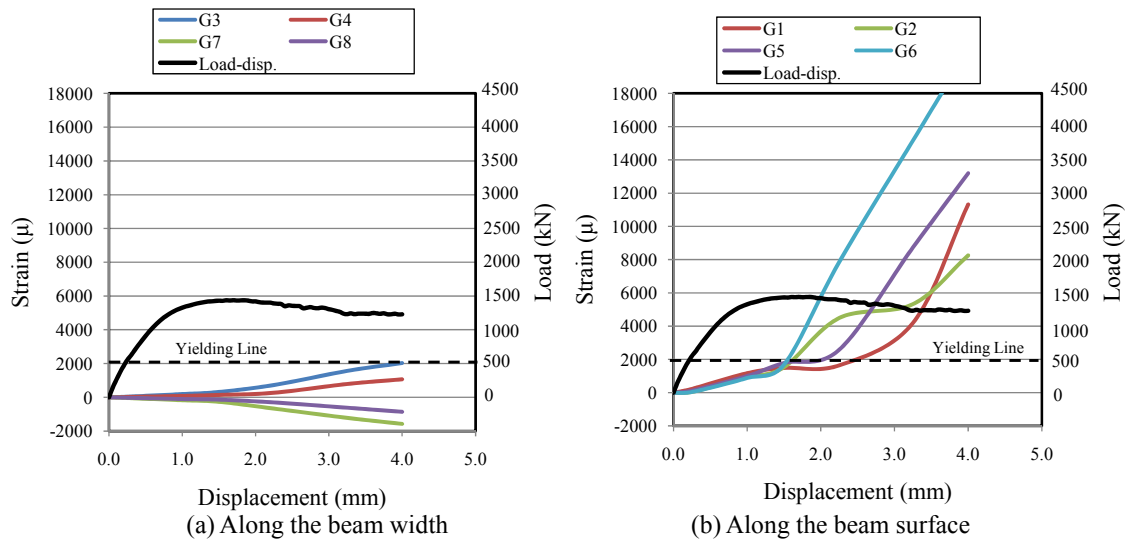
Fig. C.2 Numerical Strain of Horizontal Stirrups (BS3-200-LS)

Figure C.3 gives the comparison of principal stress distribution along the middle longitudinal beam section as well as the stress on the cross-section at the middle of the shear span for BS3-200 and BS3-200-LS specimens. The figures are given at two steps; near the peak load (a) and at a post-peak load (b). The maximum of the stress range is set to 50.0 MPa (1.8*fc'). The stress within the shear span as well as the one on the cross-section increases due to the effect of horizontal stirrup as seen in the figure.
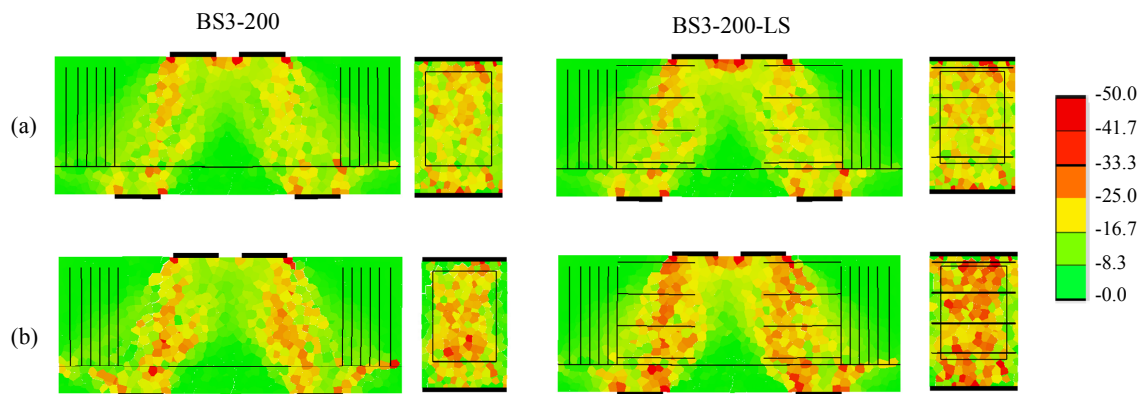
Fig. C.3 Principal Stress Distribution

Figure C.4 shows the comparison of three-dimensional deformed shapes between BS3-200 and BS3-200-LS specimens at the post-peak load (b). The arrangement of the horizontal stirrup reduces the amount of concrete spalling that shows the effectiveness of horizontal stirrup by confinement effect.

(a) BS3-200

(b) BS3-200-LS
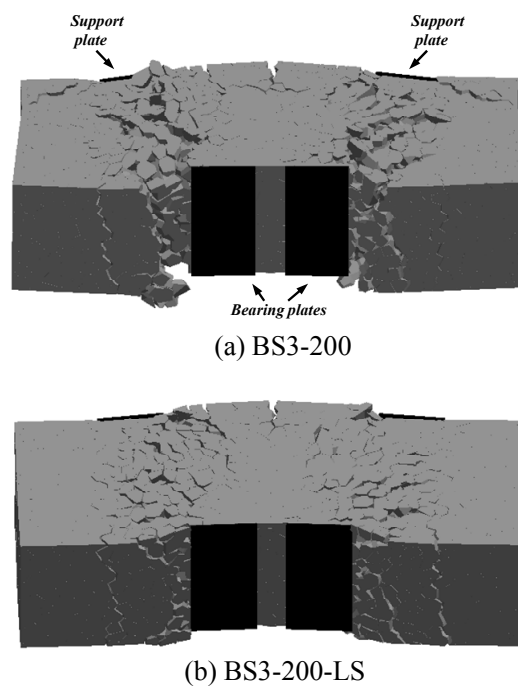
Fig. C.4 3-D Deformed Shapes

146

C.2 B3-1.0 Series

The comparison of the experimental and the numerical load-displacement curves for the specimens is shown in Fig. C.5. B3-1.0 and B3-1.0-VS specimens were already discussed in Chapter 3 in detail. The results of B3-1.0-LS case shows that, the horizontal stirrup is not effective in the beams with a/d=1.0.
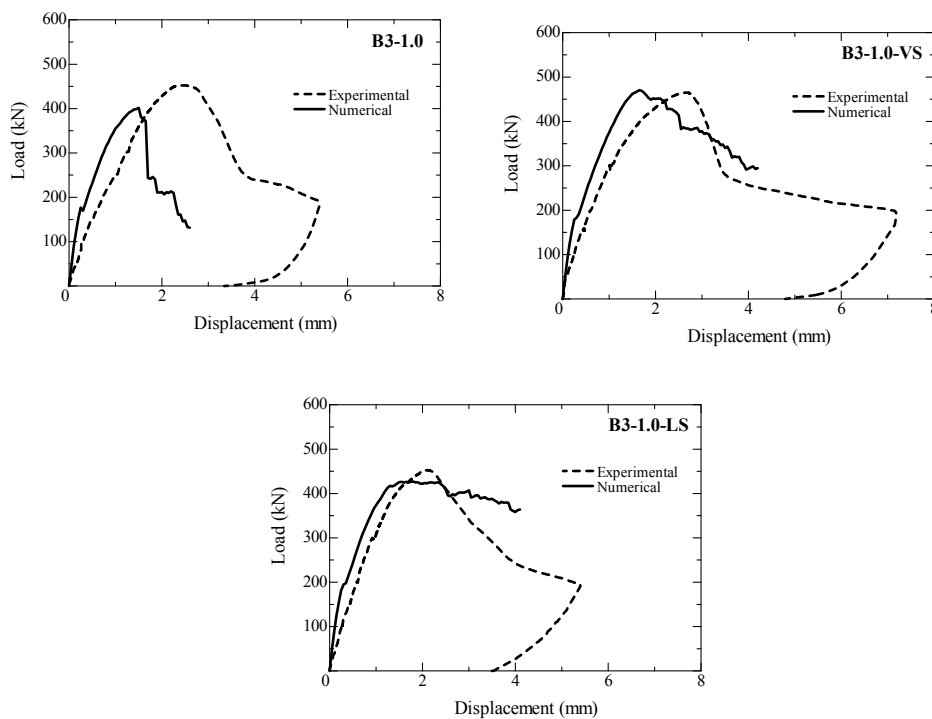
Fig. C.5 Comparison of Load-Displacement Curves

Appendix D

ENERGY CONSUMPTION FOR EACH SERIES GIVEN IN CHAPTER 6

In order to investigate the effect of horizontal stirrup on the ductility, the energy consumption of the beams is compared between the specimens in each series. To achieve that, the area under the load displacement curves is calculated for each beam. The energy is normalized by compressive strength of concrete (f_c') and the energy consumption of the beam with no stirrup in each series. The energy consumption is investigated in pre-peak and post-peak region as well as the total energy. The method to calculate the energy is summarized in Fig. D.1. Up to the peak load, the area under the curve is considered as pre-peak energy consumption. The area under the curve between the peak load and the post-peak load of $0.85.P_{peak}$ is considered as a post-peak energy consumption. The sum of the pre- and post-peak energy consumption gives the total energy as shown in Fig. D.1.
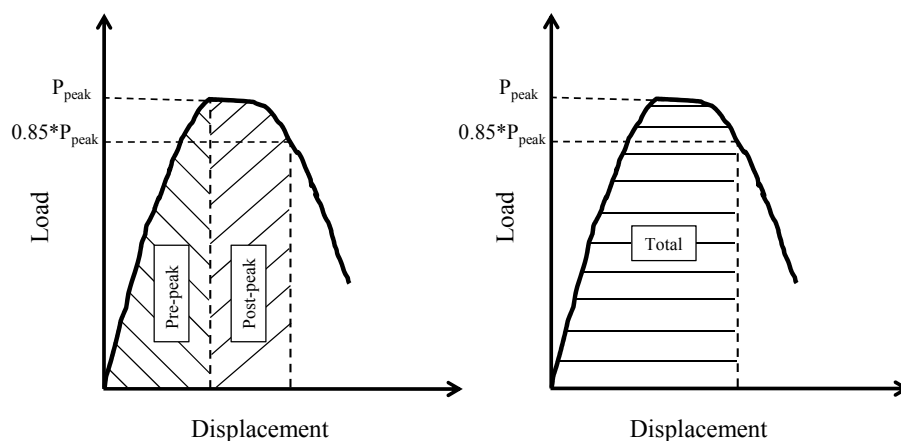
Fig. D.1 Calculation Method for Energy Consumption

Figure D.2 shows the energy consumption for BS2 series. The calculation method for energy consumption The energy consumption increases in BS2-VS case due to the yielding of stirrup in the post-peak region. On the other hand, the energy in the pre-peak increases significantly in BS2-LS specimen due to the increase in load. Moreover, the energy in the post-peak also increases and the total energy consumption is 2.26 times of BS2 case. That is, the horizontal stirrup contributes to ductility of the beam significantly.
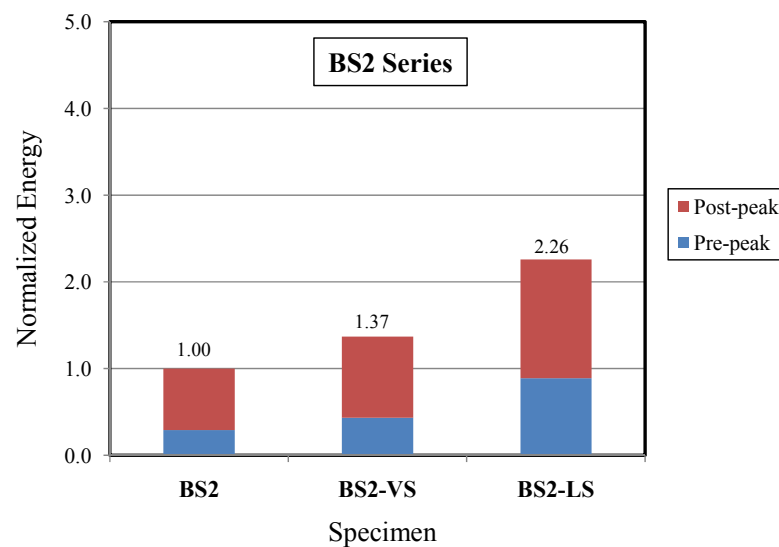
Fig. D.2 Energy Consumption (BS2)

The energy consumption for BS3 Series is shown in Fig. D.3. In the beams with horizontal stirrups, the energy consumption increases significantly in both pre- and post-peak regions. The total energies for BS3-LS-70-h, BS3-LS70 and BS3-LS35 are 2.79, 3.30 and 4.27 times of BS3 case respectively. BS3-LS35 specimen shows the largest ductility since the volumetric ratio of the beam is highest in this case. However, the energy consumption in BS3-LS70-h case is lower than the one in BS3-LS70 case in spite of the volumetric ratio is slightly higher than BS3-LS70 case. The reason is that, since the horizontal stirrups are divided into two loops by means of reinforcement with hooks at each ends (see Fig. 6.2 in

Chapter 6), the hooks caused the increase of cover thickness that led to the decrease of confined concrete area within the horizontal stirrups. Therefore, a less confinement effect could be provided.
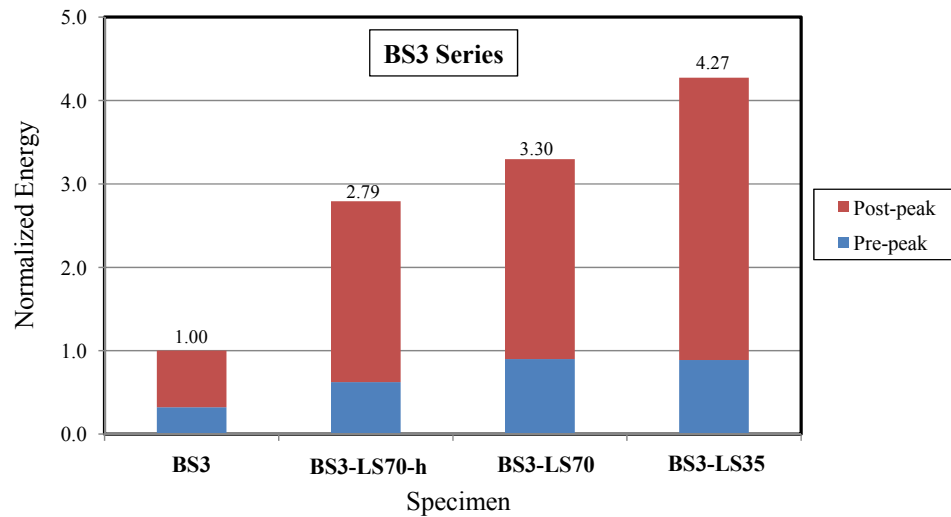
Fig. D.3 Energy Consumption (BS3)

Figure D.4 shows the energy consumption for B3-0.5 Series. The energy consumption decreases in B3-0.5-VS case as seen in the figure. On the other hand, the consumed energies for B3-0.5-LS70 and B3-0.5-LS35 increase in both pre- and post-peak regions. The total energies for B3-0.5-LS70 and B3-0.5-LS35 are 1.55 and 2.06 times of B3-0.5 case respectively. That is, the beams with higher volumetric ratio provide larger ductility.
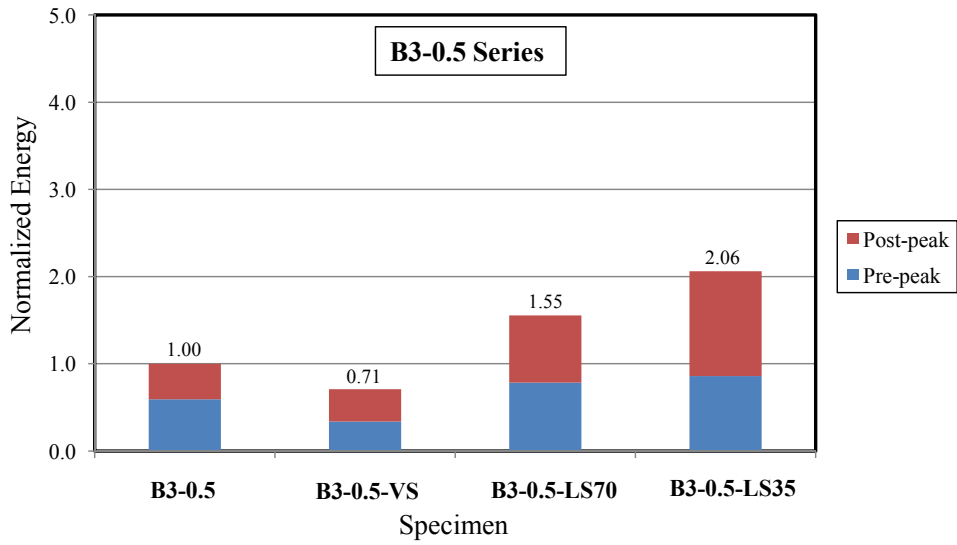
Fig. D.4 Energy Consumption (B3-0.5)

The energy consumption for BS3-200 series is shown in Fig. D.5. The energy consumption in BS3-200-LS specimen increases significantly in both pre- and post-peak regions and the total energy is 3.53 times of BS3-200 case. That is, the arrangement of the horizontal stirrup provides a significant ductility for the beam in this series.
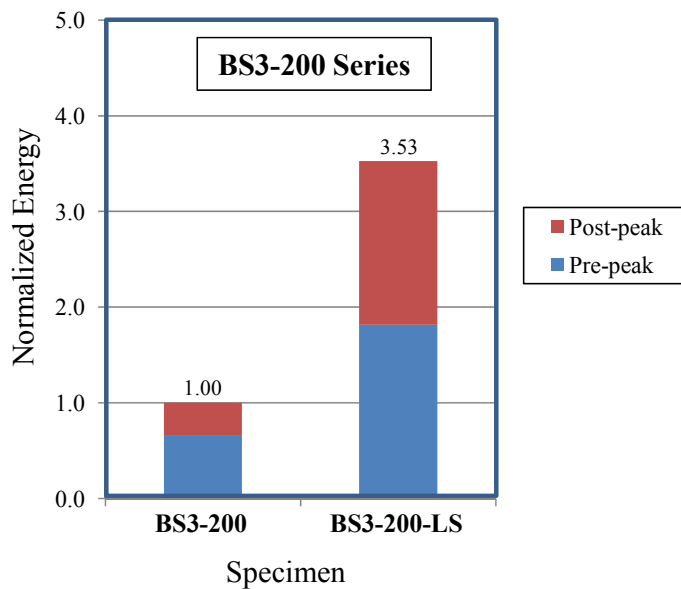
Fig. D.5 Energy Consumption (BS3-200)

Figure D.6 shows the energy consumption for B3-1.0 series. The total consumed energies for B3-1.0, B3-1.0-VS and B3-1.0-LS are 1.00, 1.05 and 0.76 times of B3-1.0 case. That is, the horizontal stirrup is not effective in the beams with a/d=1.0 case.
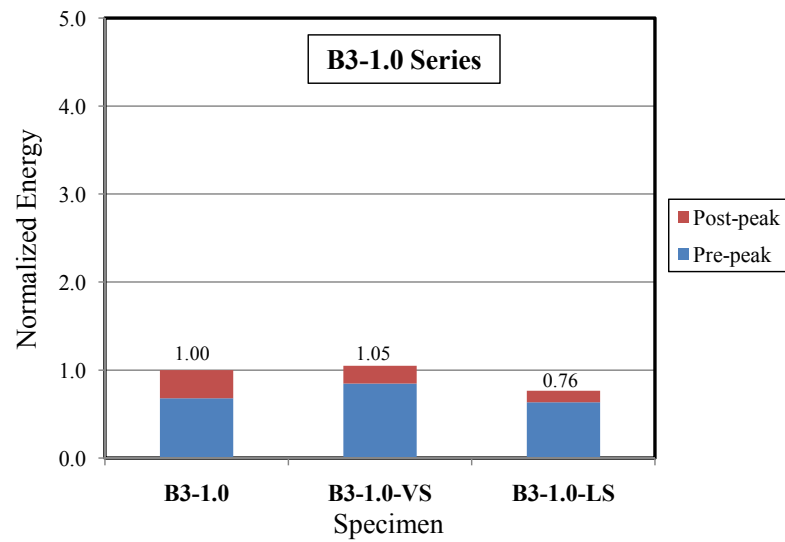
Fig. D.6 Energy Consumption (B3-1.0)